The Role of the Dynamics of the Subducting Plate in Generating Arc Magmatism

BENJAMIN LOUIS MAUNDER

The Role of the Dynamics of the Subducting Plate in Generating Arc Magmatism

Benjamin Louis Maunder

Department of Earth Sciences

Durham University

A thesis submitted for the degree of

Doctor of Philosophy (PhD)

August 2017

Abstract

The thermal state of subducting plates is thought to be of great importance in the generation of the arc magmatism above them. The temperature of slabs affects dehydration, the primary driver of arc magmatism, but may also determine whether the slab itself undergoes partial melting. The focus of this study has therefore been slab temperature: how sensitive it is to the dynamic properties of the slab, and exactly what effect it has on arc magmatism today and back in Earth's early history.

Through the use of numerical models, we improve on existing proxies for slab temperature. Our models demonstrate that the temperature of different parts of the slab depend variably on slab age, trench normal convergence rate, slab dip and the decoupling depth of the subducting and over-riding plates. In addition to forward modelling, we worked backwards from real-world data. To this end we developed a tool to search for statistically significant correlations between the same slab parameters, as well as over-riding crustal thickness, and the trace element characteristics of arc lavas in global databases.

We also investigate a recently proposed dynamic process which may have an effect on arc processes: the formation of plumes of slab derived material (relamination). We find that the relamination of mafic oceanic crust is more likely under Archean conditions, potentially explaining systematic differences between the chemistry of Archean rocks and more modern continental crust and arc rock. We also undertook a preliminary investigation on the feasibility and effect that episodically driven subduction could have on the thermal profile of subducting slabs.

We demonstrate here that through forward numerical modelling and analysis of the chemistry of arc lavas, we can gain valuable insight into the thermal state and complex dynamics of the slab in the critical sub-arc region.

Contents

Declaration

I, Benjamin Maunder, declare that this thesis, presented for the degree of Doctor of Philosophy at Durham University, is a result of my own original research and has not been previously submitted to Durham University or any other institution. Any previously published material and the contributions of colleagues have been, when appropriate, clearly indicated. Work for this thesis was conducted from September 2013 to August 2017 under the supervision of Dr Jeroen van Hunen at Durham University.

Benjamin Louis Maunder
Durham University
August 2017

Acknowledgements

I would like acknowledge and give thanks for the support of my supervisor Jeroen van Hunen. I couldn't have asked for a better supervisor: dedicated and patient. No matter how busy he got he'd always have time to help. I have often been told how jealous other students are of the fact that I have Jeroen as a supervisor and it is easy to see why. I also want to thank Valentina Magni and Pierre Bouilhol who have both also played the role of supervisor throughout my PhD and done so with the same dedication.

I have made extensive use of the computing facilities provided by the Durham University High Performance Computing service who have offered constant support. I would also like thank Arnauld Heuret for allowing me access to a compiled version of his SubMap database.

Thanks to Jeroen's other students, past and present, who have helped me problem solve along the way. Thanks to all my friends and colleagues who made my time at Durham so enjoyable with an extra thanks to Erin, Emma and Ben and my sister Jenny for letting me use their houses as second homes while I wrote up. Thanks to my parents for their support throughout the whole process.

Finally, thanks to my 214 family, the best bunch of housemates that ever was.

1 Introduction

1.1 Earth's Crust and Plate Tectonics

From the core to the surface, the rocky planets of our solar system are compositionally layered. All have ferrous cores, rocky mantles and a thin, outer, compositionally distinct, rocky veneer: the crust (Figure 1.1). All other planets and moons in our solar system have crusts that are approximately uniform in composition and thickness. Earth, on the other hand, has a bimodal crust: oceanic and continental (Rudnick and Gao, 2003). Oceanic crust is relatively uniform (7 km thick and basaltic) and young (very little oceanic crust is older than 160Myrs (Becker et al., 2009)). On the other hand, continental crust is much more variable. It is generally thicker: 30-100 km and, in bulk, richer in silica, making it less dense than oceanic crust. It is also far more variable in age. The oldest continental crust, at 4 Gyrs (Stern and Bleeker, 1998), is not much younger than Earth itself with evidence that continental crust existed even before this (Wilde et al., 2001).

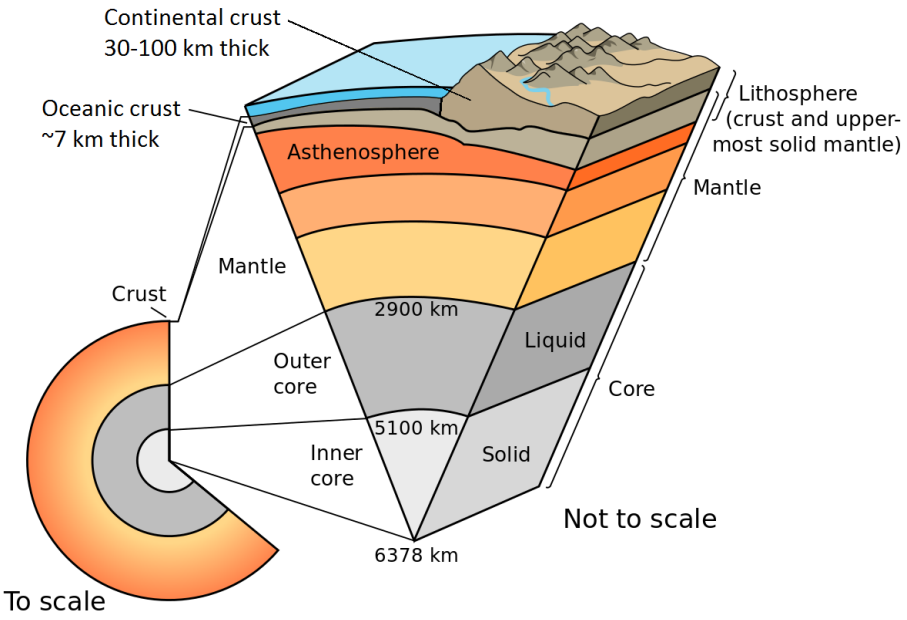

Figure 1.1 Earth's internal structure. The crust has been blown up in the cut-out sector to highlight its bimodality. Compositional layers are labelled: the core, mantle and crust; as well as the mechanical layers: the lithosphere and the asthenosphere. This figure is adapted from: the United States Geological Survey (https://pubs.usgs.gov/publications/text/inside.html).

As well as being the only planet with a bimodal crust, Earth is the only planet/planetoid we know of, on which plate tectonics operates (Stern et al., 2017). The theory of plate tectonics was proposed as a way of explaining the phenomenon of continental drift (Wegener, 1912), which

itself was a way of explaining the observation that Earth's continents appear to fit together. Mechanically, it is known that, under the low temperature, low pressure conditions found near Earth's surface, rock deforms in a brittle manner, with the formation of faults along which any shear strain a body of rock is subjected to is accommodated. As pressure increases, the brittle strength of rock rapidly increases (Byerlee, 1978) meaning that the outer layer of Earth, known as the lithosphere (the crust and upper-most mantle), is strong and rigid (Figure 1.2(a)). As temperature increases with depth, the strength of rock starts to decrease again (in a region known as the asthenosphere) as rock starts to deform in a viscous manner via solid-state creep (McKenzie, 1966): the gradual diffusion of individual atoms and lattice defects (Ranalli, 1995). The theory of plate tectonics suggests that the rigid lithosphere is divided up into tectonic plates, in between which are lithosphere-scale fault zones decoupling the plates, allowing them to move relative to one another, over the weaker asthenosphere (McKenzie and Parker, 1967).

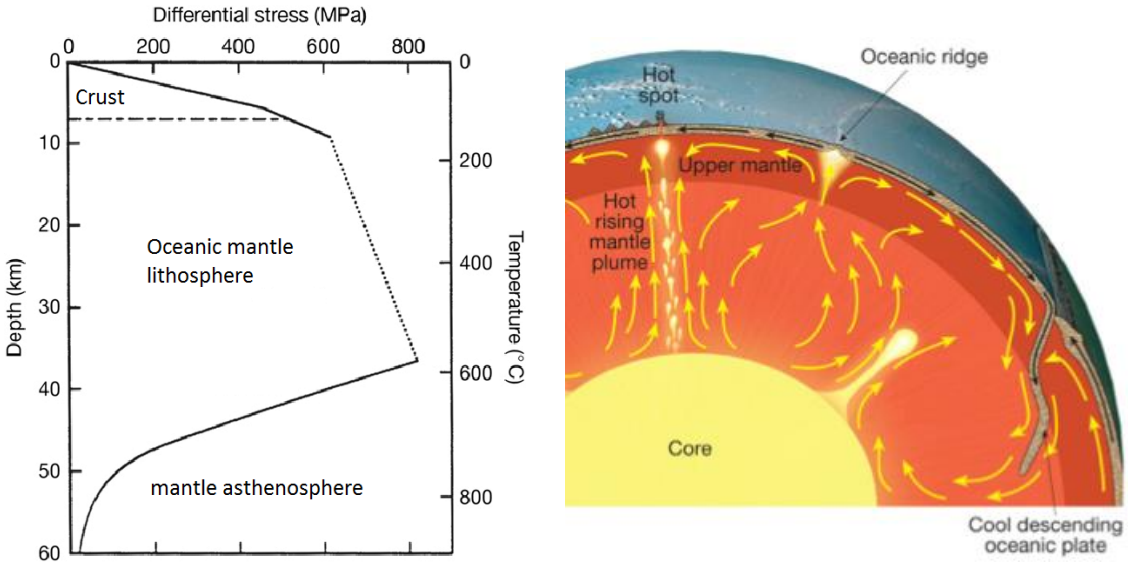

Figure 1.2a) *The strength (measured in differential stress in MPa) of the oceanic lithosphere and asthenosphere with depth. The crust and lithospheric mantle deform in the brittle regime and therefore have strengths that increase linearly with pressure (depth). Below a certain depth, which depends on the thermal profile of the plate and therefore its age, the material deforms by solid state creep and thus behaves viscously, with material becoming weaker with increasing temperature. This figure is adapted from: (Kohlstedt et al., 1995).*

b) *A schematic depicting mantle convection. Subducting plates form the downward limbs of convection cells. The presence of upward limbs of these cells, or "mantle plumes", are often invoked to explain locations of intra-plate volcanism which appears to be unrelated to plate tectonic processes ("hot spots"). Mantle upwelling at mid-oceanic ridges, on the other hand, is more passive: a result of plates being pulled apart by forces ultimately transmitted from subduction zone. This figure is sourced from: Pearson Prentice Hall (https://web.njit.edu/~taozhou/ccc/Ch07_Lecture.pdf).*

The whole process is driven by the sinking of old, cold and therefore dense oceanic plates, back into the mantle: subduction (Forsyth and Uyeda, 1975). The mantle below the plates is cooled

from above and heated from below and, as it can flow on geological timescales, behaves like a convecting fluid (Holmes, 1931) (Figure 1.2(b)). Subduction can be thought of as the downward limb of this convection current. However, while oceanic plates invariably end their lives via subduction; plates, or parts of plates, with continental crust atop, don't normally subduct, because continental crust is thick enough and has a low enough density to act effectively like a buoyancy aid (McKenzie, 1969; Molnar and Tapponnier, 1975). Instead, when two continental blocks converge, they collide in a mountain-building orogeny, and subduction is shut down. This elegantly explains why oceanic crust is rarely found older than ~160 Myrs but we have continental crust that dates back to the early Archean.

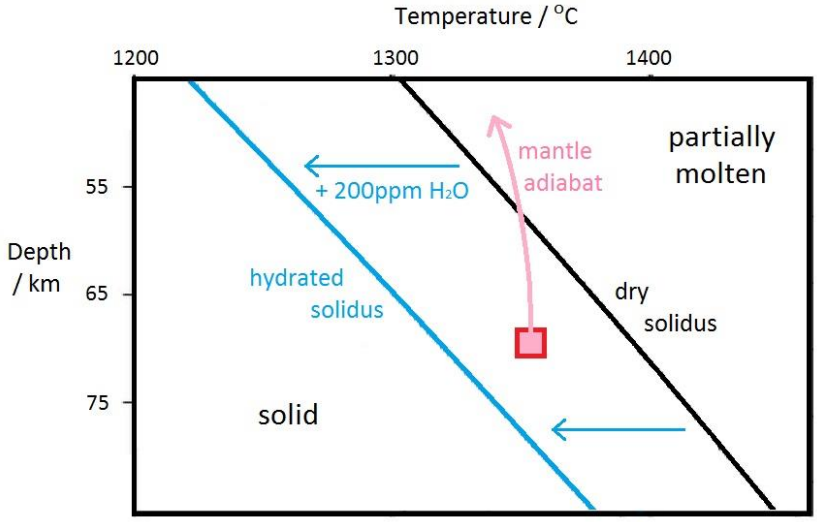

Figure 1.3 The solidus of dry mantle peridotite (black) and mantle peridotite with a small amount of water added (200 parts per million), based on information from (Hirschmann, 2000; Hirschmann et al., 2009). If a batch of dry mantle material is at 1350°C (modern-day upper mantle temperature) and just below a 70 km thick lithosphere, then there are two mechanisms by which it can melt. If a dynamic process allows for it to travel upwards adiabatically (without losing heat) then it will cross its solidus and start to partially melt. This is termed decompression melting and occurs beneath mid-oceanic ridges. If water is added to the batch then this lowers its solidus and causes it to melt. This occurs in the mantle wedge of subduction zones.

To accommodate convergence at subduction zones, plates can be pulled apart. Continents subjected to tensile tectonic stresses are known to rift. The rifting starts as a rift valley (a good example being the East African Rift System (Chorowicz, 2005)), which evolves into an oceanic basin with a mid-oceanic ridge in the centre, thus beginning the lifecycle of an oceanic basin which ends with continental collision (the "Wilson cycle" (Wilson, 1966)). Mid-oceanic ridges are where new oceanic plate is created. To first order, the lithosphere forms by diffusive cooling from above and, as such, oceanic lithosphere thickness is proportional to the square root of the time since it was at the ridge: the plate age (up until a certain age where this relationship breaks down) (Turcotte and Schubert, 2014). The oceanic crust is formed by the melting of the mantle, which

flows up to fill the void left by the diverging plates. This mantle material flows up fast enough to retain its high temperature, but due to the falling pressure, as it rises, it crosses its solidus and partially melts (Figure 1.3) (McKenzie and Bickle, 1988). This is known as decompression melting. Asthenospheric mantle has approximately the same temperature and composition (nearly) everywhere on Earth (Karato, 2012) and, as a result, the amount and composition of melt formed at mid-oceanic ridges is nearly constant everywhere. This explains the uniformity of the oceanic crust, relative to rocks formed via other igneous processes, and also means that mid-oceanic ridges do not produce continental crust, which must be forming via a different mechanism.

1.2 Subduction Systems and Arc Magmatism

As we have discussed, subduction is a key (if not *the* key) driver of plate tectonics on Earth. As such, the question of how viable plate tectonics is on a planetary body is really a question of how viable subduction is (van Hunen and Moyen, 2012). Another important feature of subduction zones is that they allow for the return of material at Earth's surface to the mantle. An important consequence of the addition of volatile material from the surface to the mantle is the generation of arc magmatism. Above nearly all subduction zones found on Earth today lies a volcanic "arc": a chain of volcanoes on the over-riding plate, parallel to the plate boundary. This arc magmatism contributes approximately 20% of global magma production (Crisp, 1984). The commonly accepted mechanism for the production of arc magmas is as follows. Oceanic plates become hydrated during their exposure to seawater, sped up by hydrothermal circulation (Wolery and Sleep, 1976) at mid-ocean ridges and the "outer-rise fracturing" that occurs as plates bend into subduction zones (Ranero and Sallares, 2004). This water is bound in hydrous minerals within the seafloor sediments, oceanic crust and the uppermost lithospheric mantle (down to approximately 15 km (Faccenda et al., 2009)). Many of these hydrous minerals become unstable during subduction as pressures and temperatures rise. The breakdown of these hydrous phases releases water along with a dissolved load (often referred to as "slab fluid") which then percolates upwards (due to being buoyant in the mantle and likely on short timescales compared to the movement of the plates) into the mantle wedge (Arculus and Powell, 1986; Tatsumi, 2005). The temperature of the mantle wedge is approximately the same as the ambient asthenosphere and sustained by mantle flow, driven by the subducting plate itself. The solidus (the temperature a material begins to melt at, at a given pressure) of mantle peridotite is highly dependent on the presence of water (Gaetani and Grove, 1998). At mantle wedge pressures and temperatures, dry peridotite does not melt whereas hydrated peridotite does (Figure 1.3). As such, the addition of

slab derived fluids to the mantle wedge causes this mantle material to melt. It is these melts that rise through the over-riding plate and erupt at the surface. As they are percolating through the over-riding plate they are likely altered by assimilation of materials they're passing through as well as via partial recrystallization on the way (a process called fractional crystallisation). This whole process is summarised in Figure 1.4.

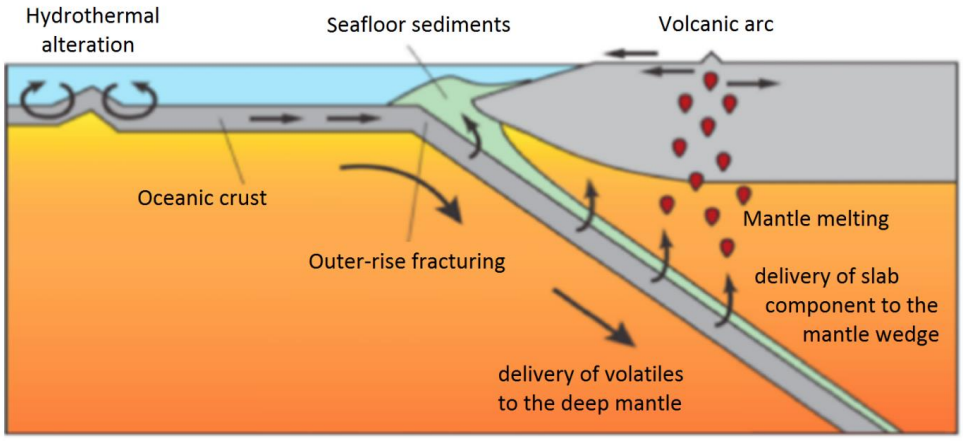

Figure 1.4 A schematic diagram outlining the processes that give rise to arc volcanism. The movement of water and other volatiles is highlighted by arrows: uptake into the crust and mantle at mid-oceanic ridges and via outer-rise fracturing; release from the slab into the mantle wedge via slab metamorphism; then incorporation into the arc crust and return to the exosphere via arc volcanism. This diagram is adapted from (Marschall, 2005), modified from (Bebout, 1996).

There are various lines of evidence to support this mechanism. The isotopic signatures of arc lavas have been shown to match the signatures of the sediment input at the trench, a strong indication that there is chemical transfer from the slab to the melt (Hawkesworth et al., 1997). However, the most important evidence lies in the concentrations of major and trace elements in the erupted lavas, in comparison with lavas erupted in other tectonic settings. Arc lavas show similarities, in their major element compositions, to other lavas, known to be mantle-derived (Plank and Langmuir, 1988). This has led to the conclusion that the source of arc magmas is (usually) the mantle. Without further evidence it was believed for a time that arc magmatism was a result of decompression melting (just as at mid-oceanic ridges), as mantle peridotite flows up and into the corner of the mantle wedge. However, the trace element concentrations tell a different story. A strong enrichment in a set of elements known as large ion lithophile elements (LILEs) compared to another set known as high field strength elements (HFSEs) is strong evidence for the involvement of subducted fluid (Hawkesworth et al., 1994; McDonough, 1991; Pearce, 1982; Pearce and Peate, 1995). This is because, while both LILEs and HFSEs are "incompatible"; that is that they are not readily incorporated into the main rock forming minerals, LILEs are readily soluble in aqueous fluids and HFSEs are not. As such, LILEs are carried from the slab to the mantle wedge by fluids

and HFSEs are not, leading to the elevated LILE/HFSE ratio (often referred to as the "arc signature") that is observed across all arcs.

1.3 The Formation of Continental Crust, Throughout Earth's History

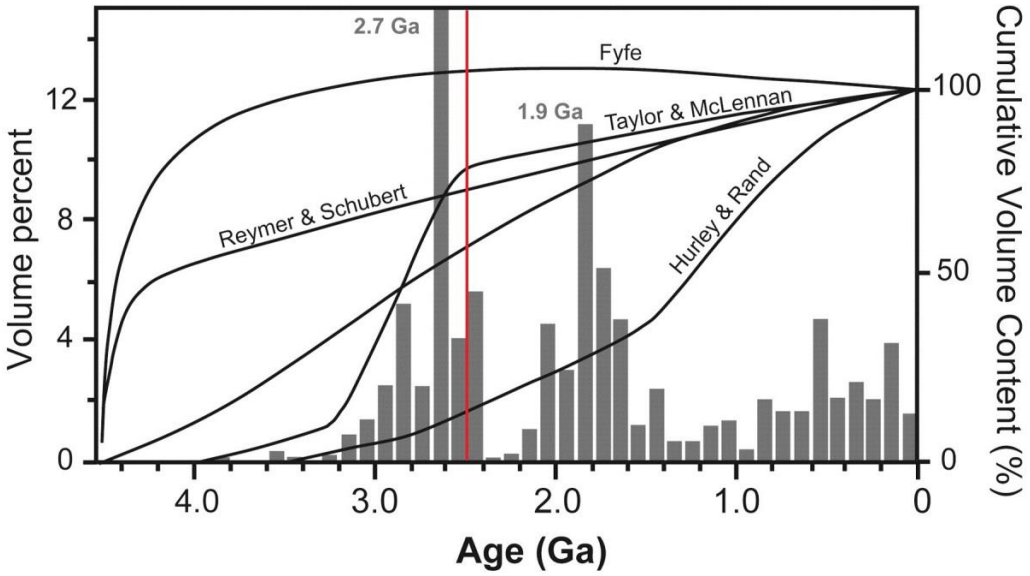

Figure 1.5 Estimates of continental crust growth rates are plotted with black lines. These estimates were made in the following studies: (Fyfe, 1978; Hurley and Rand, 1969; Reymer and Schubert, 1984; Taylor and McLennan, 1985). The end of the Archean is marked by a red line. This is when a shift in tectonic regime has been proposed by some authors. A histogram of ages of juvenile continental crust, as inferred from ages of zircon crystals, neodymium isotope ratios and lithological associations (Condie, 2015) is overlain. These demonstrate peaks at 2.7 Ga and 1.9 Ga, which correspond to times where supercontinents were forming. This figure is adapted from (Hawkesworth et al., 2010).

The origin of Earth's continental crust (CC) is a hotly debated topic. However, it is known that the bulk continental crust has an arc signature (Taylor and McLennan, 1985); evidence that continental crust formation is related to arc magmatism (Davidson and Arculus, 2006). The presence of an arc signature even in Archean continental crust, in particular a characteristic suite of Archean rocks collectively referred to as TTGs (trondhjemites, tonalities, and granodiorites), is used as evidence for the operation of subduction in the Archean (van Hunen and Moyen, 2012) and that subduction has been the key CC forming process throughout Earth's history. A counterargument is that an apparent enrichment in LILEs in Archean CC may simply arise due to the ancient mantle being less depleted in LILEs (Condie and Pease, 2008). However, some Archean rocks have more of an arc signature than others. Moyen & van Hunen (2012) identify three main types of Archean terrane with differing signatures: plume-like komatiites and tholeiites with elevated MgO contents (which according to Herzberg et al. (2010) are associated with melting of

mantle hotter than the ambient mantle); rocks with a stronger arc signature; and bimodal terranes. Rocks with a stronger arc signature tend to occur together, which indicates that they are a result of a regional process: a more convincing indication of subduction.

There is much debate on the rate of CC production throughout Earth's history: some argue that the CC formed early in Earth's history and has just been recycled since (Armstrong and Harmon, 1981), while others believe that CC formation is occurring on Earth today (Gazel et al., 2015; Taylor and McLennan, 1995) (Figure 1.5). The observation of peaks in the ages of globally collected zircon crystals, which coincide with points in Earth's history when continents were amalgamating to form a supercontinent, appears to fit with the hypothesis that CC is formed in oceanic arcs, as supercontinent assembly allows for more arc material to be preserved (Condie et al., 2011). There is, however, evidence for a change in CC formation mechanism at the end of the Archean, within the rock record. Key examples include a change in the composition of diamond inclusions (Shirey and Richardson, 2011), the absence of subduction related ultra-high-pressure metamorphic rock from before the Neoarchean (Sizova et al., 2014) and an abrupt change in oxygen-isotope proxies for crustal reworking at the end of the Archean (Dhuime et al., 2012). In addition to this evidence, when looking at mantle temperature estimates (constructed from MgO contents of Archean rocks derived from the ambient mantle), slower mantle heat loss in the Archean is required to fit the data (Herzberg et al., 2010). As plate tectonics is the primary way in which Earth loses heat (> 60% of heat loss occurs through the oceans, primarily at mid-ocean ridges) this would argue for a slower, or perhaps intermittent form of plate tectonics in the Archean (Korenaga, 2006). Numerical modelling of subduction has also suggested that subduction might be more intermittent in the Archean, due to the higher mantle temperatures and therefore weaker plates (Moyen and Van Hunen, 2012). Other modelling studies have suggested that for part or perhaps throughout the Archean, subduction wasn't viable at all (Sizova et al., 2010) and instead Earth operated under a stagnant lid or "plume-lid" regime (a static lithosphere with no plate tectonics) (Fischer and Gerya, 2016) with the potential for a longer-term episodicity involving large scale mantle over-turn events (O'Neill et al., 2007). A modern analogue for a plume-lid early Earth might be Venus (Rozel et al., 2017). Another planetoid currently in a stagnant lid regime is Io. On Io, a "heat pipe" mode is operating where lava is extruded and the lithosphere gradually subsides underneath: another potential tectonic mode for the early Earth (Moore and Webb, 2013). However, there is evidence for the presence of subduction from this time in paired metamorphic belts and low-angle seismic reflectors in Archean lithosphere, which have been interpreted as fossil subduction interfaces (van Hunen and Moyen, 2012).

1.4 Archean Continental Crust and Slab Melting

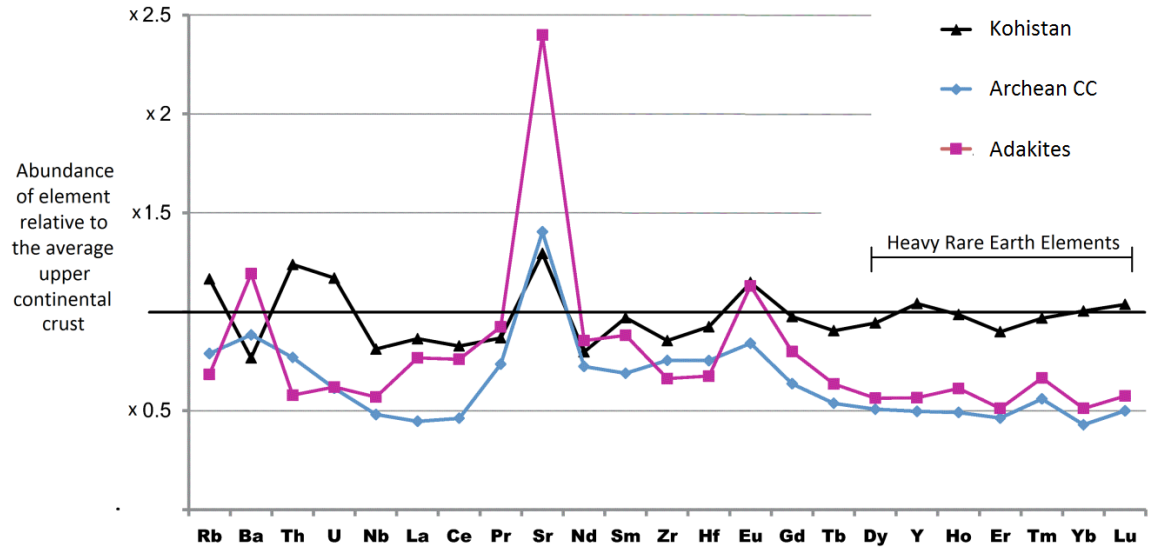

Figure 1.6 The trace element characteristics of Archean continental crust; modern day "adakites"; and an arc that was accreted to the Asian continent in the Phanerozoic: the Kohistan arc, all relative to the bulk upper continental crust. The depletion of heavy rare earth elements is present in both adakites and in the Archean continental crust but absent in the more recently formed arc.

As mentioned previously, Archean CC (specifically TTGs) shows similarities to more recent CC and also arc rock. However, there are some consistent differences. Archean TTGs commonly demonstrate depletion in the heavy rare earth elements (HREEs) (Martin, 1999) (Figure 1.6). This geochemical signature is actually observed in certain arc lavas today, although they are rare. Such lavas are termed "adakitic" (Kay, 1978) and their occurrence has been shown to often coincide (although there are exceptions) with the subduction of young oceanic plates, which should be hotter (discussed more below) (Defant and Drummond, 1990). It has been shown in lab experiments that the melting of mafic materials (such as the subducting oceanic crust), at high pressure (corresponding to mantle depths) produces a melt with these characteristics (Foley et al., 2002). The high pressure is necessary for garnet to be stable in the residue as this is the mineral responsible for the sequestration of the HREEs. These two lines of evidence have been used to support a "slab melt" hypothesis for the formation of adakites. The basic premise is that, under hotter subduction conditions, the subducting oceanic crust gets hot enough to partially melt such that not only are aqueous fluids released from the slab, but also are substantial quantities of crustal melts, which mix with the mantle melts. This would likely occur more often in a hotter Archean mantle, explaining the prevalence of this signature in Archean rock. However, there are other mechanisms that produce adakitic signatures. High pressure fractional crystallisation of a mantle melt is capable of producing depletion in HREEs and there are also

other geodynamic settings where mafic material may melt in the stability field of garnet (Macpherson et al., 2006). A popular non-subduction model for the formation of TTGs involves the formation of a stagnant lid and a thick, uniform crust formed by mantle melting above mantle plumes (Moore and Webb, 2013). The base of this crust undergoes metamorphism, densifies and drips into the mantle where it melts, providing the source for TTGs (Zegers and van Keken, 2001). However, we don't see continental crust forming on other bodies operating under stagnant lid regimes (e.g. Venus) and this mechanism doesn't allow for the drawing down of water into the mantle.

It has been suggested that slab melting may be the key to forming CC today as well. The arc that is believed to be producing the most "continental like" lavas today (andesitic as opposed to basaltic and particularly enriched in incompatible elements) is the Central American land bridge where the subduction of a hot-spot track is occurring, thereby elevating slab temperature (Gazel et al., 2015). However, it has been observed that there is a correlation between crustal thickness beneath the volcanic arc and Sr/Y (a key indicator of the adakitic signature (Moyen, 2009)). This, along with evidence that Sr/Y increases as lavas become more "evolved" (higher SiO_2 and lower MgO, an indication that a lava has undergone more extensive fractionation), indicates that fractionation processes are potentially more important in the development of this signature on Earth today (Macpherson et al., 2006). Interestingly though, this trend is not seen in Archean TTGs (Chiaradia, 2015).

1.5 Relamination

While slab melting has indeed been shown to be viable in warm subduction zones via the use of numerical models, provided the subducting crust is rehydrated by the dehydration of the slab mantle below, these models demonstrate that the slab melt contribution is small, in terms of volume, compared to the amount of mantle wedge melting one would expect (Bouilhol et al., 2015). As such, the source, even for lavas with a "slab melt" signature, is mostly mantle derived and thus basaltic. Given that the bulk CC is believed to be andesitic (Rudnick and Gao, 2003), this presents a paradox. There have been a couple of proposed additional mechanisms to account for this. The first is that basaltic melts undergo fractionation with the more felsic fractionated magma emplaced into the over-riding arc crust and the more mafic residual somehow removed and recycled back into the mantle. The mafic residue is denser than mantle peridotite and so it is suggested that this removal mechanism may simply be lower crustal foundering (Kay and

Mahlburg-Kay, 1991). However, this may be difficult from a geodynamic perspective, as the presence of any underlying mantle lithosphere would prevent the sinking of any crustal material.

An alternative mechanism that has garnered more support recently is “relamination” (Hacker et al., 2011) (Figure 1.7(a)). It was originally observed in numerical models of subduction that materials that remain buoyant in the mantle upon subduction may detach from the slab and rise through the mantle wedge as compositionally driven plumes or diapirs (Gerya and Yuen, 2003b) (Figure 1.7(b)). These plumes of crustal material would be heated to mantle wedge temperatures, and very likely partially melt, below the over-riding plate (Castro, 2014). The resulting melt would be andesitic and the residue easily recycled. This process need not be the primary formation mechanism of arc magmatism, rather a rare or slow process that has gradually had the effect of refining the CC over Earth’s history, perhaps occurring if small intra-oceanic arcs are subducted, or significant amounts of sediment or material dragged into the subduction channel by erosion. In fact, the occurrence of relamination has been suggested to be essential to explain certain trace element signals in arc lavas. In particular, the enrichment observed in thorium and barium (both incompatible but not fluid mobile) likely comes from subducted sediments, and recently it has been suggested that release of these elements requires temperatures of > 1000^{o}C: too hot to even be slab top temperature (Behn et al., 2011). It has also been used to explain why, when volatile input into subduction zones are approximately uniform in time and space, arc magmatism is discrete in both (Marschall and Schumacher, 2012).

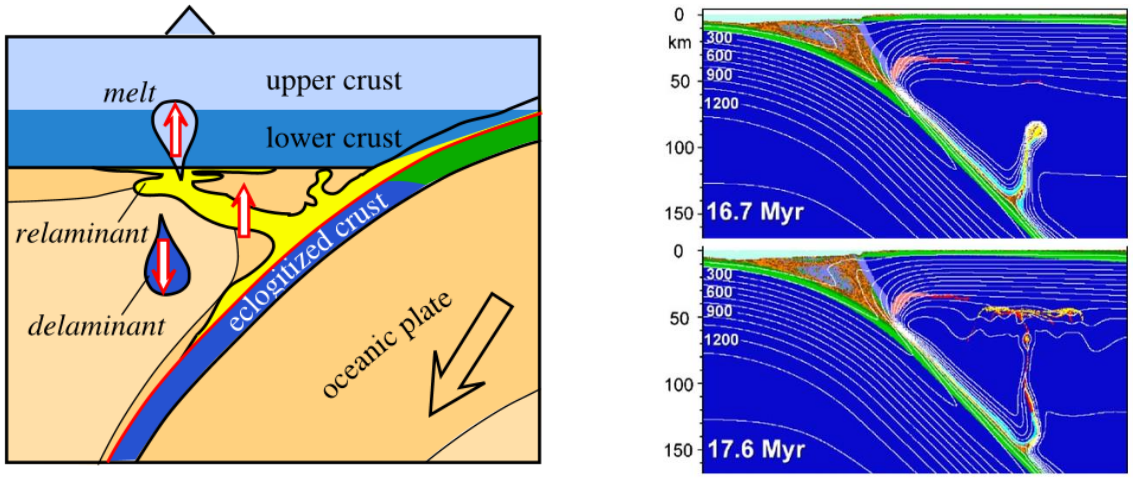

Figure 1.7a) Schematic of the process of “relamination”. Any buoyant material dragged into the subduction system (yellow) has the potential to come away from the subducting plate. This material could consist of sediments, eroded over-riding crust, subducted oceanic arcs or perhaps even oceanic crust under the right conditions. This material then melts below the over-riding lithosphere with the melt rising to form the crust and the residue left to sink back into the mantle. This figure is sourced from (Hacker et al., 2011).

b) The existence of this dynamic behaviour was originally suggested after observing it in numerical simulations of subduction. This is a model snapshot from a study by Gerya and Yuen (2003b) demonstrating the formation and development of a crustal mantle wedge plume. This figure is sourced from (Gerya et al., 2006).

1.6 Slab Temperature

Many of the subduction related chemical or physical processes that have been proposed to contribute to the formation of Earth's CC depend on the thermal state of the subducting plate. Slab melting clearly depends on the temperature of the subducting crust (Poli and Schmidt, 2002). It also depends on the dehydration of the slab mantle below, which depends on the temperature of the slab interior, as it has been shown that a supply of fluid from the mantle below is essential to melt the crust (Bouilhol et al., 2015). The process of relamination is also likely to be temperature dependent as it requires crustal material to be weak enough to form the initial Rayleigh-Taylor instabilities at the subduction interface which go on to feed the crustal plumes. The strength of materials, particularly at mantle depths where viscous creep dominates, is temperature dependent (Ranalli, 1995). Even normal volatile recycling at subduction zones should be slab temperature dependent (Poli and Schmidt, 1995). In colder slabs it is suggested that hydrous phases may remain stable in the deep mantle to allow for the transport of water to the deep mantle, a process that has likely changed over Earth's history due to the mantle likely being hotter in the Archean, resulting in hotter slabs (Magni et al., 2014). As such, understanding the controls on the thermal state of slabs, and better understanding the effect this has on the chemistry and dynamics of the subduction system, is certainly important in understanding the formation of CC.

Analytical analysis of a slab sinking into a hot mantle led to the first insight into what controls the thermal structure of slabs. The resulting proxy for the temperature of a slab, the slab "thermal parameter", ϕ (Kirby et al., 1996), is still commonly used and defined as follows:

$$\phi = tv\sin(\theta)$$

where t is the age of the slab, which, as mentioned before, determines the thermal profile of an oceanic plate prior to subduction; v is the trench-normal convergence rate of the two plates; and θ is the slab dip angle (the angle of the slab relative to the horizontal). $v\sin(\theta)$ can be thought of as the effective sinking velocity of the plate. The thermal parameter is dimensionally a length and its physical interpretation is that it gives an estimate of the depth a given isotherm reaches. It therefore performs best as a proxy for the temperature of slab interiors. However, since then, more detailed studies have been undertaken, including the use of numerical simulations. van Keken et al. (2002) used such simulations to demonstrate there was only a weak correlation between slab top temperatures at the crucial sub-arc depths and $\log_{10}(\Phi)$. Other modelling studies produce variable results. For example, Peacock (2003) found that young and slowly subducting slabs are the warmest and in extreme cases may melt, while Magni et al. (2014)

demonstrated that slab velocity has the strongest control on the thermal structure of slabs and that its effect isn't straightforward: faster slabs have colder interiors but hotter slab surfaces. In addition, the thickness of the over-riding plate and is likely to have a strong control on slab temperature and isn't encompassed in the current definition of the thermal parameter at all (Currie et al., 2004; Peacock, 2003). Numerical studies like these have also been extended to investigate the effect the thermal state of slabs has on the fate of subducted volatiles (Peacock, 1990) and also the feedback the behaviour of volatiles has on the thermal state of slabs (Arcay et al., 2007).

It has been suggested that certain geochemical signatures do show some correlation with the thermal parameter (Cooper et al., 2012; Ruscitto et al., 2012). However, the correlation isn't strong and in fact weaker than correlation with other parameters, such as the over-riding Moho depth (Turner and Langmuir, 2015a). As discussed earlier, the adakitic signature appears to coincide where subduction of young (and therefore likely hotter) plates is occurring, or has occurred. There are, however, many notable exceptions to this rule. In many of these cases, extraordinary dynamics have been called upon to explain how the slab temperature may have been raised. These include the formation of slab tears or windows (Thorkelson and Breitsprecher, 2005) and subduction initiation (Sajona et al., 1993). In addition, the same correlation hasn't been observed with convergence rate or slab dip, as one might expect if this were to be slab temperature controlled.

1.7 Thesis Aim and Outline

The aim of this thesis is to provide more insight into the subduction related processes that have been proposed to have played a role in the formation of Earth's continental crust over time, through the use of two-dimensional numerical models of subduction as well as analysis of global geochemical and geophysical databases. We aim to test the hypothesis that key chemical characteristics of the continental crust are slab derived with studies focusing on the thermal state of the subducting slab and how this may affect the chemistry of arc lavas. We also focus on the specific process of relamination and how this may have evolved over Earth's history and how these changes could potentially explain differences in the chemistry of Archean continental crust compared to more modern continental crust and arc rock. The investigations are conducted with the slab melting hypothesis for the formation of early continental crust (as well as modern-day adakites) in mind, with an aim to critically assess the viability of such a mechanism.

1.7.1 Chapter 2

In this chapter we describe the setup of the numerical models used in Chapters 3, 5 and 6, including a description of the governing physics and the numerical techniques used.

1.7.2 Chapter 3

In order to critically assess whether slab melting is occurring today (or whether it may have been in the Archean) or whether the thermal state of slabs has a significant effect on the chemistry of arc magmatism, it is first important to know what factors determine the thermal state of slabs. We conduct a parametric study, using our models to assess the effect of slab age, convergence rate, slab dip and plate decoupling depth on the temperature of the slab, at different points in the slab. Empirically derived proxies are developed which improve on the original thermal parameter.

1.7.3 Chapter 4

In this chapter we use global geochemical and geophysical databases to look for correlations between these slab parameters and fluid and “slab melt” related chemical signatures. With the results of the previous chapter in mind we assess whether it is likely that certain geochemical signatures are controlled by the thermal state of the subducting plate.

1.7.4 Chapter 5

In this chapter we aim to assess how the process of relamination may have changed throughout Earth’s history by using our numerical models of subduction. We specifically investigate whether the mafic subducting crust might have been more involved in the process of relamination as an explanation for the chemical differences seen between Archean TTGs and younger continental crust.

Chapter 5 is based on a published manuscript. The co-authorship of this publication reflects the training, discussion and specialist knowledge provided by the collaborators.

1.7.5 Chapter 6

In this chapter we present the results from a preliminary investigation of Archean episodic subduction, specifically looking at the effect of sudden stalling and subsequent gradual restarting of subduction on the thermal state of the subducting crust.

1.7.6 Chapter 7

In this chapter we summarise the results from all chapters and outline the main conclusions that can be drawn from this body of work. Suggestions for further work are also made, including a description of the progress made in these directions so far.

2 Method

2.1 Governing Physics

Over geological timescales, the Earth's rocky interior behaves like a convecting fluid. This convection is driven by buoyancy differences arising from both thermal and compositional heterogeneity. With the assumption of incompressibility and the neglecting of density differences, except where multiplied by the acceleration due to gravity (a set of assumptions commonly known as the Boussinesq approximation), the basic set of coupled equations which describe this behaviour are presented below (Turcotte and Schubert, 2014). The parameters associated with the symbols used in the following equations, their values (where applicable), and their units (if any) are given later in Table 2.1.

2.1.1 The Conservation of Mass:

$$\nabla \cdot \mathbf{u} = 0$$

Equation 2.1

i.e. that the velocity field has zero divergence, or the "incompressibility" assumption.

2.1.2 The Conservation of Thermal Energy:

$$\frac{\partial T}{\partial t} + \mathbf{u} \cdot \nabla T = \kappa \nabla^2 T$$

Equation 2.2

This equation contains both a diffusion and advection term for the movement of heat. There are no source or sink terms as the Boussinesq approximation also involves ignoring internal sources and sinks of heat: radiogenic, shear and adiabatic heating. Neglecting radiogenic heating is valid for all materials used in our models (mantle and mafic crust) over the relatively short timescales for our studies. Adiabatic heating occurs at a rate of 0.5^{o}C/km (Turcotte and Schubert, 2014) and as such should only have a small effect in models of the shallowest upper mantle. Its rheological effect should also be partially offset by neglecting pressure dependence in the material flow laws.

The effect of shear heating will be largest in regions of high strain rate. In our models this is at the top of the subducting slab, although the strength of its effect is debated (Peacock, 1996).

2.1.3 The Conservation of Momentum:

$$-\nabla P + \nabla \cdot \left(\eta\left(\nabla \mathbf{u} + (\nabla \mathbf{u})^{\mathrm{T}}\right)\right) + \Delta\rho g = 0$$

Equation 2.3

where the density differences $\Delta\rho$ can arise due to both thermal and composition heterogeneity:

$$\Delta\rho = \rho_0 \alpha (T - T_0) + \Delta\rho_c$$

Equation 2.4

Equation 2.3 is the simplified Navier-Stokes equation with the inertia terms dropped, or the "Stokes equation". This simplification is justified as the gravitational forcing terms are many orders of magnitude greater than the system's inertia in the case of mantle convection. In other words, forces at all points in the system are balanced. This has the effect of making this equation time-independent: the temperature and compositional fields yield a unique instantaneous velocity and pressure field (the instantaneous stokes flow problem (Zhong et al., 2007)).

2.1.4 The Conservation of Composition:

$$\frac{\partial C}{\partial t} + \mathbf{u} \cdot \nabla C = 0$$

Equation 2.5

This advection equation is solved separately using a marker-in-cell method (see Section 2.5.4).

2.1.5 Non-dimensionalisation

All the above equations are simplified by the following non-dimensionalisation:

$$\mathbf{x} = \mathbf{x}'h \qquad t = t'\frac{h^2}{\kappa} \qquad \mathbf{u} = \mathbf{u}'\frac{\kappa}{h} \qquad P = P'\frac{\eta_0 \kappa}{h^2} \qquad T = \Delta T(T' + T_0) \qquad \eta = \eta_0 \eta'$$

simplifying the equations to (with the primes dropped):

$$\nabla \cdot \mathbf{u} = 0$$

Equation 2.6

$$\frac{\partial T}{\partial t} + \mathbf{u} \cdot \nabla T = \nabla^2 T$$

Equation 2.7

$$-\nabla P + \nabla \cdot \left(\eta\left(\nabla \mathbf{u} + (\nabla \mathbf{u})^{\mathrm{T}}\right)\right) + (R_a T + R_b C)e_z = 0$$

Equation 2.8

$$\frac{\partial C}{\partial t} + \mathbf{u} \cdot \nabla C = 0$$

Equation 2.9

Performing this non-dimensionalisation also has a computational advantage as it negates the need to store the large numbers typical of geodynamic problems. The thermal and compositional Rayleigh numbers, Ra and Rb respectively, are defined as:

$$Ra = \frac{\alpha \rho_0 g \Delta T h^3}{\kappa \eta_0} \qquad Rb = \frac{\Delta \rho_C g h^3}{\kappa \eta_0}$$

These non-dimensional numbers quantify the vigour of convection due to temperature and compositional differences. $\alpha \rho_0 \Delta T$ is the difference in density arising from a temperature difference of ΔT and $\Delta \rho_C$ is the difference in density between a particular material and its surroundings. There are two basic materials in our model: mafic crust and mantle. The crust is made less dense than the mantle by a fixed amount (individual to each study) above a certain fixed eclogitisation depth (see Figure 2.1), and more dense below it (again by a fixed amount individual to each study). This is a first order approximation to represent depth-dependent, densifying, metamorphic reactions that occur in mafic materials (Duesterhoeft et al., 2014; Hacker, 1996; Poli and Schmidt, 2002).

Other than the densities, it can be seen that the vigour of convection increases with the scale of the system and the acceleration due to gravity and decreases with increasing thermal diffusivity and viscosity. Complexity is added to these equations due to the fact that viscosity is temperature, composition and strain rate dependent (see Section 2.3.1).

2.2 Model Setup

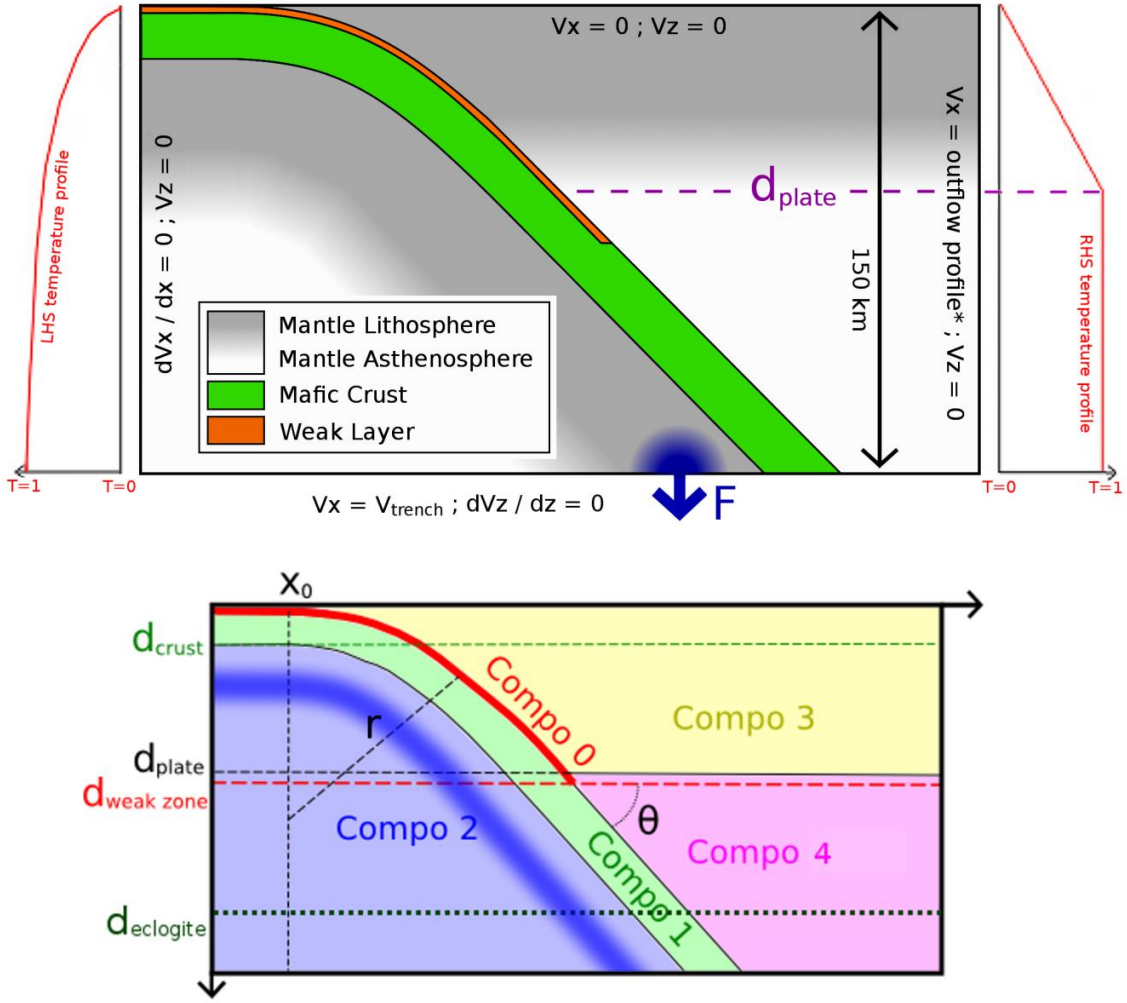

Figure 2.1 Schematic of the model setup. Top Panel: mechanical boundary conditions are written in black on their respective boundaries. Thermal boundary conditions are plotted in red to either side of the plot. The area over which the artificial slab pull force (see Section 2.2.5) is applied is schematically highlighted in dark blue. Bottom Panel: a more technical schematic primarily outlining what value is given to tracers at different points in the model, see Section 2.5.4 for more details. Compo 0, 1, 2, 3 and 4 define the weak layer, subducting crust, subducting mantle, over-riding plate and mantle wedge respectively. All "Compo 0" tracers become "Compo 1" tracers below $z = d_{weak\ zone}$, otherwise known as the decoupling depth. x_0 and r define the initial geometry of the slab, although this is largely unimportant due to the Implementation of an initialisation step (see Section 2.2.2). It is important to distinguish between over-riding plate and mantle wedge for the sake of initialisation, as during this stage the over-riding plate is weakened. Crustal material (Compo 1) is given a different density to the rest of the model. A step-wise increase in this density occurs at $d_{eclogite}$. Compo 2 is used to determine where the artificial slab pull force is applied, a band of tracers, just below the subducting crust, highlighted in a darker blue, are marked for this purpose.

Symbol	Description	Units	(Default) Value
u	Velocity field	ms^{-1}	-
T	Temperature field	°C	-
t	Time	s	-
κ	Thermal diffusivity	m^2s^{-1}	$8x10^{-7}$
P	Pressure field	$JK^{-1}mol^{-1}$	-
η	Viscosity field	Pa s	-
g	Acceleration due to gravity	ms^{-2}	9.8
ρ_0	Reference density (density of the mantle)	kgm^{-3}	3300
α	Thermal expansivity	K^{-1}	$3.5x10^{-5}$
T_0	Surface temperature	^oC	0
$\Delta\rho_c$	Density of material relative to ρ_0 (basalt / eclogite)	kgm^{-3}	-300 / 200
C	Compositional field	-	-
h	Model depth (Ch. 5 / Ch. 3)	km	150 / 200
ΔT	Temperature of the mantle relative to T_0 (modern / Archean)	^oC	1350 / 1550
F	Artificial slab pull force	TNm^{-1}	adjusted
η_0	Reference viscosity	Pas	10^{20}
v_{trench}	Velocity of trench relative to mantle below the model domain	ms^{-1}	variable
x_0	Distance from the LHS boundary to the trench (Ch. 5 / Ch. 3)	km	15 / 20
d_{crust}	Thickness of the incoming crust (modern /Archean)	km	7 / 15
d_{plate}	Thickness of the over-riding plate	km	variable
$d_{weakzone}$	Decoupling depth	km	variable
$d_{eclogite}$	Eclogitisation (densification of the crust) depth	km	variable
r	Initial radius of curvature of the slab (Ch. 5 / Ch. 3)	km	150 / 200
θ	Angle of subduction	^{o}	variable
t_{slab}	Slab age	Myrs	variable
$\eta_{weakzone}$	Viscosity at the centre of the weak zone	Pas	10^{20}
η_{max}	Maximum viscosity	Pas	10^{24}
η_{disl}	Viscosity resulting from dislocation creep only	Pas	-

η_{diff}	Viscosity resulting from diffusion creep only	Pas	-
η	Effective viscosity	Pas	-
$\dot{\varepsilon}$	Stain rate	s^{-1}	-
A	Rheological pre-factor	$Pa^n s$	variable
E	Activation energy	$Jmol^{-1}$	variable
n	Stress exponent	-	variable
R	Gas constant	$JK^{-1}mol^{-1}$	8.31
T_{abs}	Temperature in kelvin	K	-

Table 2.1 A description of all symbols used in Sections 2.1 and 2.2 and model defining properties along with their units and values where applicable.

For use in Chapters 3, 5 and 6, we set up a 2D model of an established subduction zone. Figure 2.1 is a schematic of the model setup. It consists of a slab with an oceanic crust on top, subducting underneath an over-riding plate with a weak layer decoupling the two plates (see Section 2.2.4). All materials and the weak layer are defined using tracers (see Section 2.5.4). The slab is run through an initialisation stage to allow it to find its stable (pseudo) steady state geometry (see Section 2.2.2).

2.2.1 Model Domain

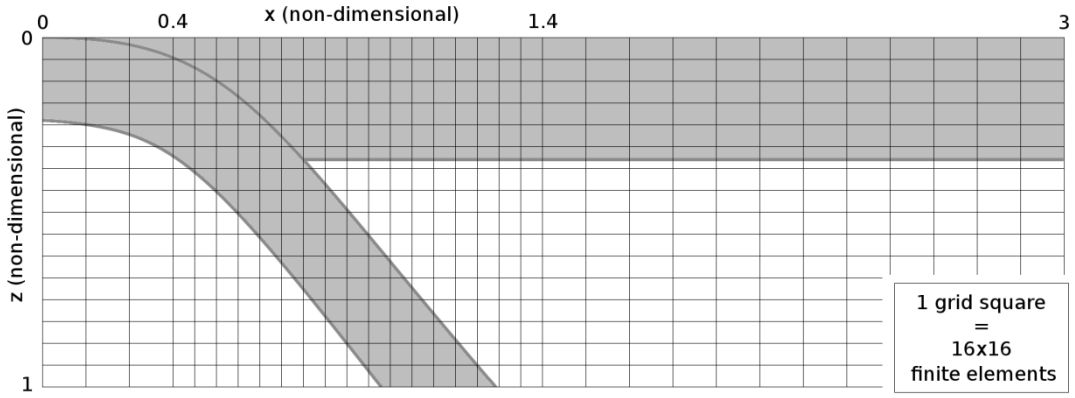

Figure 2.2 The finite element mesh used. The approximate position of the mantle lithosphere, in a typical model, is highlighted in grey.

The different studies use modelling domains of different dimensions but all models have the same number of elements: 256 vertically and 512 horizontally. They also all have the same model aspect ratio: 3:1 (x:z). The mesh used is Cartesian and undeformable (Eulerian) and is refined in the same way in each. Elements to the left of the trench have an aspect ratio of 2:1 as well as elements to the right of the slab, with elements in between (the region of interest) with a 1:1 ratio (Figure 2.2).

2.2.2 Initial Conditions and Initialisation

The initial thermal structure of the slab is that of a half-space which has been cooled from above for a certain length of time: the slab "age" (A). This is analytically calculated to be (Turcotte and Schubert, 2014):

$$T(z) = \Delta T \operatorname{erf}\left(\frac{z}{2\sqrt{\kappa A}}\right) + T_0$$

Equation 2.10

Symbols used in this equation are given in Table 2.1 and erf is the error function. The over-riding plate has the linear thermal profile of a long established plate, which has been both cooled from above and warmed from below (by mantle wedge flow and perhaps small scale convection). It is characterised by a thickness (quoted for each study).

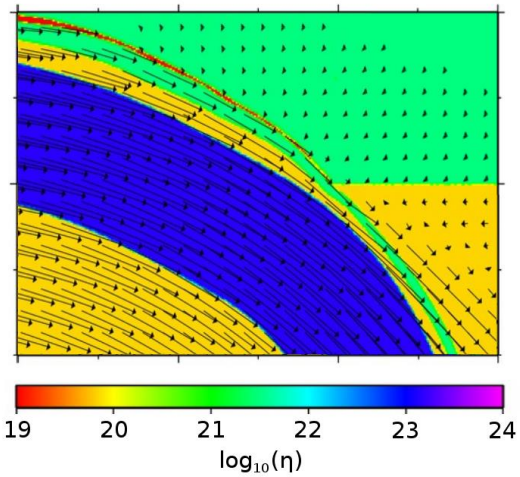

Figure 2.3 Model results from a preliminary model, which demonstrates the need for an initialisation stage. The upper and lower crust are given fixed, low viscosities. The initial radius of curvature given to the slab is too tight and as the slab naturally "straightens" the necessary deformation needed to achieve this is accommodated in the weakest layer: the subducting crust. By increasing crustal strength and decreasing over-riding plate strength whilst the model initialises, we overcome this problem.

The prescribed initial geometry of the slab is not necessarily the geometry that the slab would have in a (pseudo) steady state situation. This means that the slab is subjected to stresses, which a subduction system in steady state would not be subjected to in reality. When the slab is topped with a weaker layer (i.e. the crust), deformation due to these stresses is accommodated in this weak layer. Figure 2.3 depicts the model in a preliminary development stage, which demonstrates this problem. The remedy to this problem is to run the model through an initialisation period, where the crust is given a fixed, moderately high viscosity and the over-riding plate weakened, so that strain is accommodated in the over-riding plate while the slab finds its steady state geometry. The termination of this stage of initialisation is done automatically as soon as the entire initially prescribed slab has left the model domain. This is achieved via the use of tracers (explained further in Section 2.5.4). The model is then run through a second, main stage where the over-riding plate is given its proper rheology and the crust that is currently in the model domain is kept at a uniform high viscosity. During this stage new crust which enters the model is given its proper rheology (Figure 2.4b). Running the slab though such initialisation stages also ensures that the subducting and over-riding plates start the main model run with (pseudo) steady state temperature profiles. Figure 2.4 presents a pair of model snapshots from such initialisation period.

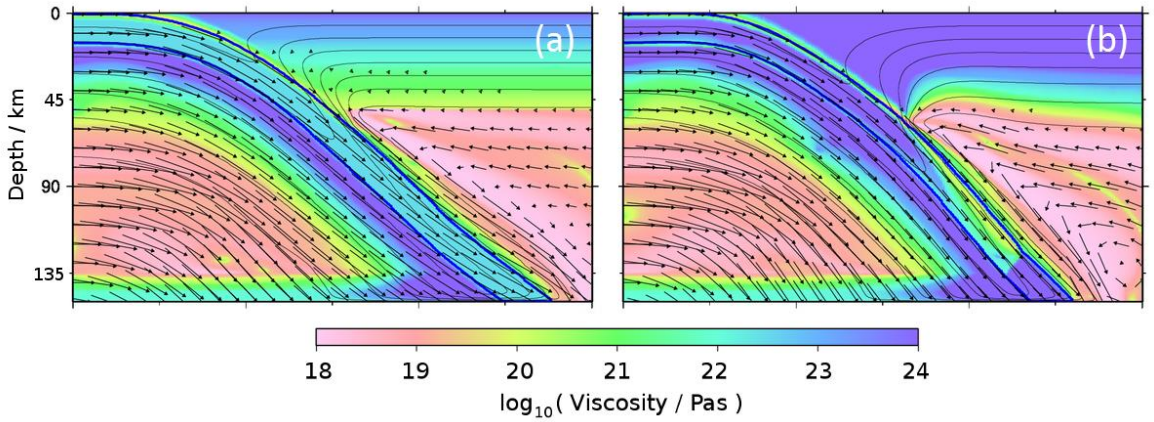

Figure 2.4 Model snapshots which demonstrate the initialisation process in action. (a) is the beginning of the first stage, where the crust (outlined in blue) is given a fixed viscosity and the over-riding plate is weakened to allow the slab to find its natural stable geometry. (b) is towards the end of the second stage where nearly all crustal material of uniform and high viscosity has exited the model domain and been replaced by crustal material with the desired rheology. During the second stage the over-riding plate is given its proper rheology. The thermal profile is in pseudo-steady state by this point (the 200^{o}C isotherms, plotted in black, are stable). Another feature seen in these plots is where the lowest 10 km of the slab mantle is given a diffusion-creep-only rheology to prevent the artificial slab pull force lowering the viscosity leading to unrealistic slab break-off.

2.2.3 Boundary Conditions

Thermal boundary conditions are all fixed temperature (Dirichlet). They are 0°C at the top, and mantle temperature at the bottom boundary (1350°C in "modern day" models). The right hand side boundary has the same thermal profile as the initial condition for the over-riding plate and the left hand side boundary has the same thermal profile as the initial condition for the slab (see Section 2.2.2 and Figure 2.1).

Mechanical boundary conditions are different on different boundaries. They are zero velocity, both horizontally and vertically, on the top boundary. The bottom boundary has a fixed horizontal velocity, chosen to keep subduction at a fixed angle (see Section 2.2.5), and has zero vertical stress ($\sigma_{zz} = 0$), allowing material to freely move in and out through this boundary. The right hand side boundary has a fixed velocity: vertically zero and horizontally the velocity is linearly interpolated between zero, at the base of the over-riding plate, and the velocity of the bottom boundary, at the bottom boundary. The left hand side has zero velocity vertically but zero stress horizontally ($\sigma_{xx} = 0$). This allows the slab to freely enter through this boundary, driven only by the applied slab pull force (see Section 2.2.5). However, this zero stress side boundary does require some care taken in its implementation, and this is further discussed in Section 2.4.

2.2.4 Weak Layer

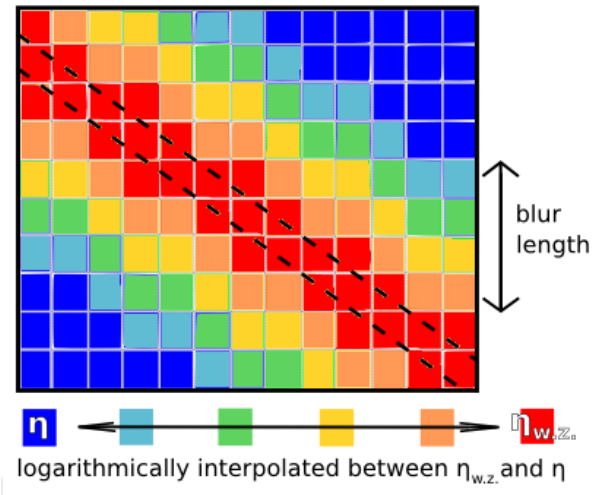

Figure 2.5 A diagram depicting our implementation of a "blurred" weak layer. The elements are outlined by the grey grid. The viscosity of an element is depicted by its colour, red being the weak zone viscosity and blue the background viscosity at that point in the model, determined by the governing flow law in that region. Weak zone tracers (see Section 2.5.4) can be found between the dotted lines. Any element which contains at least one weak zone tracer is given the weak zone viscosity. The viscosities of elements within a "blur length" (in this diagram the blur length is 4 elements though this varies depending on the model) of a weak zone element (vertically) are given an intermediate viscosity such that the viscosity increases exponentially from the weak zone to the background viscosity over this blur-length.

It is believed that to achieve single-sided subduction as we observe on Earth today, a decoupling weak zone needs to be maintained between the two plates (Gerya et al., 2008). What the weak zone actually is in reality is debated. Near to the surface it is primarily the thrust fault. At depth, compositional differences may also play more of a role in weakening; it has been suggested that subducted sediments are in part responsible (Shreve and Cloos, 1986) and also perhaps slab dehydration leading to serpentinisation of a subduction "channel" just above the plate (Gerya et al., 2002). In our models this weak zone is a weak layer, defined by tracers (see Section 2.5.4). The layer of tracers which define the weak zone is thin (<1 km). All finite elements which contain at least a single weak zone tracer are given the "weak zone" viscosity (a variable in our models, typically 10^{20} Pas). This is then interpolated to the background viscosity over a certain number (again, variable) of finite elements, vertically both above and below, to give the weak zone a certain thickness (quoted in the individual research chapters). This is depicted in Figure 2.5. This has the advantage of dramatically increasing numerical stability and may even resemble reality more closely than a discrete layer of fixed viscosity.

2.2.5 Driving Subduction at a Fixed Velocity and Angle

We aim to drive subduction as realistically as possible. In reality it is thought that subduction, and indeed all of plate tectonics, is primarily driven by slab pull: the negative buoyancy force of cold lithospheric slabs in a relatively hotter mantle, transmitted up the rheologically strong core of the slab (Forsyth and Uyeda, 1975). As such, we drive subduction via a vertical body force that we apply to an area within the cold portion of the slab near the bottom boundary of the model. Figure 2.1 schematically illustrates how the area that this force is applied over is determined and this is further explained in Section 2.5.4. The force is introduced into the calculations by simply increasing the density of material in this area. This force is then adjusted by a fixed amount each time step: increased if the slab velocity is below the target velocity and decreased if above. This ensures that subduction continues at an approximately constant velocity throughout the model run. This is ideal for the parametric studies we wish to use this model for, particularly when we want to investigate the effect of subduction convergence rate. We deemed the use of a fixed velocity boundary condition applied to the bottom boundary to be too unrealistic as this also drives mantle flow away from the slab. Figure 2.6 is a plot of the force and velocity through time for a typical steady-state model. In order to prevent unrealistic stresses that may arise due to the application of this technique from affecting the strength of the slab, the subducting mantle is given an approximately equivalent Newtonian, stress-independent, rheology (Christensen, 1984) in an area within 10 km of the bottom boundary (Figure 2.4).

A constant angle of subduction is achieved via the horizontal velocity bottom boundary condition (see Section 2.2.3). We refer to this velocity as the “trench” velocity. This is because the trench remains fixed in our models: the model’s frame of reference is moving with the trench, relative to the mantle below the model. This trench velocity is calculated as the desired subduction velocity multiplied by the cosine of the desired subduction angle.

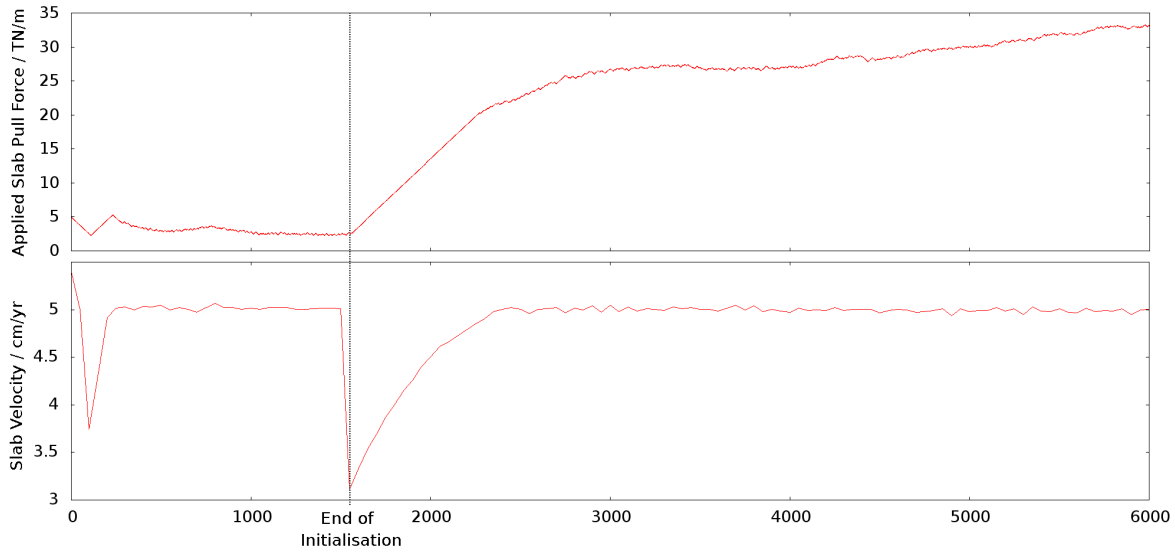

Figure 2.6 The magnitude of the applied artificial slab pull force and the resulting slab velocity throughout the first stages of a typical subduction model with a target velocity of 5 cm/yr. The horizontal axis is in time-steps. The end of the initialisation period is marked (see Section 2.2.2). The velocity at the end of initialisation dips to below 4 cm/yr, which is due to the imposing of the correct viscosities throughout the model at this time. The model recovers by automatically increasing the slab pull force and does so in a few hundred time steps (slab velocity is only below 4 cm/yr for ~200 time-steps). The force required to keep subduction going at a constant speed gradually increases due to the gradual cooling of the model domain from above. As such, the model is in “pseudo” steady state.

A simple benchmark was conducted for the implementation of the slab pull force. The model used is uniform in temperature but contains two materials: a block of highly viscous dense material is placed within an easily deformable lighter material with its base at the bottom boundary of the model. The downward force on the block due to gravity is analytically calculated. The same force is then applied to the block at the boundary, but upwards, using the “slab pull” technique we developed. We observe that the block remains stationary as expected. We then half the applied force and observe that the block begins to fall through the bottom boundary until only half the original block remains, where it comes to rest, again, as expected.

2.3 Rheology

The rheology (the response of a material to an applied stress) of mantle and crustal rocks is of fundamental importance in all geodynamic processes. In this modelling study, we are chiefly concerned with the deformation of materials at the top of the slab and within the mantle wedge, beneath the over-riding plate. In this region it is believed that deformation is dominated by dislocation creep (REF). In a material deforming via dislocation creep, flow occurs due to the movement of crystal lattice imperfections, or dislocations. It is a non-linear, or non-Newtonian, deformation mechanism (Ranalli, 1995) which means that the viscosity is dependent on the strain rate of the material (which in turn is affected by the viscosity). Diffusion creep starts to play more of a role with depth and away from areas of high strain. In a material deforming via diffusion creep, flow occurs due to the diffusion of actual atoms (or vacancies) and is linear, or Newtonian (Ranalli, 1995). Brittle deformation is likely to only start playing a role in materials with temperatures < 450^{o}C (Gerya and Yuen, 2003b). As such, we neglect its effect for model simplicity. Instead we include a maximum, limiting viscosity to 10^{24} Pas in the coolest regions of the model, as a first order approximation (van Keken et al., 2008). This also aids numerical stability by limiting viscosity contrasts.

2.3.1 Dislocation and Diffusion Creep Flow Law

Weakening due to dislocation and diffusion creep is described by the following flow law:

$$\eta_{disl;\,diff} = A^{\frac{1}{n}}\dot{\varepsilon}^{\frac{1-n}{n}} \exp\left(\frac{E}{nRT_{abs}}\right)$$

Equation 2.11

The total resultant viscosity due to the combination of the two deformation mechanisms is:

$$\eta = 1/(\frac{1}{\eta_{diff}} + \frac{1}{\eta_{disl}})$$

Equation 2.12

This is due to the fact the strain rates from the two deformation mechanisms are additive and the viscosity is inversely proportional to strain rate. A is the rheological prefactor, n the stress exponent (1 for diffusion creep, 3-4 for dislocation creep) and E is the activation energy which modulates the effect of temperature on the viscosity. The effect of pressure is not included at it is

assumed not to affect the strength of materials significantly within our relatively shallow model domain. This is exacerbated by the neglecting of adiabatic heating (see Section 2.1.2) which has the opposite effect on the strength of materials. A back-of-the-envelope calculation demonstrates that we expect an increase in the viscosity at the bottom of the model area by no more than a factor of 3 (based on an activation volume of $1.4 \times 10^{-5} m^3/mol$ for dislocation creep (Karato and Wu, 1993) and an adiabatic gradient of 0.5 °C/km).

2.3.2 Determining the Rheological Parameters

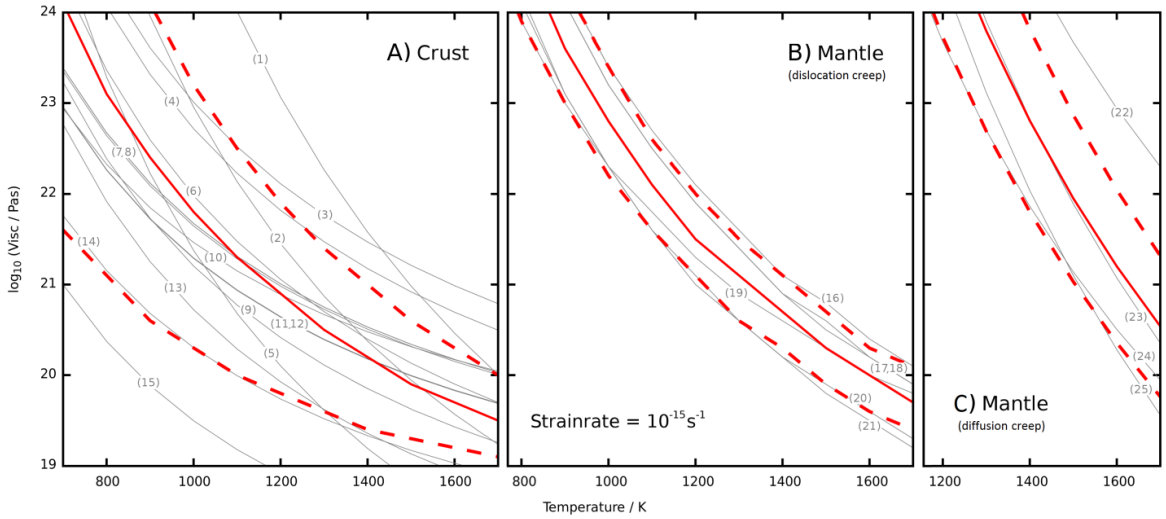

Figure 2.7 Viscosity vs temperature plots for crustal dislocation creep and mantle dislocation and diffusion creep at a strain rate of 10^{-15} s−1. Experimentally derived flow laws are plotted in grey. The labels refer to Table 2.2 where the values for A, E and n, descriptions of the materials being tested and references for the experimental studies are listed. The average flow laws are plotted in solid red with the ±1 standard deviation (of the logarithm of the viscosity) flow laws (k=-1 and k=1) plotted with dashed red lines.

During preliminary work it became apparent that dynamic behaviour in the subduction system was very sensitive to the choice of values for these rheological parameters. The primary way these parameters are determined for crustal and mantle materials is by laboratory experiment. However, these studies can yield estimates that vary; sometimes by orders of magnitude (see Figure 2.7). This is partly due to differences in experimental set up and experimental error but also due to the fact that the materials tested have varying states of hydration (believed to have a significant effect on the strength of materials, though the extent of which is debated (Karato, 2010; Mei and Kohlstedt, 2000)) and also may have a different composition (particularly for crustal materials which vary from sedimentary materials to mafic basalts). We aimed to get the best possible estimate for these properties by compiling many different studies by different

groups for different materials at various states of hydration. A list of the studies we compiled is given in Table 2.2 along with a description of the material being tested and its state of hydration. The viscosities that the different flow laws predict are then calculated at a range of different strain-rates ($10^{10}s^{-1}$ - $10^{18}s^{-1}$) and temperatures (200K – 1700K) and the logarithmic mean of the calculated viscosities ($\bar{\eta}$) is found along with the standard deviation (s) at each strain rate and temperature. A best-fit flow law can then be calculated for the dataset $\bar{\eta} + ks$ where k is an adjustable constant, characterising the material strength of the resulting flow law. This is done by first defining the following quantities:

$$a = \frac{1-n}{n} \qquad b = \frac{E}{n} \qquad c = \frac{\ln(A)}{n}$$

Flow law	**Description**	**Label in Figure 2.7**	**Study reference**
Mantle disl.	Dry, grain size=10mm	17	(Hirth and Kohlstedt, 2003)
	Wet, grain size=10mm	20	(Hirth and Kohlstedt, 2003)
	Dry	16	(Ranalli, 1995) (original (Kirby and Kronenberg, 1987))
	Wet	19	(Ranalli, 1995) (original (Kirby and Kronenberg, 1987))
	Dry	18	(Karato and Wu, 1993)
	Wet	21	(Karato and Wu, 1993)
Mantle diff.	Dry, grain size=10mm	23	(Hirth and Kohlstedt, 2003)
	Wet, grain size=10mm	22	(Hirth and Kohlstedt, 2003)
	Normalised so upper mantle visc.=O(10^{20}) Pas	25	(Ranalli, 1995) (originally (Jaoul et al., 1980))
	As above	24	(Ranalli, 1995) (originally (Houlier et al., 1990))
Crust	Wet quartzite	15	(Ranalli, 1995)
	Plagioclase: An75	11	(Ranalli, 1995)
	Dry quartzite	14	(Ranalli, 1995)
	Diabase	7	(Ranalli, 1995)
	Quartz diorite	13	(Ranalli, 1995)
	Mafic granulite	6	(Ranalli, 1995) (original (Wilks and Carter, 1990))

	Undried diabase	9	(Caristan, 1982)
	Undried microgabbro	5	(Wilks and Carter, 1990)
	Synthetic amphibolite	10	(Hacker and Christie, 1990)
	Garnetite	1	(Ji and Zhao, 1994)
	Eclogite	2	(Ji and Zhao, 1994)
	Dried diabase	4	(Mackwell et al., 1998)
	Dried diabase	3	(Mackwell et al., 1998)
	Partially dried diabase	8	(Shelton and Tullis, 1981)
	Partially dried anorthosite	12	(Shelton and Tullis, 1981)

Table 2.2 A list of the experimental studies used in the calculation of average flow laws for crustal dislocation creep and mantle dislocation and diffusion creep with a description of the material being tested. The numbers in column 3 refer to the labelling in Figure 2.7 and references for the studies are given in column 4.

Flow law	**k (how many SD from the mean)**	**A / $Pa^n s$**	**E / $Jmol^{-1}$**	**n**
Mantle disl	-1	3.62×10^{16}	4.5×10^5	3.47
	0	1.47×10^{16}	4.96×10^5	3.48
	1	5.92×10^{15}	5.42×10^5	3.48
Mantle diff	-1	1.79×10^{10}	3.09×10^5	1
	0	9.04×10^9	3.44×10^5	1
	1	4.62×10^9	2.79×10^5	1
Crust	-1	6.04×10^{21}	1.7×10^5	2.95
	-0.75	1.46×10^{21}	2.06×10^5	2.99
	-0.5	3.37×10^{20}	2.44×10^5	3.03
	-0.25	7.49×10^{19}	2.83×10^5	3.08
	0	1.59×10^{19}	3.23×10^5	3.12
	0.5	6.28×10^{17}	4.06×10^5	3.21
	1	2.03×10^{16}	4.94×10^5	3.31

Table 2.3 Values of A, E and n for different materials and different values of k.

These quantities then linearize the flow law equation (Equation 2.11):

$$\ln(\bar{\eta} + ks) = a\ln(\dot{\varepsilon}) + b\left(\frac{1}{RT_{abs}}\right) + c$$

Equation 2.13

Now linearized, we can use 3D least squares linear regression to find the best-fit flow law for a chosen k (how many standard deviations from the mean flow law). Values for A, E and n can be calculated from the best-fit a, b and c. Table 2.3 contains values of A, E and n for different materials and different values of *k*. Figure 2.7 is a plot of viscosity vs temperature at a strain rate of $10^{-15}s^{-1}$ for different materials. All the used experimental flow laws are plotted, as well as the calculated flow laws for *k=-1*, *k=0* and *k=1* (i.e. flow laws for the mean minus one SD, the mean itself, and mean plus one SD).

Using the range of calculated mantle flow laws gives viscosities on the order of 10^{20} Pas in low strain rate environments at mantle temperatures. This compares favourably with estimates from the analysis of post-glacial rebound: ~$4x10^{20}$ Pas (Mitrovica and Forte, 2004) and from mantle mass heterogeneities and surface observables: ~$2x10^{20}$ Pas (Ricard and Wuming, 1991).

2.4 Handling "Open" Side Boundaries

2.4.1 Single Open Boundary

A horizontally stress-free side boundary condition means material is free to move in and out of the model. Chertova et al. (2012) discuss how using open boundaries should be preferred for subduction modelling as they allow for free flow and, in particular, because they don't lead to forced return flow as in the case of closed boundaries. However, the model behaves as though material beyond the boundary has "zero" buoyancy. In the calculations, the average buoyancy of each row of elements is subtracted from every element in that row as a rescaling to ensure buoyancy values aren't too large (for numerical accuracy). This doesn't affect the behaviour in the model as buoyancy forces are vertical only and as such only lateral buoyancy differences matter. This rescaling means that "zero buoyancy" (neutral buoyancy) is the row average. If the buoyancy of material in the elements next to the open boundary isn't at exactly this average then a pressure gradient will effectively exist and a stress will be experienced by material at the boundary. However, the amount each row of elements is rescaled by is arbitrary. If you choose to rescale by the buoyancy at the open boundary (the left boundary in the case of our models) then elements

at this open boundary now have zero buoyancy (which is the buoyancy of material outside the model). This removes any pressure gradient, meaning that the boundary is now truly stress free and any stresses on the boundary elements arise solely from within the model domain. Figure 2.8 depicts a model of subduction with a stress free left hand side (in-flow) boundary, but without this correction applied. It demonstrates that an unrealistic pressure gradient drives rapid flow beneath the subducting plate.

2.4.2 Multiple Open Boundaries

The method described above does not work for a model with multiple open boundaries unless it is ensured that all open boundaries have the same temperature and compositional profiles. We used this technique in the models used in Freeburn et al. (in review). However, if it is necessary to have different thermal and/or compositional profiles at the open boundaries then another method is needed. Rather than ensuring there is no stress applied to the boundary elements from outside the model domain, one can apply a balancing force. The magnitude of this force at a particular element is calculated by subtracting the integrated buoyancy force of all material above the element from the integrated buoyancy force of all material below the element. However, with only one open boundary in our model we don't need to use this more elaborate technique.

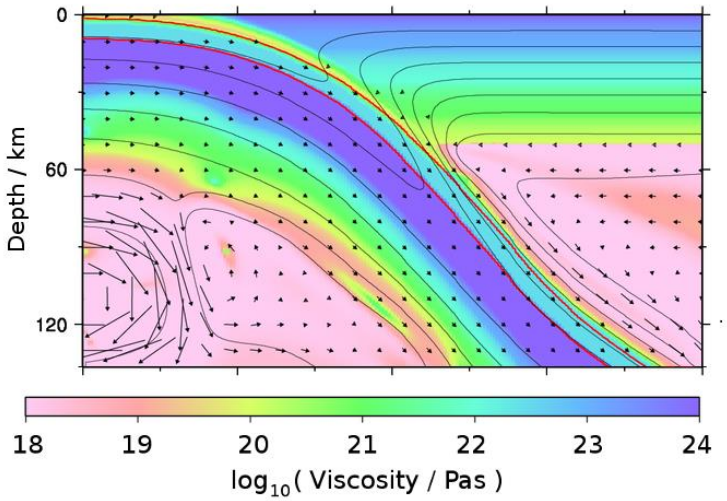

Figure 2.8 A subduction model in its initialisation stage with the buoyancy correction switched off. The left hand boundary is stress free and, without the correction, unrealistic pressure gradients at the boundary drive a rapid flow field beneath the slab.

2.4.3 Benchmarking

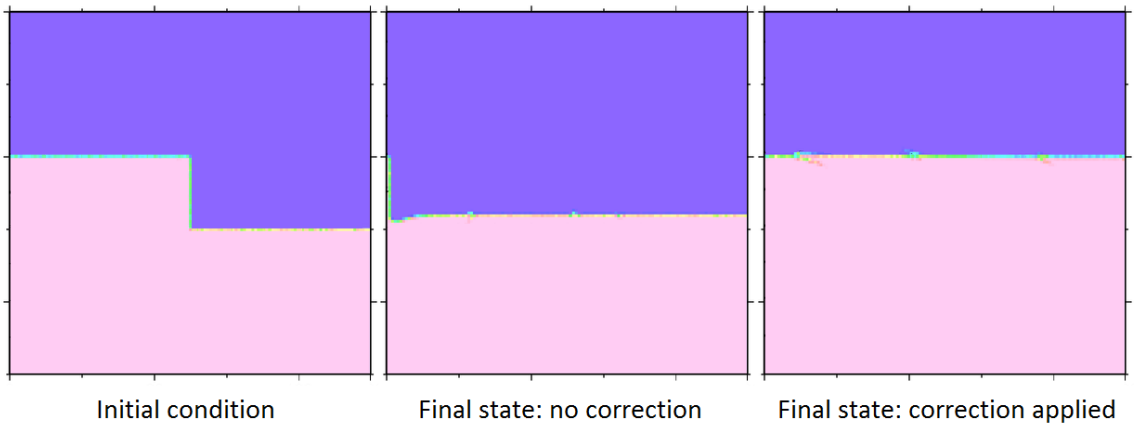

Figure 2.9 Model for testing the operation of an open left hand side boundary (all other boundaries are closed and free slip). Pink material is denser than purple material. When the correction, described in the text, is applied, the material comes to rest at the (upper) level it is at the open boundary, as it would in reality. Otherwise it comes to rest in between the lower level and the upper level as, at any time, material outside the model area, to the left, is treated as having the row-average density.

To ensure that either of the buoyancy correction techniques, described above, work as expected we set up a simple benchmark model. The model is isoviscous, uniform in temperature and contains two materials of different densities. The model starts in a state with the denser material below with the lighter material. The boundary between the two materials is a step function. The left hand side boundary is open and the right closed. Figure 2.9 demonstrates what happens to this model with and without the buoyancy correction. With the original implementation, the final state of the model is with the boundary between the two materials in between the original step function. With the correction applied, the level rises to the level on the left side of the step function and it stays there. The model is therefore now behaving as though material beyond the open (left) boundary is fixed at the same level (the level on the left side of the step function), extending to infinity and independent on the state of material within the model domain.

2.5 Numerical Scheme

2.5.1 Citcom

We use the Cartesian version of the code Citcom (Moresi and Gurnis, 1996; Zhong et al., 2000). This code solves the non-dimensionalised conservation of mass, momentum and energy using a finite element method (see Section 2.5.2) and is parallelised for the efficient running on computer

clusters. The grid used for this method is depicted in Figure 2.2 and is undeformable (Eulerian). The advection and conservation of composition is handled via a marker-in-cell (or tracer) technique (see Section 2.5.4) after the velocity field has been calculated using the finite element method.

2.5.2 Finite Element Method

The finite element (FE) method is a way of finding an approximate solution to a system of partial differential equations (PDEs) over a finite domain given a set of initial and/or boundary conditions via the discretisation of these equations. First, we consider discretisation in time. Looking at our system of three coupled equations, it can be seen that they can be solved in two separate steps. An initial temperature field uniquely defines an instantaneous flow field (the instantaneous stokes flow problem (Hager and O'Connell, 1981)) because the conservation of mass and momentum equations are time-independent. One then approximates this flow field to be constant over a certain small "time-step", and the temperature field is advected (and diffused) according to this flow field over this time-step.

The FE formulation for the instantaneous stokes flow problem is achieved in the following way. The two second-order PDEs are first multiplied by separate "weighting" functions and integrated to put them into their "weak" (or integral) form. The domain is then divided into small "elements" with the vertices of these elements referred to as "nodes". The unknown quantities are then calculated at these node points and interpolated to the interior of the elements via a "shape function" (Hughes, 2012). In Citcom, within each finite element, this shape function is linear for the velocity field and constant for the pressure field (Zhong et al., 2007). By doing this, the PDEs are reduced to the following matrix equations (Moresi and Solomatov, 1995):

$$KV + GP = F$$

Equation 2.14

$$G^T V = 0$$

Equation 2.15

Vector V contains the velocities at all node points, vector P contains the pressure at all the pressure points (pressure is actually calculated at four points inside each element) and vector F contains all driving and boundary forces. K is known as the stiffness matrix and G and G^T are the discrete gradient and divergence operators, respectively. This is a saddle point problem and to

solve this iteratively it is necessary to use Uzawa iteration by combining the above equations as follows (Moresi and Solomatov, 1995):

$$(G^T K^{-1} G)P = G^T K^{-1} F$$

Equation 2.16

Given $G^T K^{-1} G$ (the Schur complement) is symmetric positive-definite, this equation is now solvable via an iterative scheme such as the conjugate gradient method, as used in Citcom. Using an iterative method here has the advantage that computation time can scale almost as order N, the number of unknowns. This is a best case scenario and likely higher in most applications though is certainly less than order N^3 operations, the number required for a direct approach (Moresi and Solomatov, 1995). Less memory is also required. Iterations cease when the velocity and pressure residuals are below certain fixed values: the "accuracies" of the velocity and pressure solvers, which can be set independently (see Section 2.5.5).

The energy equation (advection and diffusion of temperature) is solved using a streamlined upwind Petrov-Galerkin method (Brooks, 1981). This method involves similar steps to those outlined above but with a couple of key differences. Interpolation inherent to the FE method results in artificial "numerical diffusion" of temperature and so the weighting functions are chosen such to counteract this and conjugate gradient isn't necessary to solve the resulting matrix equation (Zhong et al., 2007):

$$M\dot{T} + (K + C)T = F$$

Equation 2.17

The vector *T* contains the temperature at all node points and *M, K, C* and *F* are the relevant mass, stiffness and advection matrices and force vector. This is instead solved using a predictor-corrector algorithm that is explicit and, as such, the chosen time-step needs to satisfy the Courant time stepping constraint to ensure stability.

2.5.3 Non-Linear Rheology

In the case of a model of a material with a linear, or Newtonian, rheology, the above implementation is sufficient. However, when viscosity is a function of the flow field, as it is when using a non-linear rheology (see Section 2.3.1), the stiffness matrix becomes a function of the flow field and an additional level of iteration is required to find a solution. The first non-linear rheology

iteration uses the flow field from the previous time-step to calculate the viscosity field and each subsequent iteration uses the flow field from the previous iteration. A misfit between iterations is calculated and used as a measure of convergence. As this is the outer-most iteration, this can be considered the overall accuracy of the solver which we set to 0.01 for all models.

2.5.4 Marker in Cell Technique

All compositional information is carried and handled through the use of "tracers" (otherwise known as "markers" or "particles") (Gerya and Yuen, 2003a; van Hunen et al., 2002). These tracers are distributed homogeneously and randomly throughout the model domain such that there are many tracers per element. Each time-step, they are advected with the fluid flow. This is done using a second order Runge-Kutta method; the velocity used to advect the tracers being the velocity at the midpoint of the tracer's path during a particular time-step. As the velocity field is defined only on the nodes, this velocity needs to be interpolated from the nodes. This is done in such a way as to obey the conservation of mass (Equation 2.1), i.e. conservatively. This is necessary as it was found that using a simple linear interpolation method results in regions devoid of tracers forming in areas with high velocity gradients (Wang et al., 2015). A prime example of such an area in our subduction model is the decoupling weak-zone.

Compositional information is stored on the tracers in six fields: Compo0-5. Compo0 defines the weak-zone and can take a value of 0 or 1000000 (an arbitrary large number). This is to ensure that any element containing even a single weak-zone tracer is treated as belonging to the weak-zone to ensure continuity. Every time-step it is ensured that all tracers have a Compo0 value of 0 below the decoupling depth (see Figure 2.1). Compo1, 2, 3 and 4 define other areas/materials within the model: the subducting crust, subducting mantle, over-riding plate and mantle wedge, respectively. These can take the values of 0 or 1 (exclusively) except Compo2 which takes a value between 1 and 2 in a band below the subducting crust, for the use in the application of the artificial slab pull force (see Section 2.2.5 and Figure 2.1). Finally Compo5 is used purely to indicate the end of the initialisation period (see Section 2.2.2). An element's worth of tracers at the left (in-flow) boundary, within the top-most slab mantle, are given a value 1 and the point at which the global sum of Compo5 is equal to 0 (i.e. when all material of Compo5 has left the computational domain by subduction through the bottom boundary) marks the end of initialisation.

The compositional information, carried on the tracers, is required for the use in the finite element calculation in the next time-step, as both the density and viscosity of materials in the model are compositionally dependent. This requires an interpolation from the tracers to the finite element

nodes and a system of averaging. This is done by a weighted averaging technique of all the tracers within elements the node belongs to, with the weighting based on the distance between each tracer and the node.

In Chapter 3 we calculate the pressure-temperature (PT) paths of different points in the subducting slab. We use tracers to do this, and this requires temperature to be interpolated from the nodes to the tracers, which we achieve by using a similar method. We then select tracers at fixed points in the slab to report their temperature and position within the model domain to construct PT paths. This assumes that deviatoric pressure is negligible in comparison to changes in lithostatic pressure. We also add an adiabatic heating correction of 0.5^{o}C/km (Turcotte and Schubert, 2014) to the temperature in post processing to these PT paths for later comparing our modelling results to observations and other predictions from other studies.

2.5.5 Optimisation

P accuracy	**Relative V accuracy**	**Lagrange multiplier**	**Time to t-step 40**	**Vrms at t-step 40**	**Time to 2.14 Myrs**	**Vrms at 2.14 Myrs**
0.0001	0.001	1000	42643	221.03	terminated	terminated
0.0001	0.001	10	terminated	terminated	terminated	terminated
0.0001	0.1	1000	4261	221.42	70449	209.80
0.0001	0.1	10	3862	223.01	65094	210.42
0.01	0.001	1000	2962	221.31	34730	212.00
0.01	0.001	10	2713	220.56	terminated	terminated
0.01	0.1	1000	terminated	terminated	terminated	terminated
0.01	0.1	10	terminated	terminated	terminated	terminated

Table 2.4 The computational time a typical subduction model needs, to reach 2.14 Myrs and 40 time-steps on 8 processors. We vary pressure solver accuracy, relative accuracy of the velocity solver (to the pressure solver) and the Lagrange multiplier

Despite the care taken to avoid high viscosity contrasts around the weak zone (see Section 2.2.4), large viscosity contrasts still inevitably occur in a subduction setting (Moresi and Solomatov, 1995). Large viscosity contrasts on the length scale of the resolution of the model can destabilise the instantaneous stokes solver. Steps are taken in Citcom to mitigate against this, such as the

application of a pre-conditioner and the use of an augmented Lagrangian method (Moresi and Solomatov, 1995), modulated by the “Lagrange multiplier” to reinforce the incompressibility constraint (which specifically aides convergence when finding the pressure field). However, in preliminary model runs it was evident that convergence was still an issue and that the adjustment of the target accuracies of the pressure and velocity fields as well as the Lagrange multiplier can have a dramatic effect on convergence rate.

We therefore undertook a brief study to optimise these solver properties. We set typical test models running, identical save for the three solver properties mentioned above. We recorded the time taken to reach 40 time-steps and the time taken to reach 2.14 Myrs as well, as the root mean squared velocity of the model as a test of consistency and reliability. Table 2.4 contains the results. We therefore decided to use values of 0.01, 0.001 and 1000 for pressure solver accuracy, relative accuracy of the velocity solver (to the pressure solver) and the Lagrange multiplier, respectively. Root-mean-squared velocity (Vrms) varies by 1% between the three models which made it to 2.14 Myrs, acceptable given the accuracy of the non-linear rheology solver (the top-most loop) is 0.01.

3 Modelling Slab Temperature: A Re-evaluation of the Thermal Parameter

3.1 Introduction

The thermal structure of subducting slabs has a first order control on many aspects of subduction zones. In particular, slab-top temperature has an important control on the devolatilisation of slabs and therefore the cycling of elements back to the surface via the associated arc magmatism. The pressure-temperature conditions of the slab affect the chemistry of the fluids they release. In particular, in hotter slabs, it is believed that slab top temperatures may exceed the solidus for some subducted materials: primarily subducted sediments, giving rise to particular geochemical signatures (Eiler et al., 2005; Hermann et al., 2006; van Keken et al., 2002). In colder slabs, it is possible that certain hydrous mineral phases within the slab remain hydrous and carry water back to the deep mantle. As such, the overall efficiency of fluid release is slab temperature dependent (Magni et al., 2014; van Keken et al., 2011).

The temperature of slab crust is of particular importance in the study of the formation of the Earth's earliest continental crust. It is commonly thought that higher mantle temperatures in the Archean led to higher slab temperatures and caused the subducting mafic crust to melt more commonly (Martin, 1999). This may give rise to a so called "adakitic" geochemical signature (Kay, 1978), pervasive in Archean rocks but rarely found in arc magmas today. Modern adakites erupt more commonly above particularly young (and therefore commonly believed to be hot) slabs (Defant and Drummond, 1990); evidence that has been used to bolster this slab melt hypothesis.

From a geophysical perspective, subduction is driven by slab pull (Forsyth and Uyeda, 1975) primarily due to the negative thermal buoyancy of slabs and therefore the thermal state of slabs should also have a large effect on the balance of forces within the subduction system and the stress state of the slab (England and Wortel, 1980). As such, slab temperature also influences seismicity within the slab (Gorbatov and Kostoglodov, 1997; Helffrich and Brodholt, 1991); the motion of the trench and therefore stress state of the over-riding plate (Lallemand et al., 2008); and the interaction of the slab with the 660 km transition zone (Agrusta et al., 2017). Another important effect of slab temperature that has recently been suggested and investigated is the possibility of the formation of compositionally buoyant diapirs, or plumes, of slab-derived material that rise through the mantle wedge (Gerya and Yuen, 2003b; Marschall and Schumacher, 2012). There is mounting evidence to suggest that the existence of such plumes and their presence may have a profound effect on the chemistry of arc magmatism (Behn et al., 2011).

Indeed we investigate the formation of these crustal plumes in Chapter 5 of this thesis and demonstrate that these compositional plumes are formed more readily from hotter slabs (Maunder et al., 2016).

Plank et al. (2009) point out that there are two primary methods by which the temperature of a presently subducting slab can be determined: 1) by analysis of the arc magmatism above them, and 2) by forward geodynamic modelling using known physical parameters. We focus here on the latter. Much work has already been done in trying to characterise the thermal profile of slabs, and in particular how this depends on other physical parameters such as the slab age (referred to from now on as "age"), trench normal convergence rate (referred to from now on as "speed") and slab dip angle (referred to from now on as "angle"). The subduction "Thermal Parameter", or $\Phi = t\, v\, \sin\theta$; where t is age, v is speed, and θ is angle, has commonly been used as a first order measure of the internal temperature of slabs (Kirby et al., 1996). Slab top temperature has been predicted to be related to this thermal parameter and depth z above the depth of the base of the over-riding lithosphere: $T = 1/\sqrt{1 + \Phi/z}$ (Molnar and England, 1995; Syracuse et al., 2010). At greater depths, McKenzie (1969) theorised that, due to the heating effect of the overlying mantle wedge, a more accurate expression for internal slab temperature at these depths is given by $T = 1 - (2/\pi)\exp(-(\pi^2/5.38)\, z/\Phi)$. Both these expressions use the thermal parameter and, as such, equally weight the effect of age, speed and angle on the thermal profile.

However, since then, more detailed studies have been undertaken, including the use of numerical simulations. van Keken et al. (2002) uses numerical models to demonstrate there is an existing, but fairly weak correlation between slab temperatures at sub-arc depths and $\log_{10}(\Phi)$. Syracuse et al. (2010) produce numerical subduction models for 52 modern arc segments to determine their thermal profiles. They find that the proposed relationships work reasonably well for slab temperatures at shallow depths and also at greater depths, but fail to give strong correlations in the crucial sub-arc region. Peacock (2003) finds that young and slowly subducting slabs are the warmest and in extreme cases may melt. Magni et al. (2014) show that slab velocity has the strongest control on the thermal structure of slabs and that its effect is not straightforward: faster slabs have colder interiors but hotter slab surfaces. Similar numerical studies have also investigated the effect the thermal state of slabs has on the fate of subducted volatiles (Peacock, 1990) and the feedback the behaviour of volatiles has on the thermal state of slabs (Arcay et al., 2007). Another factor that is likely to play a crucial role is the thickness of the over-riding plate (Currie et al., 2004; Peacock, 2003) which isn't encompassed in the current definition of the thermal parameter.

It has been suggested that certain geochemical signatures do show some correlation with the thermal parameter (Cooper et al., 2012; Ruscitto et al., 2012). However, the correlation isn't

strong and in fact weaker than correlation with other parameters, such as the over-riding Moho depth (Turner and Langmuir, 2015a). This could mean that the thermal state of the slab plays a smaller role in determining the geochemical characteristics of arc magmas or that, for this purpose, the thermal parameter is not performing sufficiently well as a proxy. In this study we re-address the use of the thermal parameter as a proxy for slab temperature at different points within the interior of subducting slabs at sub-arc depths. We also find that the original definition of the thermal parameter performs well for internal slab temperatures deeper in the mantle (~150 km +) but age dominates for internal slab temperatures above this depth and slab top temperatures above the decoupling depth at 70 km. Speed dominates for slab top temperatures below the decoupling depth, arguably the most important region when considering fluid release and arc magma genesis. We also investigate the effect of varying the decoupling depth and find that it does have a dominant control on slab temperature, from the surface to the Moho, as well as within the depth range that it is varied, down to ~40 km below this range.

3.2 Method

3.2.1 Model Setup

A detailed description of the model setup is given in Chapter 2, here we present an overview. This is a 2D model, developed using a Cartesian version of the finite element code, Citcom (Moresi and Gurnis, 1996; Zhong et al., 2000), which solves the coupled equations for the conservation of mass, momentum and temperature whilst assuming incompressibility and using the Boussinesq approximation. Shear heating is not included (see Section 3.4.2). Composition is tracked by tracers which are conservatively advected with the flow field (Wang et al., 2015).

The model is 700 km wide and 200 km deep and consists of 512 x 256 finite elements with horizontal mesh refinement such that an element in the region of interest is 800 x 800 m. As subduction is driven by a negatively buoyant slab which extends to beyond 200 km depth in reality (Forsyth and Uyeda, 1975), we add an additional slab pull force to the down-going slab at the bottom boundary (Maunder et al., 2016). This allows for subduction speed to be controllable. Slab dip is made controllable by applying a variable shear between the top and bottom boundaries (achieved via a fixed velocity bottom boundary condition, or v_{trench}). It has been suggested that, in order to achieve low-angle subduction, such a shear does need to exist (van Hunen et al., 2004), although we recognise that there are other factors which may also play a role and this is a simplification. The left hand side thermal boundary condition is that of a half-space which has been cooled over a certain time: the slab age. We run the model through an

initialisation period until the slab is in statistical thermal equilibrium. Boundary and initial conditions are summarised in Figure 3.1.

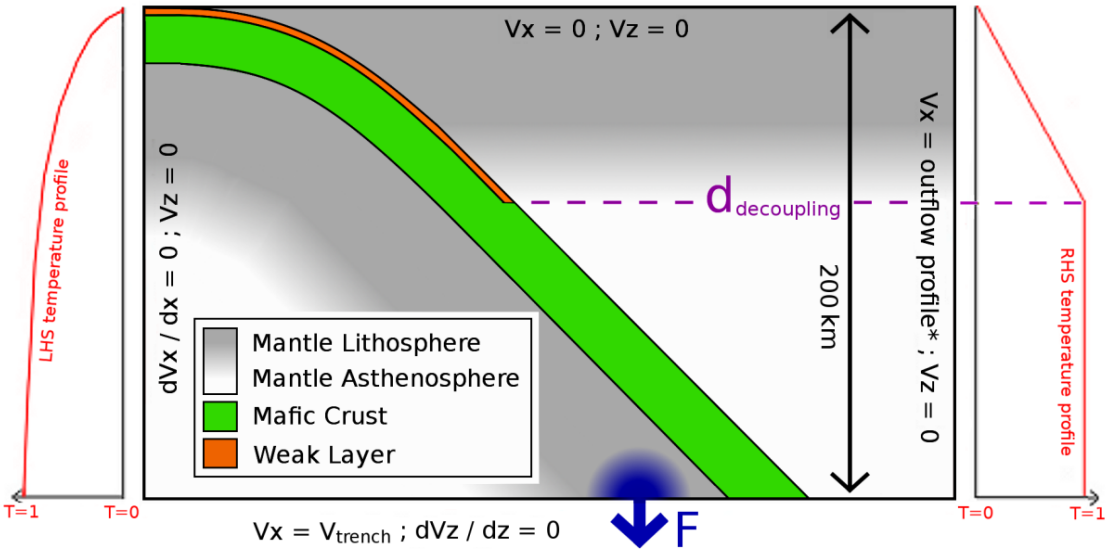

Figure 3.1 Initial positioning of all materials. The left hand side boundary is open, and allows for horizontal inflow of material with a half space cooling temperature profile characterised by the slab age, t. The right hand side boundary has a fixed, horizontal outflow profile with a thermal profile of an older plate, with 0°C surface temperature, 1350°C mantle temperature below the decoupling depth and linearly interpolated in between. A vertical body force is applied to an area within the subducting lithosphere at the base of the model, which is continually adjusted to maintain a constant slab velocity. The top boundary is closed and no slip with a fixed surface temperature and the bottom boundary is open and has a fixed horizontal velocity v_{trench}, set to ensure the plate subducts at a certain angle.*
**outflow profile is zero flux above the decoupling depth then linearly increases to v_{trench} by the base of the model.*

3.2.2 Rheology

Material deforms viscously by diffusion and dislocation creep mechanisms (with no pressure dependence), operating in parallel:

$$\eta = \frac{1}{\frac{1}{\eta_{disl}} + \frac{1}{\eta_{diff}}}$$

Equation 3.1

$$\eta_{diff/disl} = A^{\frac{1}{n}} \dot{\varepsilon}^{\frac{1-n}{n}} \exp\left(\frac{E}{nRT}\right)$$

Equation 3.2

The definitions of the symbols used are given in Table 3.1. Two different compositions are included in this model: (dry) mantle peridotite, and (partially hydrated) mafic oceanic crust (gabbro). The different compositions have different values of A, E and n, which are informed by a detailed literature study and listed in Table 3.1.

A weak zone, which terminates at a fixed decoupling depth (70 km unless stated otherwise) and is defined using tracers, decouples the two plates (Figure 3.1). Its viscosity is fixed in the centre at 10^{20} Pas and logarithmically increases to the background viscosity over a fixed distance: ~5 km at the top of the model which reduces to ~2 km at the decoupling depth to minimise the effect of the weak zone on the mantle wedge dynamics. Brittle yielding is not included as it is deemed not to play a significant role in our region of interest: the subducting crust and overlying mantle, below the over-riding plate. Instead, we impose a maximum viscosity of 10^{24} Pas, which limits the maximum stresses achievable within the rheologically stronger regions of the model.

Symbol	Description	Units	(Default) Value
t	Age (slab age)	Ma	-
v	Speed (trench normal convergence rate)	ms^{-1}	-
θ	Angle (slab dip angle)	^{o}	-
T	Temperature	^{o}C	-
z	Depth	m	-
$\dot{\varepsilon}$	Strain rate	s^{-1}	-
$\mathbf{A_{diff}}$ **mantle**	Rheological pre-factor for mantle diffusion creep	$Pa^{-n}s^{-1}$	4.61×10^{9}
$\mathbf{A_{diff}}$ **crust**	Rheological pre-factor for crustal diffusion creep	$Pa^{-n}s^{-1}$	4.61×10^{9}
$\mathbf{E_{diff}}$ **mantle**	Activation energy for mantle diffusion creep	$Jmol^{-1}$	3.79×10^{5}
$\mathbf{E_{diff}}$ **crust**	Activation energy for crustal diffusion creep	$Jmol^{-1}$	3.79×10^{5}
$\mathbf{n_{diff}}$ **mantle**	Stress exponent for mantle diffusion creep	-	1
$\mathbf{n_{diff}}$ **crust**	Stress exponent for crustal diffusion creep	-	1
$\mathbf{A_{disl}}$ **mantle**	Rheological pre-factor for mantle dislocation creep	$Pa^{-n}s^{-1}$	5.92×10^{15}
$\mathbf{A_{disl}}$ **crust**	Rheological pre-factor for crustal dislocation creep	$Pa^{-n}s^{-1}$	7.49×10^{19}
$\mathbf{E_{disl}}$ **mantle**	Activation energy for mantle dislocation creep	$Jmol^{-1}$	5.42×10^{5}
$\mathbf{E_{disl}}$ **crust**	Activation energy for crustal dislocation creep	$Jmol^{-1}$	2.83×10^{5}
$\mathbf{n_{disl}}$ **mantle**	Stress exponent for mantle dislocation creep	-	3.48
$\mathbf{n_{disl}}$ **crust**	Stress exponent for crustal dislocation creep	-	3.08
R	Gas constant	$JK^{-1}mol^{-1}$	8.31
$\mathbf{T_0}$	Surface temperature	°C	0

ΔT	Temperature of the mantle relative to T_0	°C	1350
ρ	Density of the mantle	kgm^{-3}	3300
ρ_{crust}	Density of oceanic crust above $d_{eclogite}$	kgm^{-3}	3100
$\rho_{eclogite}$	Density of oceanic crust below $d_{eclogite}$	kgm^{-3}	3400
d_{crust}	Incoming crustal thickness	km	7.5
d_{plate}	Thickness of the over-riding plate	km	60
$d_{eclogite}$	Depth of the crustal transition from basalt to eclogite	km	100
$d_{decoupling}$	Decoupling depth: the maximum depth of the weak zone	km	70
$\eta_{weak\ zone}$	Viscosity of weak zone	Pas	10^{20}
η_{max}	Maximum viscosity	Pas	10^{24}
h	Model depth	km	200
κ	Thermal diffusivity	m^2s^{-1}	$8x10^{-7}$
g	Acceleration due to gravity	ms^{-2}	9.8
α	Thermal expansivity	K^{-1}	$3.5x10^{-5}$

Table 3.1 Symbols, units and values of properties and model defining constants.

3.2.3 Parametric Study

To investigate the relative importance of age (t), speed (v) and angle (θ) we reformulate the thermal parameter in a way that allows for the relative importance of t, v and θ to be modulated:

$$ATP = t^a v^b \sin\theta^c$$

Equation 3.3

We then use a dynamic, two-dimensional, numerical model of subduction to determine the relative weightings (a, b and c) to optimise this adjusted thermal parameter (referred to as "ATP" from now on) as a proxy for temperatures at different points within the slab. We repeat model runs for different, fixed ages, speeds and angles. The explored ranges for these properties were chosen to be representative of global subduction zones today. This is informed by the global subduction database 'SubMap' (Heuret and Lallemand, 2005) which includes physical data for all unobstructed subduction zone segments (~200 km wide) worldwide. Figure 3.2 shows the distribution of ages, speeds, and angles, along with the mean and standard deviation of each. In

SubMap, subduction angles are given as two measurements: a) between the surface and 125 km, and b) from 125 km downwards. We present two ways of summarising these data: using all measurements (i.e. two angle measurements per subduction segment) or averaging the two measurements for each segment. As the three properties (speed, age and angle) are multiplied together in the ATP, what is important is the ratio (as opposed to the difference) of the value at the top of the explored range for each property, and the value at the bottom. To extract a rough estimate for this quantity from the global data, we fit normal distributions to the data sets for each property and calculate the ratio of the mean plus the standard deviation and the mean minus the standard deviation. This quantity we call the "relative variability" ("rel. var." in Figure 3.2). The values we choose for speed, age and angle are: 3, 6, 9 and 12 cm/yr; 20, 40, 60, 80 Myr; and 30°, 45°, 60 °, 75° respectively. Crucially, these values have similar relative variabilities as the global data: 4, 4 and 1.9.

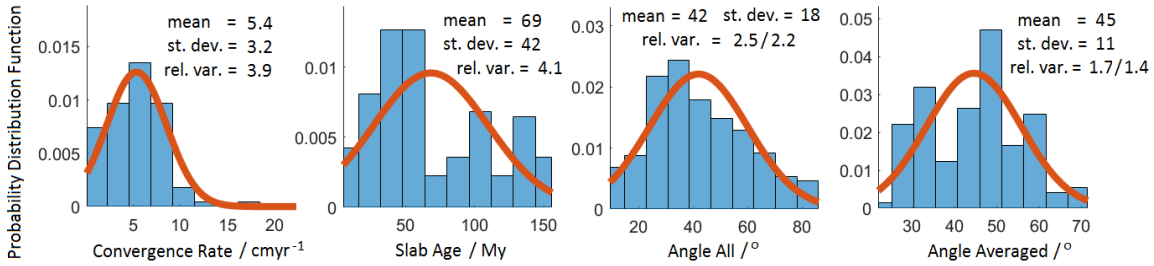

Figure 3.2 Histograms of subduction trench-normal convergence rates (speeds), slab ages and dip angles of ~200 km subduction zone segments as found in the database "SubMap" (Heuret and Lallemand, 2005). Dip angle is calculated in two ways, combining all the angle data (using both measurements: from above 125 km, and below 125 km) and averaging the two measurements in each segment. The red lines are the best fit normal distributions and the mean and standard deviation are given above. The relative variability or "rel. var." is a measure of the spread of the data (see the main text). The method of calculating the factor for each property is described in the main text.

During each model calculation, we track the PT paths through a cross section from the slab surface through the oceanic crust and slab mantle down to 15 km below the slab top. Each model calculation has a definite, fixed age, speed and angle and using these we then calculate a range of adjusted thermal parameters (ATPs) for each model using a range of a, b and c (see Equation 1). A plot is then made of temperature (at a particular point in the slab) versus $\log_{10}(\mathrm{ATP})$, for each combination of a, b and c, and an r^2 value calculated for the strength of correlation. The values of a, b and c that maximise r^2 define the "optimal" ATP. The reason the logarithm of the ATP is used is because it has already been shown by van Keken et al. (2002) that an, albeit noisy, linear correlation exists between slab temperature at different points in the slab and $\log_{10}(\Phi)$. As we take the logarithm of the ATP, only the relative values of a, b and c are of importance as

multiplying all three by the same constant serves only to dilate the plot of temperature vs ATP, leaving r^2 unaffected. This reduces the three-dimensional search space to a surface within this space, which we choose to be:

$$a = 1\,;\ -1 < b < 1\,;\ -1 < c < 1$$
$$b = 1\,;\ -1 < c < 1\,;\ -1 < a < 1$$
$$c = 1\,;\ -1 < a < 1\,;\ -1 < b < 1$$

which, crucially, includes the point $a = 1\,; b = 1\,; c = 1$, for which the ATP reduces to the original definition of the thermal parameter (Φ).

We repeat this same study with an Archean mantle temperature, 1550°C, (Herzberg et al., 2010) and a third time, now keeping angle fixed at 45° and varying the over-riding plate thickness, or rather, decoupling depth (Syracuse et al., 2010; Wada and Wang, 2009), as this is deemed to have a significant effect on the thermal structure (Currie et al., 2004; Peacock, 2003).

3.3 Results

3.3.1 Models of Subduction

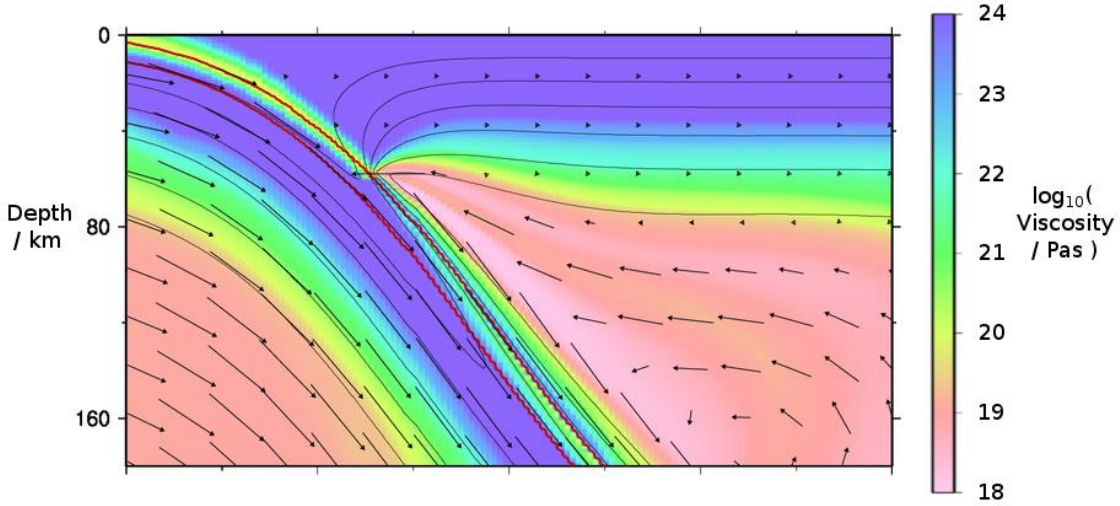

Figure 3.3 A model snapshot of the model with speed = 6 cm/yr; age = 40 Myrs; angle = 45° at the point where the PT paths of the slab are being measured. 200°C isotherms are plotted in black and the oceanic crust, which has a different density and rheology to the rest of the model, is outlined in red. The decoupling point at 70 km is clearly marked as the triple point of slab, over-riding plate and mantle wedge.

All models within the default (present day) study ran to the point where the slab isotherms no longer change significantly with time (thermal "pseudo-equilibrium"). Figure 3.3 is a viscosity profile of the model with speed = 6 cm/yr; age = 40 Myrs; angle = 45° with 200°C isotherms

plotted in black. The flow pattern and position of the isotherms are both approximately stable by this point, at which the PT paths within the slab are measured. However, two models reached a point where the solver failed to converge on a solution, during process of measuring the PT paths, due to high viscosity contrasts. These partially complete models result in the small kinks observed in Figure 3.4 but do not significantly affect other results from here on.

3.3.2 The Effect of Speed, Age and Angle on Slab Geotherms

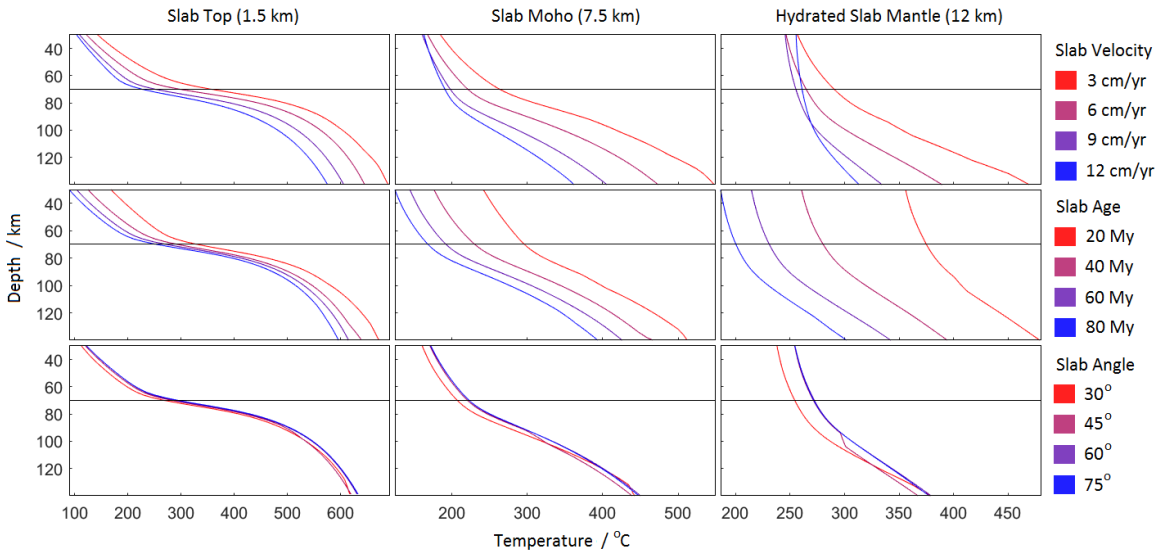

Figure 3.4 The P-T paths of models which share a property (i.e. have the same speed, age or angle) are averaged to produce the P-T paths plotted in this figure. P-T paths for models with like speeds are averaged and plotted as average curves in the plots on the top row. Similarly, like ages are shown on plots on the middle row, and like angles on the bottom row. P-T paths are given near the slab top (1.5 km from the top), the slab Moho (at 7.5 km) and inside the slab mantle (at 12 km). The kinks observed on some P-T paths (particularly apparent in the bottom right panel) arise from the exclusion of data from models which didn't run past a certain point (see main text). As such these P-T paths should be treated as approximate, but still give a good indication of how each property affects slab temperature. Exclusion of this data does not affect further analysis significantly.

Averaging geotherms in models with a shared property (the same slab velocity/age/angle) allows us to gauge how these properties affect the slab geotherm at different points within the slab. These geotherm comparisons are presented in Figure 3.4 for the slab top, Moho and the slab mantle at 12 km below the top. Varying age and speed has a larger effect on slab temperature than varying dip angle. The effect of age is reasonably constant with depth and increases considerably with distance from the slab top. The effect of velocity increases with depth, particularly below the decoupling depth at 70 km, but less so with distance from the slab top.

3.3.3 Finding the Optimal ATPs at Each Point in the Slab

The temperature of the slab at 10 km intervals between 30 and 150 km depth and at 1.5 km intervals from 1.5 km to 15 km into the slab is extracted from the models and used to calculate the optimal values of a, b and c, for these points in the slab. A subset of these optimal values is given in Table 3.2 along with how well the optimal adjusted thermal parameter (ATP) and original thermal parameter (Φ) perform.

Depth / km (from surface)	**Distance from slab top / km**	**Optimal a**	**Optimal b**	**Optimal c**	**Highest achieved r^2**	**r^2 using original T.P.**	**r^2 with age only**	**r^2 with speed only**	**r^2 with angle only**
50	1.5	1	0.8	0.3	0.95	0.78	0.55	0.38	0.02
50	7.5	1	0.2	0.1	0.98	0.61	0.93	0.06	0.01
50	12	1	0.1	0	0.99	0.45	0.99	0	0.01
70*	1.5	0.6	1	0.5	0.94	0.70	0.24	0.67	0.03
70*	7.5	1	0.4	0.1	0.98	0.71	0.83	0.15	0.01
70*	12	1	0.1	0	0.99	0.51	0.98	0.01	0.01
90	1.5	0.5	1	0.3	0.93	0.71	0.18	0.73	0.01
90	7.5	1	0.8	0.2	0.95	0.81	0.56	0.39	0.01
90	12	1	0.2	0	0.99	0.61	0.93	0.05	0.01
110	1.5	0.6	1	0.2	0.92	0.76	0.22	0.67	0.01
110	7.5	0.9	1	0.1	0.95	0.84	0.38	0.53	0
110	12	1	0.4	0.1	0.97	0.71	0.81	0.14	0.01
130	1.5	0.7	1	0.1	0.93	0.79	0.27	0.65	0
130	7.5	0.8	1	0.1	0.95	0.87	0.33	0.61	0
130	12	1	0.6	0.1	0.97	0.84	0.68	0.28	0

*Table 3.2 The values of a, b and c that define the ATP ($= t^a v^b \sin\theta^c$) which maximises the r^2 value of a plot of slab temperature and the logarithm of the optimal adjusted thermal parameter. In the next column is this highest achieved r^2 value. The r^2 value resulting from the use of the original thermal parameter is also given as a comparison as well as r^2 value of plots of slab temperature vs the logarithm of each subduction property, individually. *70 km is the decoupling depth.*

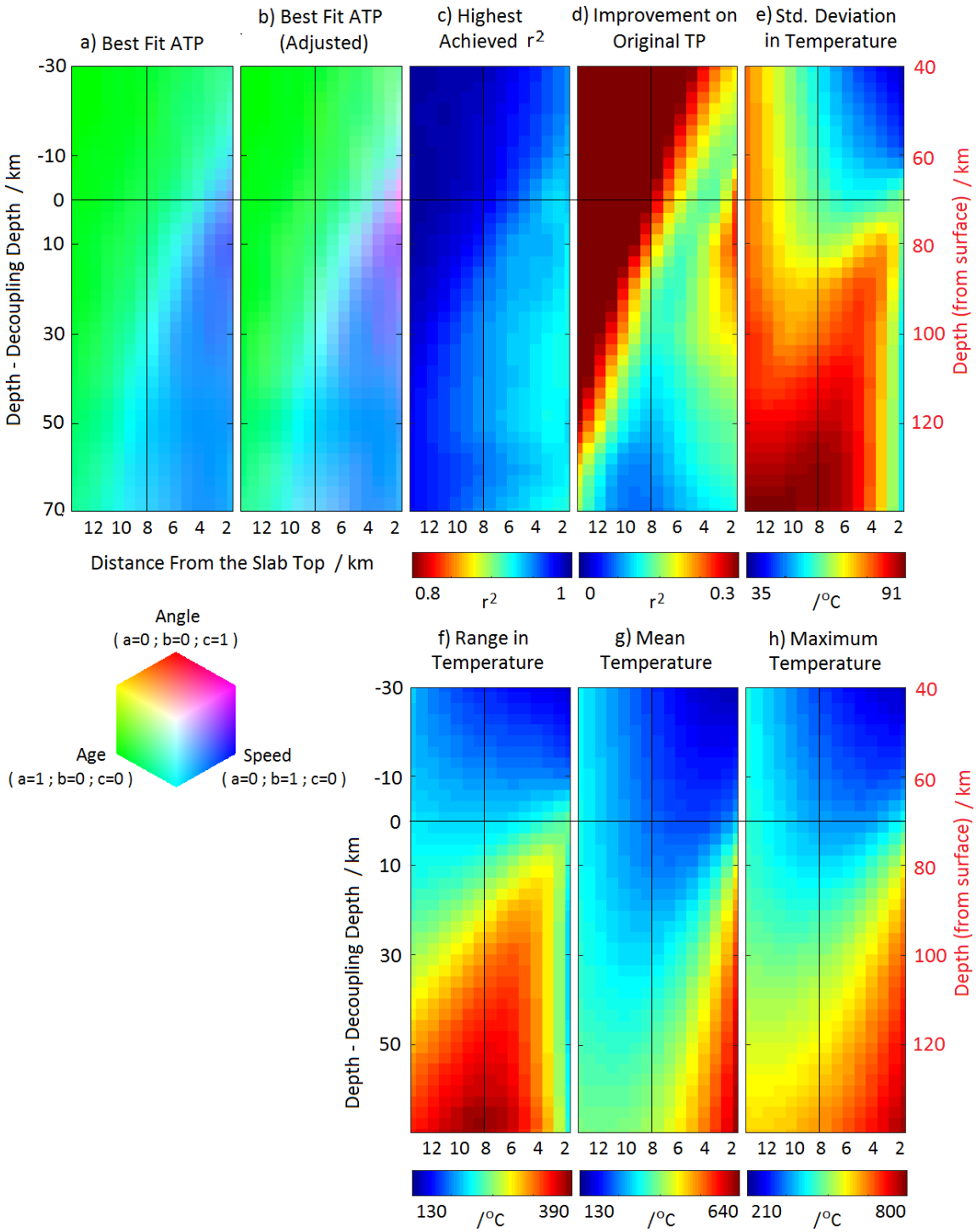

Figure 3.5 Slab cross-sections displaying different information extracted from the models: a) the optimal values of a (age), b (speed) and c (angle) plotted using RGB colour (see the key in the bottom left); b) the same plot but with the optimal values scaled to account for the fact that the angle "relative variability" (a measure of the range of values explored within the parametric study, see Section 3.2.3) is half that of the relative variabilities for age and speed; c) the r^2 value of a plot of slab temperature and the logarithm of the optimal adjusted thermal parameter; d) the difference between the highest achieved r^2 value and the r^2 value resulting from the use of the original thermal parameter, ϕ; e) the standard deviation of the temperature between all the models ran; f) the difference between the temperatures of the hottest and coldest models at that point; g) the mean temperature of all the models; h) the highest temperature found within all the models.

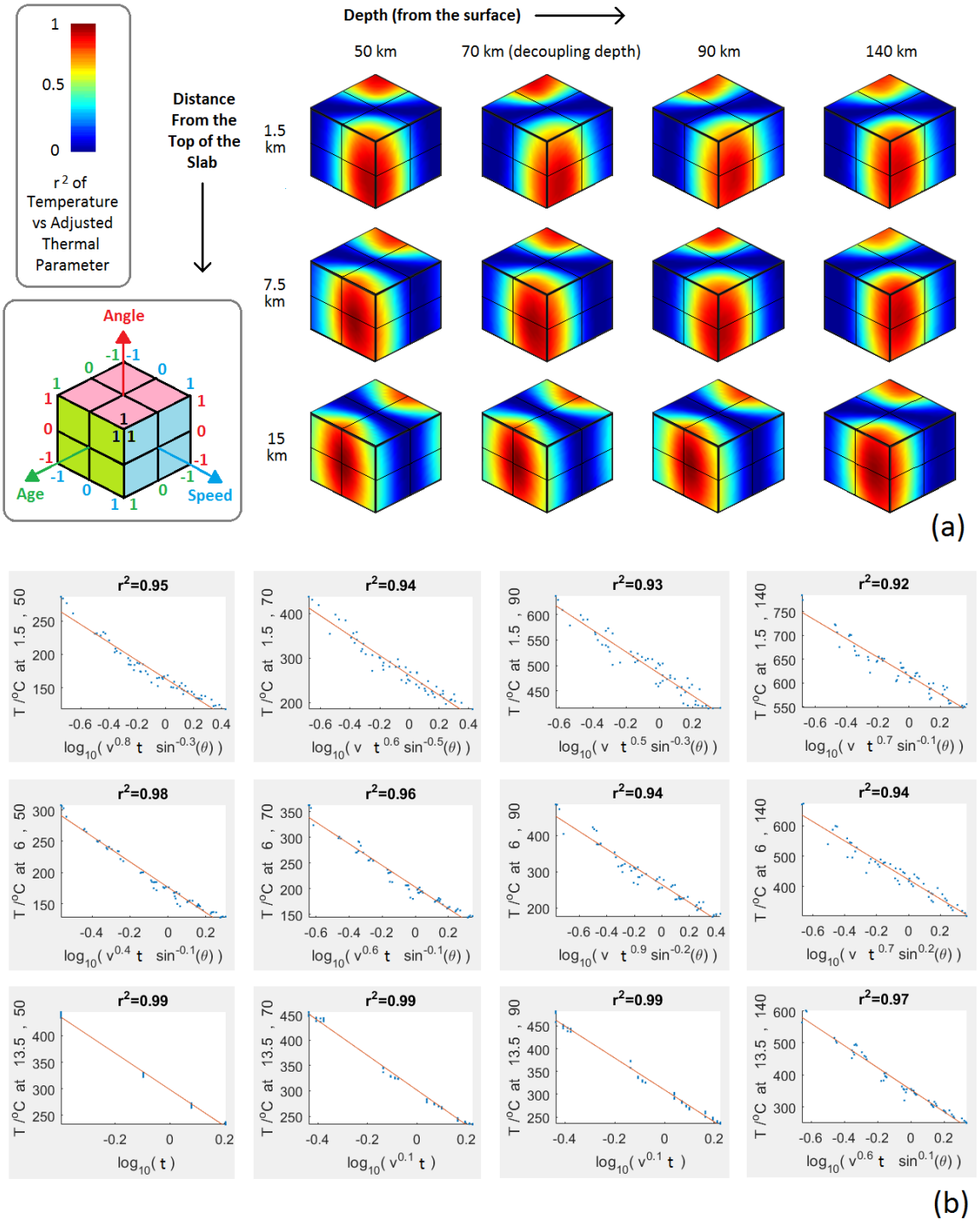

Figure 3.6 The coloured cubes (a) are a graphical representation of the full explored parameter space. The left face is $a = 1$; $-1 < b < 1$; $-1 < c < 1$ *; right face is* $b = 1$; $-1 < c < 1$; $-1 < a < 1$ *and top face is* $c = 1$; $-1 < a < 1$; $-1 < b < 1$, *see the key to the left of these plots to see this pictorially. Red colours represent values of a, b and c which yield high* r^2 *values in plots of the logarithm of the resultant ATP and temperature for certain points in the model (50, 70, 90 and 140 km depth and 1.5, 7.5 and 15 km from the slab surface). These plots are given in the bottom half of the figure (b) for the optimal values (yielding the highest* r^2*) of a, b and c, with the lines of best fit plotted and the resultant* r^2 *given. An intuitive way to interpret the cube plots is as follows: if the centre of the red "bullseye" falls on the left face of the cube then age has the strongest control on temperature, right face: speed, and top face: angle. The width of the bullseye gives an indication of how quickly* r^2 *deteriorates with distance from the optimal values of* a, b *and* c.

For all points tested in the model, we are able to find a best-fit thermal parameter with $r^2 > 0.9$ (Figure 3.5(c)) indicating that our adjusted thermal parameters are indeed good proxies for temperature in these models. Speed and age have a stronger control on slab temperature than angle at all points in the slab (Figure 3.5(a)). The slab seems to consist of two regions: primarily age controlled (*a*>>*b*&*c*), and primarily speed controlled (*b*>>*a*&*c*) closer to the slab top and deeper in the model. The boundary between them starts at the slab top at 5-10 km above the decoupling depth and runs approximately diagonally down to the Moho at 30-40 km below the decoupling depth. The lack of angle dependence is, in part, due to the fact that we explore a greater range of speeds and ages, varying both these properties by a factor of 4 but only varying the sine of the angle by a factor of 1.9 (the "relative variability" described in Section 3.2.3). So, in other words, we don't observe a lot of angle dependence, because the angle simply doesn't vary much across subduction zones. To see how variation of each parameter by the same amount would affect the slab temperature, we can divide the optimal values of *a, b* and *c* by this factor, or "relative variability". To clarify what this means: suppose you are looking at a single subduction system where angle and age varied a small amount compared to speed. It would appear as though slab temperature in this system was controlled by speed and nothing else. This correction adjusts for this, and making this adjustment gives us Figure 3.5(b). It can now be seen that angle plays a more important role at the slab top (<4 km) close to the decoupling depth (+/-10 km), being equally as important as speed in this region. However, what cannot be seen in Figure 3.5 is the fact that this angle dependence is the *opposite* of the angle dependence in the original thermal parameter definition: steeper slabs are hotter around the decoupling point in our models rather than colder as the original thermal parameter ($\Phi = t\, v\, \sin\theta$) suggests. Φ is observed to perform particularly poorly, relative to the adjusted definition, in this region close to the slab surface and decoupling depth, and also at the slab surface below the decoupling depth for ~40 km (Figure 3.5(d)). It performs nearly as well as the adjusted definition, beneath the Moho, deeper that 50 km below the decoupling depth.

It is also important to consider how variable the temperature actually is between the models. Figure 3.5(e,f) shows the standard deviation and the total range in temperature between the models at each point in the slab. Both the standard deviation and range in temperature increase with depth and are highest in the core of the slab, reaching 90°C and ~400°C (respectively) at the Moho, 70 km beneath the decoupling depth. The slab surface has a fairly constant standard deviation of 50-70°C and range of 220-260°C.

Figure 3.6 is a fuller, graphical representation of the results. The three faces of the cube represent the parameter space explored and, as explained in Section 3.2.3, the optimal r^2 value should lie on one of these faces. The width of the bulls eye pattern on the cube gives an indication of how well

constrained the optimal values for the exponents are. If the point with the highest r^2 lies on the top face, then angle is the most important parameter, left face: age, right face: speed. The actual plots of T vs $\log_{10}(\text{optimal ATP})$, with best fit linear regression lines overlain, are also presented in Figure 3.6(b). These demonstrate that a linear relationship between T and $\log_{10}(\text{optimal ATP})$ is a good first order fit.

3.3.4 Decoupling Depth Study

In order to investigate the effect of decoupling depth, we ran the same study but with a fixed subduction angle of 45^o and a variable decoupling depth (40, 60, 80, 100 km). Figure 3.7 presents the results from this study in a similar form to Figure 3.5. Two interpretations of the results are presented side by side: one where temperature is taken at points in the slab that are fixed relative to the surface (so that the surface is fixed in our reference frame; outlined in red) and one where temperature is taken at points in the slab that are fixed relative to the decoupling depth in that particular model (so that the decoupling depth is fixed in our reference frame; outlined in black).

When depth is measured from the surface (Figure 3.7(a)), the decoupling depth has a dominant effect within the depth range over which the decoupling depth is varied (40-100 km) and inside the slab crust, with the decoupling depth being almost entirely responsible for a variation in temperature of up to 300^{o}C (Figure 3.7(g)). As a result, the best fit ATP using just age and speed performs very poorly in this region (Figure 3.7(c)). This dependence diminishes as you travel deeper in the model, with speed and decoupling depth having roughly equal effect in the slab crust at ~140 km depth. Behaviour in the previously "age controlled" region (in the slab mantle) remains roughly the same, indicating that decoupling depth has a relatively minor effect on the temperatures in this part of the slab.

When depth is measured from the decoupling depth, a similar dependence on age and speed is observed as in the set of models with a fixed decoupling depth but with a dependence on decoupling depth over-printed (Figure 3.7(b)). This decoupling depth dependence is nearly uniform with depth, and has a maximum at the slab top, and gradually drops off to zero at the Moho. Defining depth as relative to the decoupling depth not only reduces the effect of decoupling depth, particularly below the decoupling point (Figure 3.7(b,f,h); it also increases the maximum strength of correlation we can achieve at nearly all points in the model (Figure 3.7(c) vs. Figure 3.7(d)).

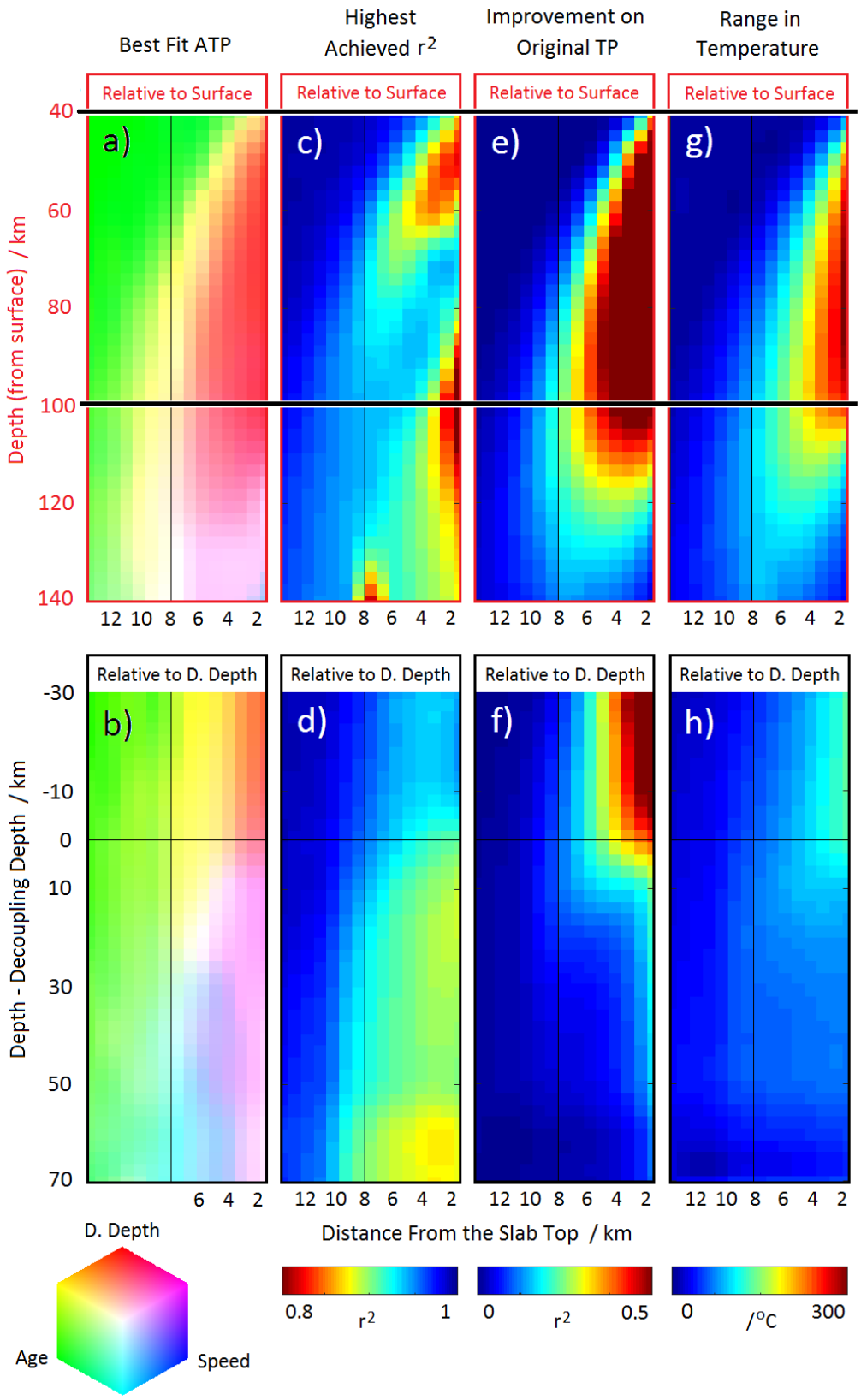

Figure 3.7 As Figure 3.5, but representing the results for the decoupling depth study, in which decoupling depth was varied instead of subduction angle. Two sets of results are presented side-by-side: the first set, where depth is given relative to the surface; and the second, where depth is given relative to the decoupling depth. The range over which decoupling depth is varied is 40 to 100 km. This is highlighted by the black lines in the first set of plots.

3.3.5 Subduction in a 200°C Hotter Mantle (Archean)

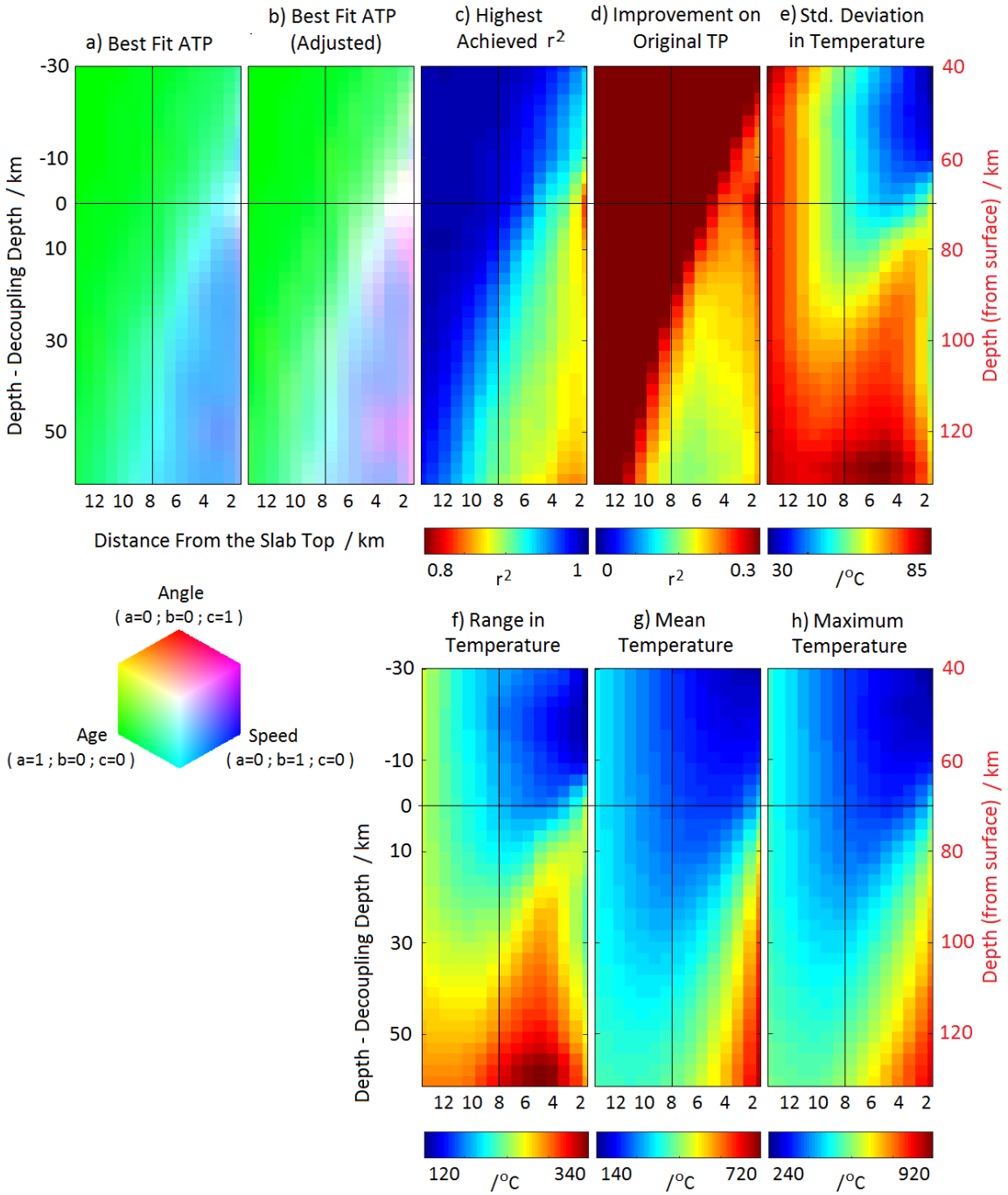

Figure 3.8 A similar plot to Figure 3.5 (therefore see Figure 3.5 caption for a fuller explanation) but representing the results for the study with an Archean mantle temperature. The mantle temperature in this study is 1550°C compared to the original study's 1350°C.

We run the same models (again now with a fixed decoupling depth at 70 km) but with a mantle temperature of 1550°C to investigate its effect on the thermal structure of the slab and, in particular, the optimal ATP. The best-fit ATP is very similar to the modern-day case (Figure 3.8(a)).

However, after performing the adjustment to correct for the use of a smaller range in angle, described in Section 3.3.3, it becomes more apparent that in this Archean model, angle is playing a more dominant role than in the modern day case: angle being as important as velocity for the entire slab top (Figure 3.8(b)). At the decoupling point, age, speed and angle all have equal control on the temperature, however, it is crucial to note that this is not the original definition of the thermal parameter as the effect of angle is opposite in sense, just like in the modern-day case. The best-fit ATP for these Archean models doesn't perform as well as in the modern case, although r^2 is always >0.8 (Figure 3.8(c)). It performs the poorest at the slab top, at the decoupling point, and again when you travel deeper in the model. Despite this, the improvement made on the original definition of the thermal parameter is greater than in the modern case; though, once again, ϕ (the original thermal parameter) performs better the deeper you go (Figure 3.8(d)). The standard deviation and full range in temperatures at each point in the slab is very similar to the modern-day case (Figure 3.8(e,f)). The maximum and mean thermal profiles look similar to the previous profiles but, crucially, with a slab top temperature, below the over-riding plate, that is ~100^{o}C hotter in both cases (Figure 3.8(g,h)).

3.4 Discussion

3.4.1 Improving on the Thermal Parameter

The original definition of the thermal parameter has previously been found to perform well for slab temperatures at 240 km (Syracuse et al., 2010). Our results confirm this: for the slab Moho at depths >140 km the ATP improves on the original thermal parameter by an increase in r^2 of <0.1 (Figure 3.5d). Syracuse et al. (2010) found that the original thermal parameter also works well at 30 km, however, we observe that all parts of the slab above ~60 km (10 km above the decoupling point) are dependent on age and little else (Figure 3.5a). Including dependence on angle and velocity serves to reduce the performance of the proxy. Between these regions, the relative importance of age, speed and angle is more complex. To first order, there are effectively three regions (Figure 3.9):

Primarily age controlled: $T \propto \log\left(t^{-1}v^{-k}\right)$; $0 < k < 0.5$

Primarily speed controlled: $T \propto \log\left(v^{-1}t^{-k}\right)$; $0 < k < 0.5$

Speed and angle sensitive region at and around the decoupling point: $T \propto \log(t^{\sim -0.5}v^{-1}\sin\theta)$

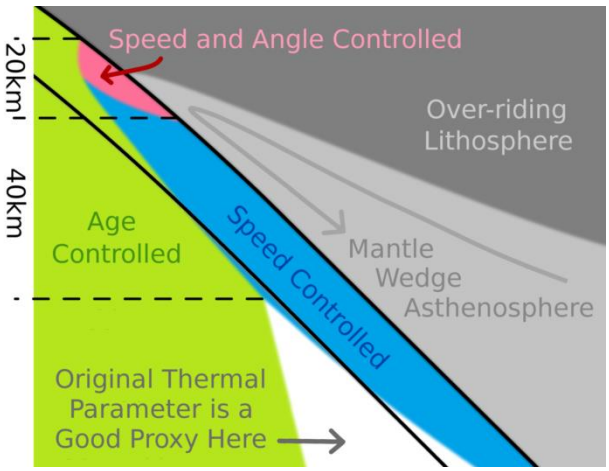

Figure 3.9 A schematic of the first order results of the main study. The coloured regions represent the parts of the slab, the temperature of which is controlled primarily by the parameter(s) labelled. The white region is where the original definition of the thermal parameter is deemed to perform well as a proxy for slab temperature. The top of the slab and the slab Moho (at 7.5 km) are depicted as black lines. The decoupling point coincides with the shallowest point of the mantle wedge asthenosphere (light grey). Horizontal dashed lines represent important depths, the distance between which is given on the left side of the figure.

The line that separates the angle/speed controlled regions from the age controlled region is actually the characteristic conduction length-scale (Turcotte and Schubert, 2014) of a slab that has been heated from the top (starting at 10 km above the decoupling point) and moving at 7.5 cm/yr: the average speed used in our study. This is expected, since age affects the initial thermal profile of slabs and during subsequent subduction, the only way the slab warms from the top is by thermal diffusion from the mantle wedge. Faster slabs will have colder tops relative to slower slabs at the same depth below the decoupling point and this velocity dependence will 'diffuse' into the slab from this point. Angle plays a role near the decoupling point as shallow subduction restricts mantle wedge flow near the decoupling point.

A property not included in the original definition of the thermal parameter is decoupling depth and we have shown that the effect of decoupling depth is potentially strong. When considering temperature with depth from the surface, decoupling depth dominates within the depth range over which it is varied, down to 40 km below this range and all within the previously "speed controlled region". Defining depth as relative to the decoupling depth reduces the effect of varying the decoupling depth considerably, the slab top now being most affected: slabs with deeper decoupling depths have warmer tops at the same depth relative to the decoupling point as they have had more time to warm up. Below the decoupling depth, this effect is of the same order as varying speed and this is for the full range of decoupling depths we explored: 40-100 km. However, it has been suggested that decoupling depths around the world do not vary significantly from 80 km (Furukawa, 1993; Wada and Wang, 2009). If the decoupling depth is indeed nearly

constant, its effect is likely negligible and one would expect the slab parameters: age and speed (and to an extent angle) to have the dominant effect on slab temperatures (Figure 3.9). Turner and Langmuir (2015a) indicate that the nature of the over-riding plate may play a more significant role in determining the geochemistry of arc lavas, though whether this is due to variable decoupling depth is uncertain.

3.4.2 Comparison with Previous Work

Using the slab top geotherms, presented in Figure 3.4, allows us to cross-check with two important numerical modelling studies: Gerya et al. (2002) and van Keken et al. (2002). These two studies use different modelling approaches. Our method of plate decoupling is closest to van Keken et al. (2002), the same model set up subsequently used by Syracuse et al. (2010), and as such our calculated slab top geotherms follow a similar P-T path, but on the cooler end (our mean lies 100^{o}C below that of van Keken et al. (2002)), in part due to our exclusion of adiabatic heating and perhaps in part, due to the fact that our "slab top" is actually at 1.5 km into the slab. It has been shown that these geotherms are already too cold to fit prograde P-T paths of most exhumed ultra-high-pressure-metamorphic rock (Penniston-Dorland et al., 2015), although this may be due to the fact that the exhumation mechanisms necessary for their preservation require anomalous subduction, e.g. slab breakoff during continental collision; or that there is a preservation bias towards hot subduction zones (Abers et al., 2017). Penniston-Dorland et al. (2015) also analyse the effect of speed, age and angle within these modelling results and demonstrate that slab dip has by far the least important effect on slab top temperature, a result we recreate. Age affects slab top temperatures by ~200^{o}C in both the Gerya et al. (2002) and van Keken et al. (2002) studies, roughly consistently at all depths. We observe the same consistency but overall less variation (~100^{o}C). Where our results differ mostly is in the effect of speed on slab top temperatures and this is also something that differs between Gerya et al. (2002) and van Keken et al. (2002). Above the decoupling depth we agree with both studies that slower slabs have hotter tops. We demonstrate that the effect of speed increases with depth, and that below the decoupling depth, it has the dominant effect, with slower slabs being hotter. However, in this region, the results from van Keken et al. (2002) show that speed has a negligible effect and the results of Gerya et al. (2002) show a reversal in the effect of speed at ~50 km. Neither study includes shear heating fully (van Keken et al. (2002) include shear heating along the decoupling interface only), and preliminary work during our investigation indicated that shear heating increases slab top temperatures by <40^{o}C in the fastest model and as such was excluded from our models also. As such this discrepancy must arise from elsewhere. Magni et al. (2014) actually

conclude that faster slabs have hotter tops. However, when they look only 2 km into the slab this is no longer the case. This suggests that the results of this study aren't necessarily at odds with the results of previous work; rather, the simple model depicted in Figure 3.9 breaks down within the topmost kilometre. This topmost kilometre is likely geodynamically complex, with the presence of small scale deformation processes arising from the mechanical interaction between the slab and over-riding plate or mantle wedge. As such, this region can't be modelled reliably using our simplified model setup.

3.4.3 Geochemical implications

In a simplified view, a three layer slab (sediments, igneous crust, and hydrated slab lithospheric mantle) supplies the overlying mantle wedge and the deep mantle with different geochemical components at different depths within the subduction system. The depth of element distillation is primarily controlled by the shape of the isotherms and the overall thermal structure of the slab (Bouilhol et al., 2015). If we consider that the subducting slab lithologies are water-saturated, the sediments will be the first to start to dehydrate, closely followed by the igneous mafic crust, with the hydrated slab mantle being the last to dehydrate, possibly carrying water to the deep mantle (Schmidt and Poli, 2014).

These overall aspects of slab devolatilisation can be put into the perspective of our results, presented in Figure 3.9, and using them we should be able to predict how dehydration depends on slab age, speed and angle (and decoupling depth). Mafic crust is predicted to fully dehydrate between 70 and >300 km and this depends primarily on temperature (Poli and Schmidt, 2002). We show that slab temperatures are predominantly controlled by age above 70 km. As such, one should expect the extreme case, where the crust has fully dehydrated by 70 km, and has lost its fluid content completely to the fore-arc, to apply to the youngest slabs, largely regardless of speed or angle. In the coldest slabs, where significant amounts of hydrated phases would be expected to persist past the decoupling depth and fluids are transported to the sub-arc region, one should expect the depth of crustal dehydration to be primarily speed controlled. For intermediate slabs, where significant dehydration is expected to occur during the near-isobaric increase in temperature encountered at the decoupling depth (van Keken et al., 2002), a dependence on both speed and angle should be expected. However, if decoupling depth is shown to vary significantly, then this should actually control crustal dehydration in these intermediate cases. If dehydration is early enough, this can be too soon for the fluids to be transported to the melt generating region of the mantle wedge and as such would be simply lost to the forearc (Abers et al., 2017; Hyndman and Peacock, 2003). This is important as these first fluids would

carry with them the most fluid mobile elements, depleting them in the arc magma source (Savov et al., 2007). Indeed, in the next chapter we perform a statistical analysis of concentrations of such elements to investigate how they depend on slab age, speed and angle.

The primary dehydration reaction in the slab mantle, and predicted to be the most significant flux of water from the slab, is the breakdown of antigorite serpentine, a reaction which is highly temperature dependent (Ulmer and Trommsdorff, 1995). At ~120 km (50 km below the decoupling point) this reaction occurs at 650^{o}C. This temperature is only achieved in the hottest models; on average the slab is still too cool above 150 km. As such, antigorite breakdown will almost exclusively occur in a region of the slab which is well characterised by the original definition of the thermal parameter. As water transport to the deep mantle is mainly controlled by this hydrated portion of the slab mantle (Magni et al., 2014; Rüpke et al., 2004), it is likely that the original thermal parameter is also a good proxy for deep water transport. Previous studies have also found that both age and speed play an important role in deep water recycling in the same sense (Magni et al., 2014; van Keken et al., 2011). If decoupling depth is shown to vary, the dehydration of the slab mantle will only be slightly affected by decoupling depth and only in the hottest (youngest) cases.

The fluid-present solidus of a typical subducted metasediment lies at ~700^{o}C at the decoupling depth (70-80 km) and increases to ~800^{o}C by 140 km (Poli and Schmidt, 2002). These temperatures are not reached at the top of our average subduction zone (measuring at 1.5 km means that we may be underestimating slightly although sediment layers on the top of subducted plates are typically 0.5-2 km thick (Clift and Vannucchi, 2004)). However, the hottest models do reach these temperatures within the speed controlled region (no models reach this temperature range outside this region). The fluid-present solidus of mid-ocean ridge basalt is similar but slightly higher than the fluid-present solidus of the metasediment (Nichols and Wyllle, 1994; Poli and Schmidt, 2002) and as such, we would only expect the very top-most mafic crust to melt, and perhaps only in the slowest subduction settings and where sediment cover is thin.

Fluid absent melting occurs via the breakdown of hydrous phases at temperatures higher than those recorded in our models (Johnson and Plank, 2000; Skjerlie and Douce, 2002). Bouilhol et al. (2015) demonstrate that the crust should be devoid of fluid by the time it reaches melting conditions and fluid present melting is only achieved via fluxing by fluids derived from the slab mantle below. As discussed above, at what depth the slab mantle dehydrates is dependent on the thermal parameter, and only shallow enough to be within our model domain for the youngest slabs. This may imply that a slab needs to be young and subducting slowly to enable mafic crust or sediment melting. However, melting of crustal material may be enhanced, and fluid absent

melting made possible, by the formation of crustal plumes or diapirs (Behn et al., 2011). This is further discussed in Section 3.4.5.

Perhaps sediment melting does occur on Earth today as indicated by the higher than expected concentrations of the fluid incompatible elements thorium and beryllium in arc lavas (Behn et al., 2011; Johnson and Plank, 2000). Our results indicate, following our previous reasoning, that one should expect sediment melting to be more likely in the slowest subduction zones today, irrespective of angle, although this is perhaps only for slabs which are also young, unless another mechanism facilitates fluid absent melting. Indeed, in the following chapter we demonstrate that the concentration of thorium is indeed convergence rate controlled with a secondary control from slab age (once effects of the over-riding plate are ignored). It has also been suggested that the mafic crust may also partially melt, giving rise to the rare "adakitic" signature (Defant and Drummond, 1990). However, in the following chapter we show that this adakitic signature doesn't correlate with convergence rate at all, but does correlate strongly with slab age.

3.4.4 Subduction in a Hotter Mantle

In the "Archean" models, with a hotter mantle, the same age dominance for the mantle part of the slab is observed. One difference is an increase in angle dependence for the subducting crust, although the boundary between an age controlled and a speed controlled ATP remains roughly the same. Another difference is an increase in average temperatures, particularly at the slab top, while the range in temperatures between different models remains approximately the same: both the coldest and the hottest models have their slab top temperatures increased by similar amounts, ~100^{o}C. This increase in slab top temperature means that the melting of crustal materials would have been more viable in the Archean, although still not ubiquitous (as the average slab top temperature still remains well below 800^{o}C), and still dependent on fluid being present. We therefore agree with Bouilhol et al. (2015) that other mechanisms/processes are required to explain the more pervasive "adakitic" signature in Archean rock (Martin, 1999), such as relamination, as explored in Chapter 5 (Maunder et al., 2016) (see Section 3.4.5).

3.4.5 Other Implications

The seismicity of slabs is known to depend heavily on their thermal structure (Ruff and Kanamori, 1980). Strong correlations between features of deep (>300 km) earthquakes (specifically b-values or number of aftershocks) and the original definition of the thermal parameter have been

demonstrated (Wiens and Gilbert, 1996) as well as the maximum depth of earthquakes (Gorbatov and Kostoglodov, 1997). We have shown here that the original thermal parameter should indeed be a good proxy for any thermally controlled process at these depths. It has also been shown that the seismic moment of the largest characteristic earthquakes within a particular subduction section correlates primarily with slab age (Peterson and Seno, 1984). We propose that this correlation could be due to differences in thermal structure above the decoupling point.

The formation of crustal plumes or diapirs has been suggested to occur in subduction zones today (Gerya and Yuen, 2003b) and subsequent relamination, or underplating, of the over-riding plate with slab derived material (Hacker et al., 2011). This dynamic process would have a profound effect on arc magmatism (Marschall and Schumacher, 2012) and could explain a high temperature sediment melt signature, which is pervasive in many subduction zones (Behn et al., 2011). In Chapter 5 we demonstrate that this process is enhanced under hotter, Archean conditions and also under modern Earth conditions during slow subduction, although age appears less important. In light of the results presented in this chapter, this makes sense as these plumes from the slab crust, below the decoupling point, in the speed controlled region. We would therefore expect to see evidence of relamination occurring predominantly in the Earth's slowest subduction zones.

3.5 Conclusions

We conducted a parametric study using a 2D, dynamic, thermo-mechanical model of subduction to investigate the effects of varying slab age, trench normal convergence rate and slab dip on the thermal structure of the slab. In particular, we evaluate how well the "thermal parameter", ϕ, performs as a proxy for slab temperature at different points within the slab. We find that beyond 50 km below the decoupling depth (the point at which the over-riding mantle becomes coupled to the slab) the thermal parameter performs well as a proxy for internal slab temperature (slab mantle and, as you travel deeper, increasingly the slab crust). We adjust this thermal parameter by modulating the importance of the slab speed, age and angle and find that the temperature dependence of the remainder of the slab can be described well by dividing the slab into three regions. Near the decoupling point (within ~10 km and within the slab crust) temperature depends mostly on speed and angle: steeper, slower slabs are hotter. The temperature of the slab crust below this region primarily depends on just speed: slower slabs are hotter (though age gradually has more of an effect with depth). The temperature of the slab mantle, as well as the entire slab above the decoupling depth, is dominantly age controlled: younger slabs are hotter (although the effect of speed gradually diffuses into the slab with depth). We don't model the top

~1 km of the slab as it is likely too geodynamically complex to be modelled reliably in our large scale model and, as such, we recognise that this region may behave differently.

We also investigate the effect of varying the decoupling depth. This has a dominant effect on slab temperatures, overwhelming the effect of slab parameters, but only within the slab crust and around the depth range of the decoupling depth. However, whether decoupling depth is actually variable in reality is debated. Finally, we investigated the effect of raising mantle temperatures and observe that, even with a mantle that is 200^{o}C hotter, the results of this study do not change significantly. The primary difference is an approximately uniform increase in slab top temperatures by ~100^{o}C in all models.

4 Do the Trace Element Characteristics of Arc Lavas Show Discernible Dependence on the Thermal State of the Slab Below?

4.1 Introduction

It is widely thought that the primary source of typical arc lavas is the mantle wedge above the subducting slab. This is based mainly on their similarity, in terms of major element composition, to other mantle derived magmas formed in different tectonic settings (Plank and Langmuir, 1988). However, the trace element composition reveals features unique to and consistent across arc lavas (Hawkesworth et al., 1994; McDonough, 1991; Pearce, 1982; Pearce and Peate, 1995), commonly referred to as the "arc signature". This signature is best explained by the addition of slab derived fluids to this mantle source (Arculus and Powell, 1986; Tatsumi, 2005) lowering the solidus of the mantle to enable melting and enriching the resulting melts in fluid mobile elements (the large ion lithophile elements, LILEs: Ba, Cs, Pb, Rb and Sr) relative to fluid immobile elements (the high field strength elements, HFSEs: Hf, Nb, Ta, Ti and Zr). Certain arc lavas also exhibit enrichment in elements commonly thought to only be liberated from the slab by the melting of subducted sediment (Th and Be in particular) (Behn et al., 2011; Hawkesworth et al., 1997; Pearce, 1982). It is also hypothesised that certain arc lavas, with high Sr/Y and La/Yb (an "adakitic" signature: indicating the involvement of mafic material at depths >>40 km), may be the result of the addition of partial melts from the mafic subducting oceanic crust.

These trace element characteristics of arc lavas are of particular importance when investigating the formation of the continental crust (CC). It is believed that CC is formed at subduction zones (Davidson and Arculus, 2006) and this is primarily due to the fact that the bulk CC appears to have an arc signature (Taylor and McLennan, 1985). The existence of an arc signature in most Archean rock (van Hunen and Moyen, 2012), in particular Archean TTGs (trondhjemite tonalite granodiorite) (Moyen, 2011), has led many to believe that subduction processes have been the primary CC formation mechanism since this time (Polat, 2012). One key difference between a typical arc lava and Archean CC, is the "adakitic" signature mentioned above (Martin, 1999). This has led many to suggest Archean CC formed via slab melting (Foley et al., 2002) and that perhaps the same process is still happening today at certain locations (Gazel et al., 2015).

The metamorphic reactions that release fluids from the slab are highly temperature dependent (Poli and Schmidt, 2002), as is the solidus of subducting oceanic crust and sediment (Nichols and Wyllle, 1994; Poli and Schmidt, 2002). As such, the efficiency of mantle wedge hydration, and the

chemical make-up of the fluid, should be slab temperature dependent (Plank et al., 2009). It therefore stands to reason that the trace element characteristics of erupted arc lavas should, at least in part, depend on the thermal state of the subducting slab. Another way in which slab temperature may have an effect on arc geochemistry is by affecting the viability of relamination (Hacker et al., 2011), the removal of buoyant material from the slab to form mantle wedge diapirs (Gerya and Yuen, 2003b), which may subsequently melt. It has been suggested that this process is indeed essential to give rise to the sediment melt signature observed in some arc lavas (Behn et al., 2011). During the work that will be presented in Chapter 5, we found that under certain conditions, specifically slow subduction, the mafic subducting crust may also be involved in such a process, potentially giving rise to an adakitic signature (Maunder et al., 2016). As such, it may be that the thermal state of the slab determines whether or not an arc produces crust which resembles CC (Gazel et al., 2015).

The thermal state of the slab depends on a number of physical properties of the subduction system. The slab "Thermal Parameter" $\phi = tv\sin(\theta)$ (where t is the slab age, v is the trench normal convergence rate and θ is the slab dip), is commonly used as a proxy for the thermal state of the slab (Kirby et al., 1996). However, it has been demonstrated that the temperature of slabs in the sub-arc region is rather more complicated (Magni et al., 2014; Syracuse et al., 2010; van Keken et al., 2002). In the previous chapter we used numerical models of subduction to demonstrate that different parts of the slab depend on slab age, convergence rate and slab dip by differing amounts. We also demonstrated that the depth at which the slab becomes mechanically coupled to the over-riding mantle (which determines the reach of the hot mantle wedge) has a very strong control on slab top temperatures. One therefore might expect that trace element concentrations depend on slab age, convergence rate and dip angle, and by different amounts depending on which parts of the slab they primarily come from. In particular, one might expect that any melt signatures should depend primarily on the slab top temperature beneath the arc (and therefore convergence rate) and/or the temperature of the slab mantle (and therefore slab age, and to a lesser extent, convergence rate and angle), which controls the dehydration reactions that supply water to the crust; crucial to lowering the solidus of the crust and sediments to enable melting (Bouilhol et al., 2015). Or, if relamination is necessary to produce these signatures, then one might expect a primarily convergence rate control (Maunder et al., 2016).

Concentrations and ratios of many major and trace elements have been shown to correlate with the thermal parameter globally (Cooper et al., 2012; Turner and Langmuir, 2015b). However, the correlations are weak, or in some cases, as Turner and Langmuir (2015a) point out, stronger correlations exist with the thickness of the over-riding crust. Indeed, over-riding plate control on certain signatures is demonstrated by variations in these signatures above slabs that are constant

in age, speed and angle but above which the over-riding plate varies (Hildreth and Moorbath, 1988; Turner et al., 2016). As for “slab melt” signatures, to bolster the slab melt hypothesis for the generation of adakites, it has been observed that adakites tend to form above slabs that are young (and therefore hot) (Defant and Drummond, 1990). However, while the sediment melt signatures have been seen to correlate with subducting sediment composition (Plank and Langmuir, 1993), they appear independent of slab age, and are prevalent above old slabs too (Elliott et al., 1997). There is also evidence to suggest that, like many other geochemical signatures, the adakitic signature (high Sr/Y and La/Yb) also correlates more strongly with crustal thickness. This might reflect a control from the thermal state of the mantle wedge (Turner et al., 2016), or reflect a control from fractionation processes as the melts ascend through the overriding plate (Macpherson et al., 2006), rather than a slab control.

Here we describe the development of a tool to look for correlations between the geochemical characteristics of arc lavas and the physical properties of their corresponding subduction system. In particular, we design it to look for correlations between ratios of trace elements and the slab parameters. We use a similar analysis technique to the one used in the previous chapter to look for correlations between the thermal state of the slab in numerical models and slab parameters. We design the statistical analysis so that we are confident that the correlations we observe are real features of the data. This is done through the exclusion of outlying data and the calculation of statistical significances, in the form of p-values. The ultimate aim is to use this tool, in conjunction with our results from the previous chapter, to shed light on how much of an effect slab temperature has on the characteristics of arc lavas. We also look for correlations between these element ratios and over-riding crustal thickness for direct comparison to determine whether the correlations with the slab parameters that we do see are artefacts of a correlation with crustal thickness, or not.

4.2 Method

4.2.1 Generation of the Data-set

To find potential correlations between trace element ratios, slab age, slab dip, trench normal convergence rate (referred to as speed from here on) and over-riding crustal thickness we need to combine three global databases: GeoRoc, SubMap and Crust1.0. GeoRoc is a global compilation of geochemical measurements grouped by tectonic setting. We analyse all volcanic arc data. SubMap is a database of physical properties of subduction systems compiled by Heuret and

Lallemand (2005). Crust1.0 is a global map of crustal thickness at a resolution of 1 degree (Laske et al., 2013).

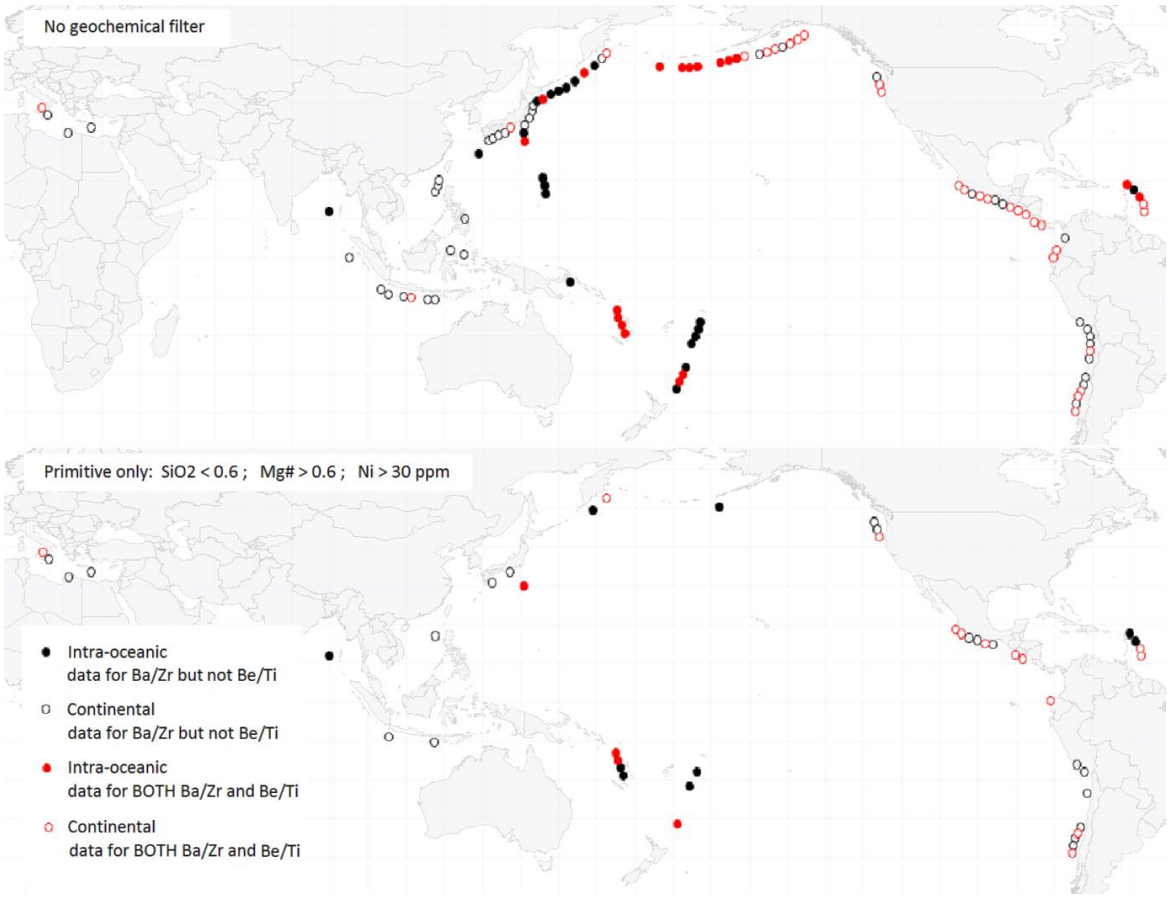

Figure 4.1 Maps of the locations of the subduction zone segments used in this study, in which each circle is a single segment. The top panel shows all the segments used for the element ratio with the most data (Ba/Zr) and for the element ratio with the least (Be/Ti). The bottom panel demonstrates which segments remain when a "primitive lava" filter is applied. Circles are either filled or empty depending on whether the over-riding plate for that segment is continental or oceanic.

The first step we take is to filter GeoRoc for unaltered, quaternary age rocks; making the assumption that today's subduction zones have not changed significantly in 2.5 Myrs. This leaves 18600 entries, though not all entries contain measurements of all element concentrations. Each GeoRoc entry has an associated longitude and latitude which we use, along with k=Crust1.0, to yield a crustal thickness for each entry. These data are then binned into the ~200 km arc segments of the SubMap database. This is done by calculating the distance from every GeoRoc data point to the centre of each SubMap segment and placing each data point in the bin for their closest SubMap segment, discarding all data that are further than 700 km from any segment. The SubMap segments we use include only segments which are deemed to be "unobstructed" by Heuret and Lallemand (2005). Subduction segments where anomalous subduction is occurring are excluded. This is defined as the subduction of seamounts, ridges or continental blocks; subduction

of slabs which are tearing or the edges of slabs. We also only use segments with a full data set: speed, age and angle. Figure 4.1 is a map of segments available for use in this study.

Once the data have been binned, we take the mean of the crustal thickness data and the mean of the logarithm of the trace element concentrations within one segment such that each segment now has one representative value for convergence rate, angle, slab age, crustal thickness and the element ratios of interest. Figure 4.2 shows the crustal thickness, speed, age and angle for each subduction segment.

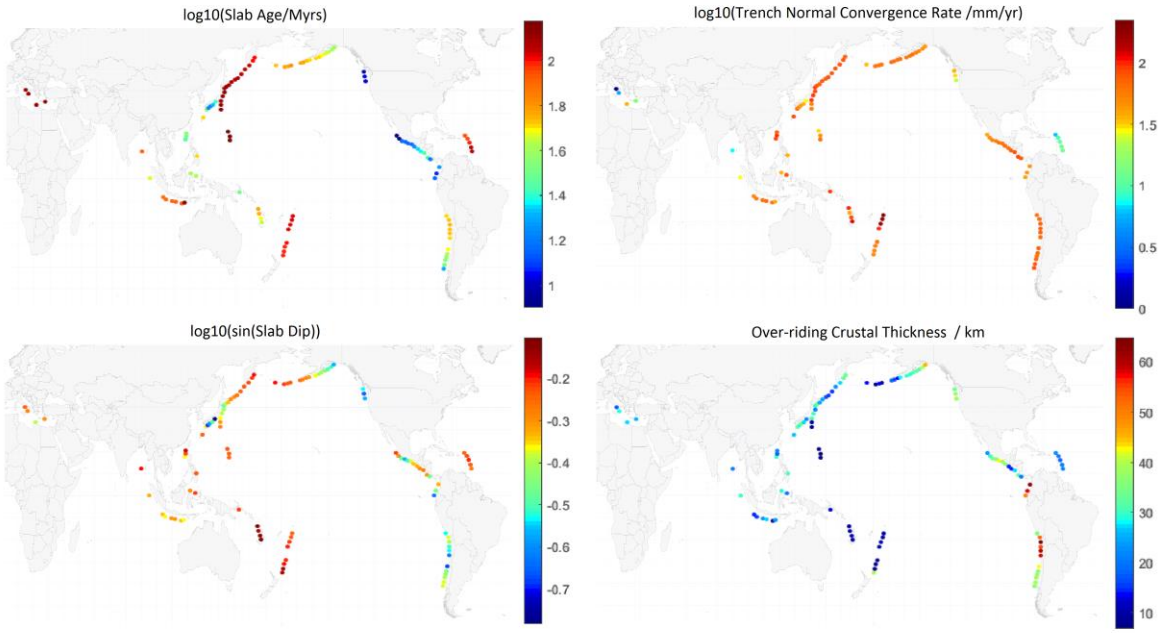

Figure 4.2 The values of age, speed, angle and crustal thickness used for each segment. The crustal thicknesses are calculated using the data for Ba/Zr: the element ratio with data in the most segments. The logarithm of the age, speed and angle is taken as we ultimately end up looking for correlations with the logarithm of the ACP (Equation 4.4).

We take the logarithm of the trace element ratios as they potentially span several orders of magnitude. The trace element ratios we choose to look at are the ratios of the large ion lithophile elements (LILE): Ba, Cs, Pb, Rb and Sr and the high field strength elements (HFSE): Hf, Nb, Ta, Ti and Zr. A high LILE/HFSE is a key part of the "arc" signature used to distinguish rocks formed at subduction arcs from rocks formed through other volcanic processes (Section 4.1). Such arc signatures arise because slab derived fluids, believed to trigger melting of a mantle source above the slab, preferentially leach LILEs over HFSEs, i.e. LILEs are more fluid mobile. We add La and U to our list of numerator elements, as they are also fluid mobile and we also add La, Be and Th. Be and Th are not fluid mobile but are enriched in some arc lavas. This has been hypothesised to be due to sediment melting and, as such, is of interest to us as this should depend on slab top

temperature (Behn et al., 2011; Hawkesworth et al., 1997; Pearce, 1982). We add Y and Yb to our list of denominator elements, being of interest as they are both readily incorporated into the mineral garnet and, therefore, low Y or Yb (or high X/Y or X/Yb) is an indication of the involvement of garnet, a mineral only present in mafic material at great depths (>40 km). Lavas with low Y and Yb are termed "adakitic" (Moyen, 2009). It is debated whether this signature arises during abnormally deep fractional crystallisation (Macpherson et al., 2006) or whether it is an indication that the subducting mafic crust is partially melting and providing a source for the arc magmatism (and as such should also be slab temperature controlled) (Foley et al., 2002).

4.2.2 Filtering the Data-set

It is known that intra-oceanic arcs and continental arcs are fundamentally different and it has been shown that this often has a first order control on the geochemistry of the associated arc magmatism. At intra-oceanic arcs, the over-riding crust is thinner and more mafic and therefore should have less of an effect on percolating melts. It is therefore useful to look at a data set where only intra-oceanic subduction segments are included. These are marked by filled circles in Figure 4.1. The geochemical data can also be filtered by how primitive the lavas are. More primitive (or less evolved) lavas are thought to have been less affected by fractionation and assimilation processes and better represent the source. This is done by applying an upper limit on the SiO_2 content on accepted lavas as well as a lower limit on the Ni content and the Mg number, which is defined as follows:

$$\mathrm{Mg\#} = 100\mathrm{MgO}/(\mathrm{FeO} + \mathrm{MgO})$$

Equation 4.1

However, by applying a stronger filter you remove more data and reduce the statistical significance of the result, and as such there is a trade-off. Figure 4.1 demonstrates the effect of removing all continental segments, and also applying a primitive lava filter, on the amount of data available for the signature with the most data: Ba/Zr, and the signature with the least: Be/Ti.

The final filter applied is one to remove outliers or anomalous results in GeoRoc. To ensure that the trend being observed in the data isn't being artificially enhanced by outliers, all data that are further than three standard deviations from the mean of the geochemical signature are discarded. Filtering steps are shown as red boxes in the flow chart in Figure 4.3.

4.2.3 Analysing the Data-set

The first analysis performed is to calculate the strength of correlation of subduction convergence rate (v), subduction angle (θ), slab age (t) and over-riding crustal thickness (d) each with the element ratios of interest. This is done by plotting the logarithm of the element ratio against convergence rate, angle, age and crustal thickness and finding the r^2 value. It is also important to consider that convergence rate, angle, age and crustal thickness may also correlate with each other for a particular data set and so we also calculate these cross correlations.

The second analysis looks to calculate the strength of correlation of the signatures with the slab "Thermal Parameter", or $\Phi = t\ v\ \sin\theta$. We calculate $\log_{10}(\Phi)$ for each segment and plot this against the logarithm of the signature, because it can span many orders of magnitude and also because it has previously been shown, by van Keken et al. (2002), that an, albeit noisy, linear correlation does exist between slab temperature at different points in the slab and $\log_{10}(\Phi)$.

We demonstrated in the previous chapter that the strength of correlation between slab temperature and the thermal parameter can be significantly improved by modulating t, v and $\sin\theta$, coming up with the following quantity:

$$t^a v^b \sin\theta^c$$

Equation 4.2

In the previous chapter, we varied a, b and c to maximise the r^2 of a log-log plot of this parameter against temperature at different points in the slab within a set of numerical models of subduction. We did this to find improved proxies for temperature within each part of the slab, finding what we referred to as "adjusted thermal parameters". Here we perform a similar analysis, only now maximising the r^2 of a log-log plot of this parameter against each element ratio. We adjust a, b and c to maximise the fit to find what we refer to, as adjusted chemical parameters (ACPs). In the previous chapter, when finding adjusted thermal parameters, we showed that only the relative values of a, b and c are of significance, as multiplying all three by a constant only serves to dilate the plot. The same applies here and we therefore perform the search over the same surface in a-b-c space:

$$a = 1\ ;\ -1 < b < 1\ ;\ -1 < c < 1$$
$$b = 1\ ;\ -1 < c < 1\ ;\ -1 < a < 1$$
$$c = 1\ ;\ -1 < a < 1\ ;\ -1 < b < 1$$

Also discussed in the previous chapter was the effect of using datasets with different ranges. For a particular set of subduction segments, the ages, speeds and angles may vary by different

amounts. A quantity that varies more will have a larger apparent influence on the ACP and we need to normalise this. As these three quantities are multiplied together in the ACP, it is necessary to normalise by the factor by which they vary, i.e. how many times larger the largest value is than the smallest. We define the "relative variability" (F) to characterise this:

$$F = (\mu + \sigma)/(\mu - \sigma)$$

Equation 4.3

in which μ is the mean of the dataset and σ the standard deviation. If a particular subduction property (e.g. angle) has a smaller relative variability than the others, then the ACP will be less sensitive to it, which will be reflected in a reduced value of c. To correct we therefore divide a, b and c by their associated relative variabilities F_t, F_v and $F_{\sin(\theta)}$:

$$ACP = t^{a/F_t} \; v^{b/F_v} \; (\sin\theta)^{c/F_{\sin(\theta)}}$$

Equation 4.4

Once the optimal r^2 value has been found, a p-value is calculated by performing a Monte-Carlo permutation test (Fisher, 1949). The whole calculation is repeated multiple times but with the dataset randomly permutated each time (i.e. data points shuffled randomly). The optimal r^2 value is calculated for the permutated sets and compared to the optimal r^2 of the original dataset. The p-value is then calculated as follows (Makkonen, 2006):

$$p = 1 - (\frac{m}{N+1})$$

Equation 4.5

where m is how many randomly permutated sets yield a lower optimal r^2 than the real set and N is the number of permutations tried. For a "perfect" dataset, where none of the permutations leads to an increase in r^2, this value tends to zero as N is increased. This is only an estimate of the p-value and it can be shown that the fractional error in this estimate obeys the following inequality:

$$\frac{\Delta p}{p} \leq \frac{1}{\sqrt{pN}}$$

Equation 4.6

Permutations are continued until p is either deemed to be above the critical value of 0.05 (95% confidence), or below, to within twice this maximum error.

Figure 4.3 Flow chart summary of the processing on the GeoRoc, Submap and Crust1.0 databases to arrive at the data presented in the Results section of this chapter. This is described more fully in the main text. Data inputs are in white parallelograms, user inputs are in black diamonds, filtering steps are in red boxes, other steps are in blue boxes, and the outputs are in white rounded boxes.

4.3 Results

4.3.1 Cross Correlations

	Crustal T	Age	Speed
Age	0.18 +/- 0.02	-	-
Speed	0.02 +/- 0.01	0.00 +/- 0.01	-
Angle	0.45 +/- 0.04	0.14 +/- 0.03	0.02 +/- 0.01

Table 4.1 The strength of cross correlations (r^2) between age, speed, angle and over-riding crustal thickness (Crustal T). The errors represent the variability from using only segments that have data for different element ratios.

	Crustal T	Age	Speed
Age	0.03 +/- 0.06	-	-
Speed	0.03 +/- 0.01	0.01 +/- 0.02	-
Angle	0.11 +/- 0.08	0.20 +/- 0.05	0.02 +/- 0.04

Table 4.2 The strength of cross correlations (r^2) between age, speed, angle and over-riding crustal thickness (Crustal T) as in Table 4.1, except now only using intra-oceanic segments.

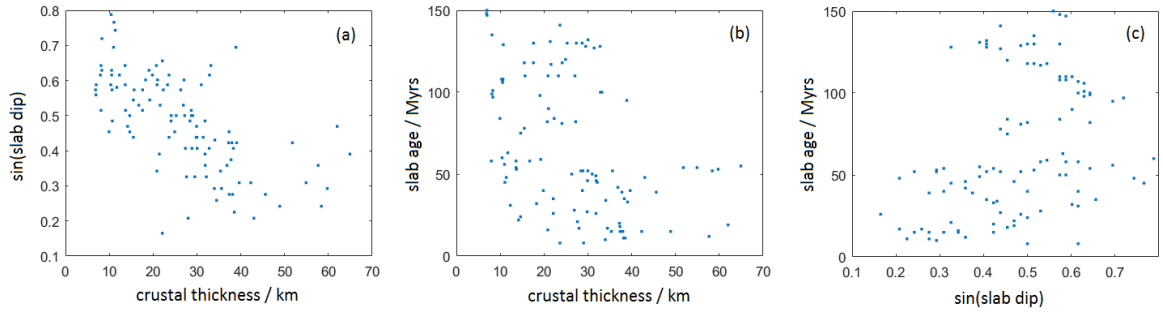

Figure 4.4 Plots of (a) angle against crustal thickness, which negatively correlate; (b) age against crustal thickness, which negatively correlate; (c) age against angle, which positively correlate.

Before interpreting correlations between the signatures and the different subduction zone properties, it is important to know whether cross correlations exist between the properties themselves, as this could produce artificially high correlations where there shouldn't be and have a profound effect on the adjusted chemical parameter study. All cross correlations are given in Table 4.1. Data for element ratios are always available for all subduction segments. So when looking at different element ratios, different sets of subduction segments are available to us. To illustrate this, the difference in the number and distribution of subduction segments when looking

at Ba/Zr and Be/Ti is highlighted in Figure 4.1. This could give rise to different cross correlation strengths for each signature. The reported 'error' in these values listed in Table 4.1 represents this variability. As can be seen in Table 4.1, speed correlates with nothing and age correlates slightly with crustal thickness and also with angle. However, the most important result here is that angle and crustal thickness correlate very strongly with each other, with an r^2 of 0.45 +/- 0.04. This is a stronger correlation than nearly every correlation we find between a subduction zone property and an element ratio in this study. As such, a correlation with angle may in fact be purely driven by a correlation with crustal thickness and vice versa. When looking at intra-oceanic arcs only, the correlation between crustal thickness and angle is significantly reduced while the correlation between angle and age increases.

4.3.2 Correlations between Crustal Thickness and Element Ratios

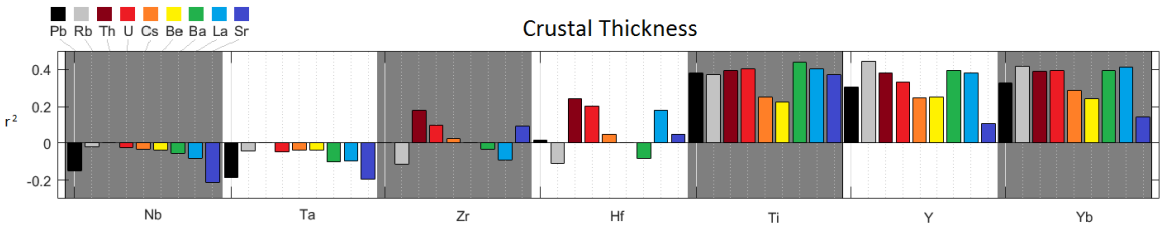

Figure 4.5 The strength of correlation (r^2) of the logarithm of trace element ratios against crustal thickness. The sign of the r^2 value reflects the sense of correlation. Element ratios with the same denominator element are grouped together and numerator elements are given in the top left of each plot. All element ratios with the same numerator element have bars that are coloured the same. So, e.g., a red bar ('U') in the box named 'Nb' refers to the correlation of crustal thickness with the trace element ratio U/Nb.

From this section onwards, as we will often be referring to the behaviour of groups of elements that all behave in the same way, we will use the following notation for brevity: e.g. (Nb,Ta) is Nb and Ta and (U,Th)/(Nb,Ta) refers to the ratios U/Nb, U/Ta, Th/Nb and Th/Ta.

We find some of the strongest correlations with crustal thickness so we present these results first. Figure 4.5 shows the r^2 values of plots of crustal thickness and element ratios. The most immediate observation is the clear correlations of element ratios involving (Ti,Y,Yb) with crustal thickness. On average, element ratios with (Ti,Y,Yb) yield r^2 values of > 0.2 with crustal thickness and some (Ti,Y,Yb) ratios have r^2 values that exceed 0.4, the highest correlations we see in this study. This is particularly strong in Ti. On average, ratios with (Nb,Ta,Zr,Hf) appear to correlate less strongly with crustal thickness: slight negative correlations for ratios with (Nb,Ta) in the denominator and slight positive correlations for ratios with Hf, on average. Consistent trends exist

when looking at the numerator elements. Ratios involving (Th,U) most often appear to correlate the strongest with crustal thickness. Sr/(Nb,Ta) are the two ratios with the strongest anti-correlations with crustal thickness and Sr/(Y,Yb) have very weak correlations with crustal thickness compared to other elements involving Y and Yb. This might indicate that Sr anti-correlates with crustal thickness, although the correlation of Sr/Ti and crustal thickness remains strong.

4.3.3 Correlations between Slab Age, Convergence Rate, Angle, Thermal Parameter and Element Ratios

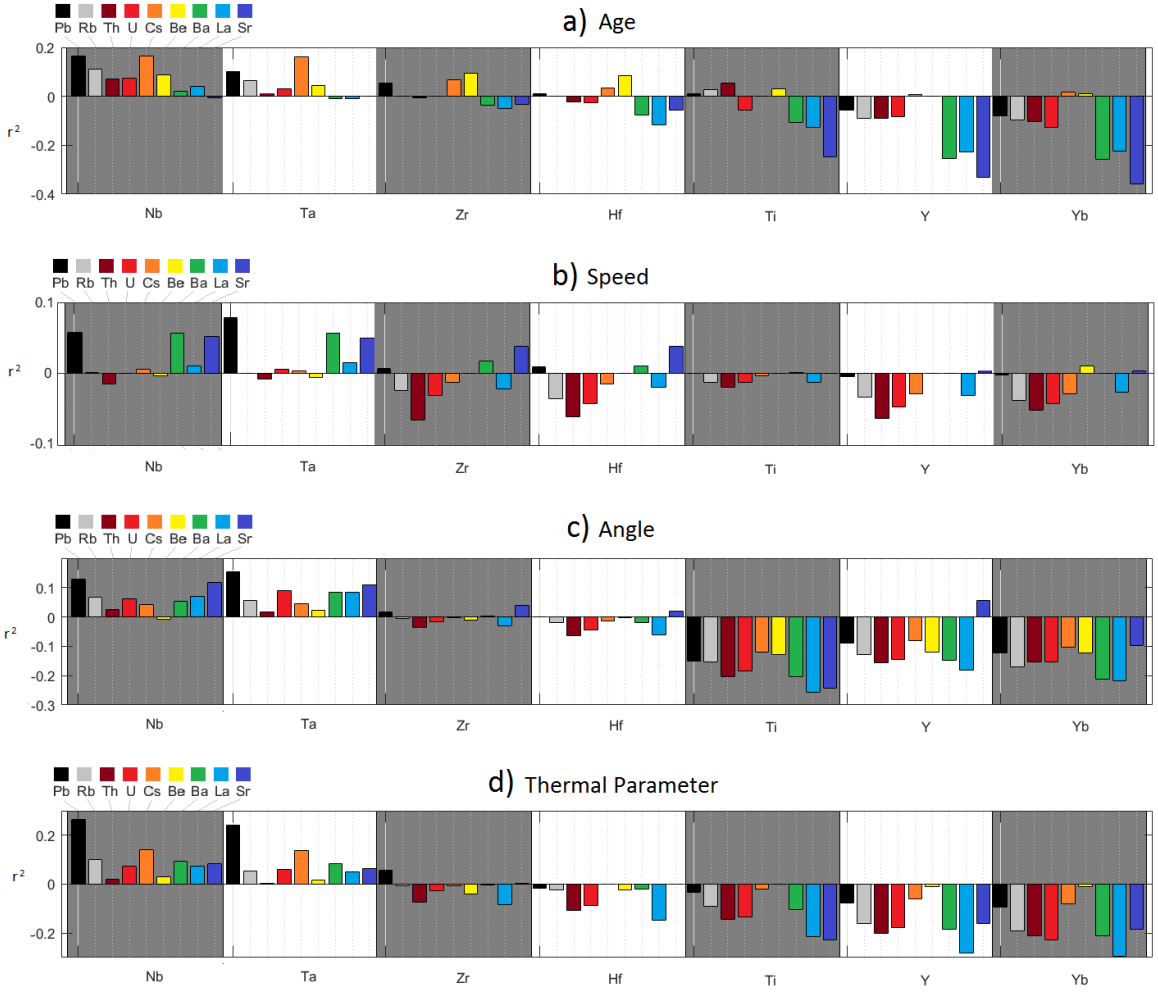

Figure 4.6 The strength of correlation (r^2) of the logarithm of trace element ratios against the logarithm of a) slab age, b) trench normal convergence rate, c) slab dip angle and d) all three combined in the thermal parameter. The sign of the r^2 value reflects the sense of correlation. Element ratios with the same denominator element are grouped together and numerator elements are given in the top left of each plot. All element ratios with the same numerator element have bars that are coloured the same.

As can be seen in Figure 4.6, only slight correlations exist between most of the investigated element ratios and the slab parameters, with only 16 ratios yielding r^2 values with magnitudes greater than 0.2. We previously showed that ratios involving (Ti,Y,Yb) correlate with crustal thickness with $r^2 > 0.2$ on average, but also that crustal thickness correlates with slab age and, in particular, slab angle. It is therefore essential to view these results with the cross correlations between crustal thickness and age and angle in mind. See the Appendix for a full table of results.
Looking at each slab parameter in turn:

Age of the subducted lithosphere (Figure 4.6(a)):
Looking at the behaviour of the denominator elements on average: ratios involving (Y,Yb) anti-correlate strongly with age and those involving Ti anti-correlate weakly with age. These correlations may be elevated slightly by the fact that age anti-correlates with crustal thickness, however if this were the only driver, one would expect Ti to yield the strongest correlation. What we see in (Y,Yb) is therefore likely arising, at least in part, from age itself. Ratios with (Hf,Zr) show no significant correlation when averaged. Ratios involving Nb, and to a lesser extent Ta, on average, slightly correlate with age which, again, may in part be due to the crustal thickness effect. Looking at the consistencies between ratios with the same numerator elements: (Ba,La,Sr)/(Nb,Ta) have the weaker correlations compared to other ratios involving (Nb,Ta) and (Ba,La,Sr)/(Hf,Zr,Ti,Y,Yb) have stronger anti-correlations compared to other ratios involving (Hf,Zr,Ti,Y,Yb), indicating that these three elements all anti-correlate with age. This results in Sr/(Y,Yb) having the strongest correlations with age, with $r^2 > 0.3$, the strongest correlations between an element ratio and any slab property. (Cs,Be) demonstrate the opposite: with the strongest correlations (or weakest anti-correlations), indicating that these two elements perhaps slightly correlate with age. Pb/(Nb,Ta) also appears to positively correlate with age.

Subduction speed (Figure 4.6(b)):
The first thing to note is that all correlations with subduction speed are very weak ($r^2 < 0.1$) so one should be careful drawing conclusions from these data. However, the behaviours of some numerator elements do show consistencies. Firstly, ratios involving Th (and to a lesser extent, U) consistently demonstrate the strongest anti-correlations with speed. Pb, Ba and Sr seem to correlate positively with speed.

Subduction angle (Figure 4.6(c)):
When looking at correlation with angle, the behaviour of ratios involving the denominator elements (Ti,Y,Yb) almost exactly mirrors their behaviour when looking at correlation with crustal

thickness. The only difference is that the correlation is uniformly lower in strength and opposite in sense (compare with Figure 4.5). This is exactly what one would expect if what we observe here is purely due to the cross correlation between angle and crustal thickness. This is the same for (Nb,Ta), except for the fact that the strengths of correlation between ratios involving (Nb,Ta) and crustal thickness and between ratios involving (Nb,Ta) and angle are very similar. As such, it is difficult to say whether it is slab angle driving the correlation or crustal thickness. Among the numerator elements, ratios involving Pb yield the strongest correlations (Pb/(Nb,Ta)) and weaker anti-correlations than most, while (Ba,La) behave oppositely: with the strongest anti-correlations and weakest correlations.

Thermal parameter (Figure 4.6(d)):

Looking at ratios with denominator elements in common, ratios involving (Nb,Ta) correlate the strongest, ratios involving (Ti,Y,Yb) anti-correlate the strongest, and ratios involving (Hf,Zr) mostly have weak anti-correlations. This is similar to what we see with age and angle. A pair of ratios which now stand out are Pb/(Nb,Ta) which have strong positive correlations with the thermal parameter. In addition, Pb/(Ti,Y,Yb) have weaker anti-correlations than most other ratios involving (Ti,Y,Yb) which indicates that Pb correlates positively with the thermal parameter.

4.3.4 Adjusted Chemical Parameter (ACP) Study

The cubes in Figure 4.7 are graphical representations of the a-b-c (age-speed-angle respectively) search space (see Eq. 4-4; Section 4.2.3). The left face is $a = 1$; $-1 < b < 1$; $-1 < c < 1$; right face is $b = 1$; $-1 < c < 1$; $-1 < a < 1$ and top face is $c = 1$; $-1 < a < 1$; $-1 < b < 1$. This is shown pictorially in the key. Redder colours represent values for a, b and c which yield higher r^2 values in log-log plots of ACP versus the ratio of the element given on the left hand side of each row over the element given at the top of each column. An intuitive way to interpret these plots is: if the centre of the bullseye pattern is on the left face, the element ratio (ER) appears to have the strongest dependence on age, then right face; speed, and top face; angle. There will always be two identical bullseyes on each cube, on opposite sides, due to the fact that the strength of correlation is independent of the sense of correlation. ERs that don't yield statistically significant results ($p < 0.05$) are coloured in greyscale. How much the pattern is "smeared" gives an indication on the uncertainty. Figure 4.8 is an array of log-log plots of ER vs the ACP for that particular ratio, laid out in the same way as Figure 4.7.

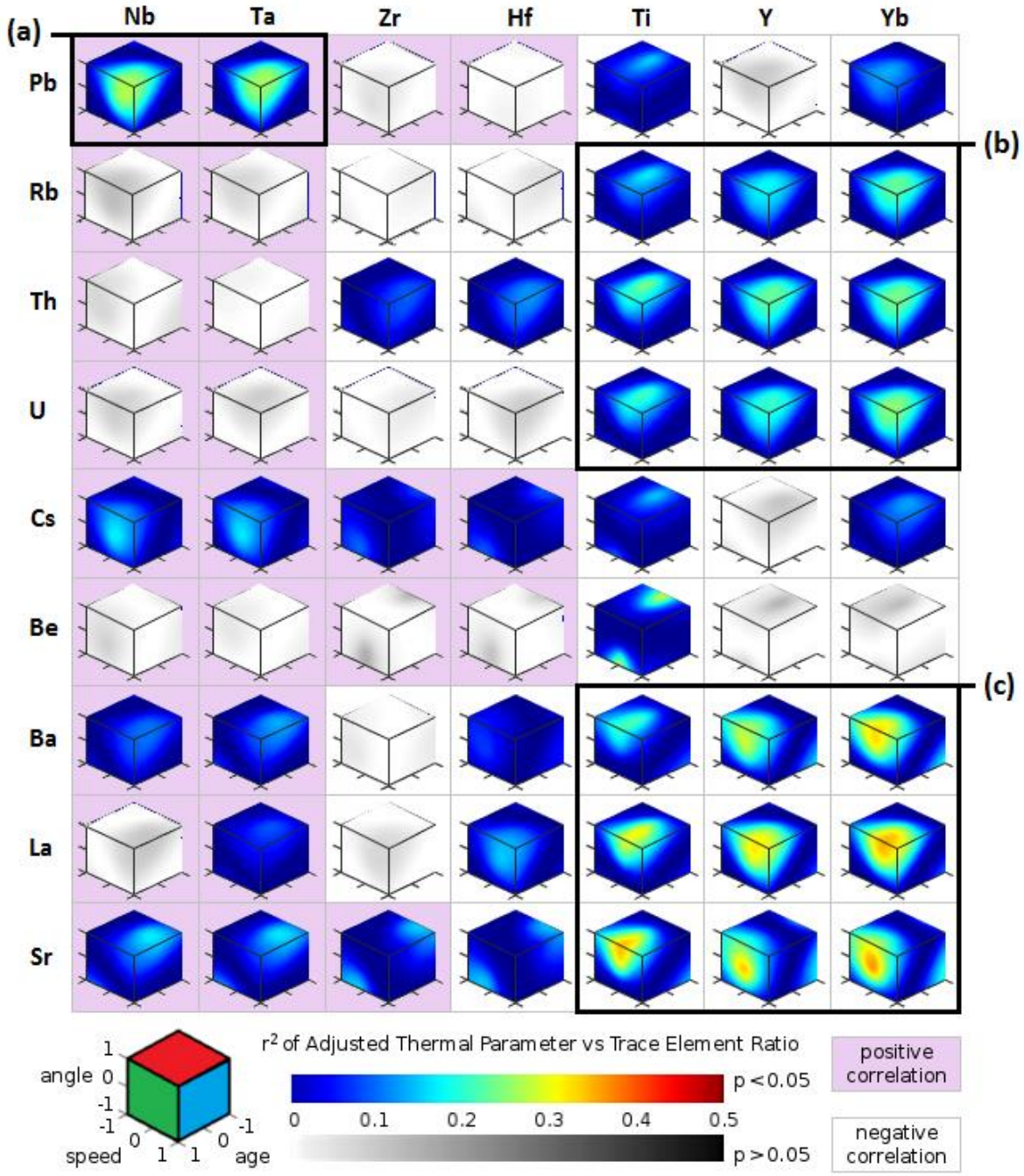

Figure 4.7 The strength of correlation between log(ER) and log(ACP) as a (age), b (speed) and c (angle) are varied between -1 and 1. The element ratio (ER) for each cube is the element of its row divided by the element of its column. On the left face of the cubes, a (age) =1, on the right face b (speed) =1 and on the top face c (angle) =1. Redder colours mean that an ATP, calculated using these values of a, b and c, correlates more strongly with ER. A lilac/white background means that the sense of correlation of the optimal ATP, and ER, is positive/negative. Greyscale cubes indicate that the result for this particular ER is statistically insignificant (p>0.05).

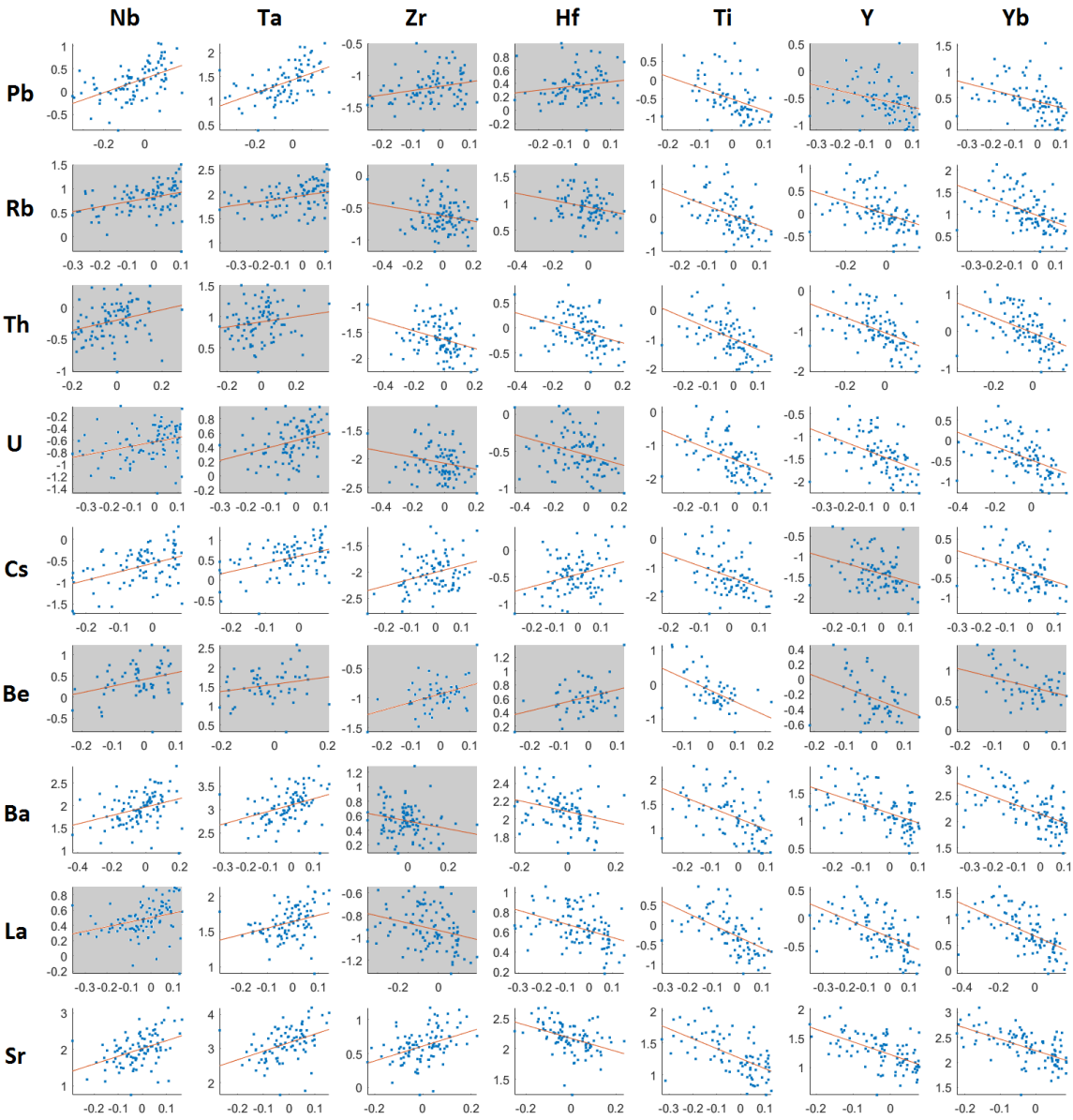

Figure 4.8 Plots of log(ER) (vertical axis) vs log(optimal ATP) (horizontal axis). Linear least squares regression is used to produce the lines of best fit and also the r^2 values quoted throughout this study. Plots with a darkened background represent statistically insignificant ER-ATP plots with p-values > 0.05.

Firstly we highlight some of the overall trends in these data. Certain denominator elements appear to behave near identically: (Nb,Ta), (Zr,Hf), and (Y,Yb) (comparing columns in Figure 4.7). This similarity between these particular pairs of denominator elements is expected due to their chemical similarity (the elements in each of the pairs are largely interchangeable in mineral lattices) giving us confidence in our approach and leading us to believe that what we are seeing here are genuine patterns in the geochemistry. There is a striking difference in the behaviour of ratios that involve (Nb,Ta), compared to ratios that involve any of the other denominator elements: ratios involving (Nb,Ta) correlate positively with their best fit ACPs, while the others correlate negatively (except for a few examples where the best fit ACP, i.e. the centre of the

bullseye pattern, is close to the edge of the cube and so whether or not ER-ACP correlation is positive or negative is ambiguous). Similar groupings of numerator elements can be made: (Rb,Th,U) for example, as well (Ba,La).

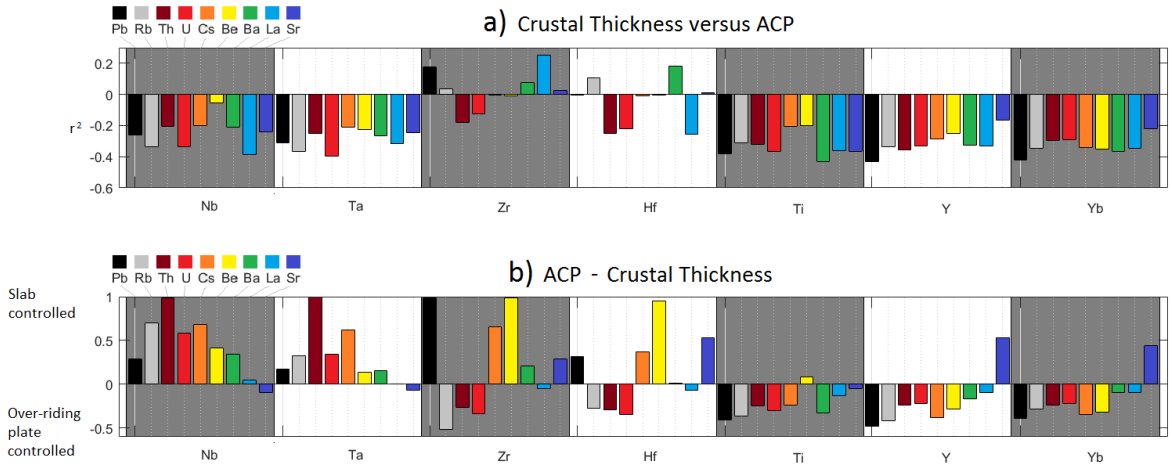

Figure 4.9 a) The strength of correlation (r^2) between the logarithm of ACP calculated for each element ratio and crustal thickness. The sign of the r^2 value reflects the sense of correlation. b) The value of ACP-Crustal Thickness for each element ratio. A description of how this is calculated is given in the main text. Element ratios with the same denominator element are grouped together and numerator elements are given in the top left of each plot. All element ratios with the same numerator element have bars that are coloured the same.

Of all the numerator elements, Pb yields the strongest correlations when put over (Nb,Ta) with the best fit values of a, b and c lying close to 1, 1, 1, similar to the classic definition of the thermal parameter (Figure 4.7, box (a)), and agreeing with what we noted in the previous section. Of the remaining ratios involving (Nb,Ta), Cs/(Nb,Ta) has the next strongest correlation with its ACP, which is dominated by slab age, though the strength of correlation is still < 0.2. (Rb,Th,U)/(Y,Yb) also yield high r^2 values with an ACP which has a, b and c lying close to 1, 1, 1, but this time with an opposite sense of correlation (Figure 4.7, box (b)). (Rb,Th,U)/Ti also yield high r^2 but their optimal ACPs are more angle dominated, indicating that, of all the denominator elements, Ti has the strongest correlation with angle (Figure 4.7, box (b)). (La,Ba)/(Y,Yb) have ACPs which depend on age and angle, but not speed, and (La,Ba)/Ti behave similarly but, again, correlate more strongly with angle (Figure 4.7, box (c)). Sr/(Y,Yb) yield some of the strongest correlations with an ACP. This ACP is approximately dependent on age alone, reinforcing the observation that Sr/(Y,Yb) are apparently controlled by slab age. Sr/Ti is similar, but, as with all other ratios involving Ti, it is deflected to a larger angle dependence (Figure 4.7, box (c)). All element ratios versus ACP plots (Figure 4.8) demonstrate that, while the correlations may be very weak, in some cases < 0.1, so

long as $p < 0.05$, these correlations haven't arisen due to outliers and reveal a genuine trend in the data (albeit a noisy one).

As was demonstrated in the results Section 4.3.1, weak cross correlations exist between the logarithm of the slab age and crustal thickness and strong cross correlations exist between the logarithm of the angle and crustal thickness. Therefore, before we discuss the ACP study results, it is important to compare them with the crustal thickness study. In Figure 4.9, we present the results of this comparison in the same way as results were presented in Figure 4.4 and Figure 4.5. The "Crustal Thickness vs ACP" is the strength of correlation between the ACP and crustal thickness. "ACP-Crustal Thickness" is a crude indication of what might be driving the correlation. This quantity is calculated by subtracting the r^2 of crustal thickness vs ER from the r^2 of ACP vs ER and dividing by their sum. A negative value indicates that crustal thickness is more likely the driver, as it correlates more strongly with the crustal thickness signature than the ACP one, and positive value: vice versa. For all denominator elements, except for (Zr,Hf), crustal thickness and ATP correlate reasonably strongly with each other. However, we see from ACP-Crustal Thickness that this may be for different reasons. Since the ACP-Crustal Thickness values of (Ti,Y,Yb) are mostly negative, these elements correlate more strongly with crustal thickness, indicating, as we alluded to in Section 4.3.2, that their concentrations are dominated by a crustal thickness related effect. (Nb,Ta) concentrations correlate significantly more strongly with ACP (positive ACP-Crustal Thickness values) and therefore are perhaps more slab controlled.

4.3.5 Intra-Oceanic Subduction Only

As highlighted in Figure 4.1, by excluding all continental subduction segments, the size of the dataset is reduced considerably. As a consequence, when running the same ACP analysis, the majority of signatures yield results that are not statistically significant: there are simply not enough data to see above the noise in the data. For the most part, it is the element ratios that yielded the higher r^2 values when looking at the unfiltered data that retain their statistical significance. These sets (boxes (a), (b) and (c) in Figure 4.7), along with (La,Sr)/(Zr,Hf), are presented in Figure 4.10, in the same format as in Figure 4.7. In all cases, the strong dependence of ratios involving Ti with its ACP, which was primarily angle controlled, has disappeared (Figure 4.10, panels (a) and (b)), lending further support to the hypothesis that Ti is primarily, if not completely, over-ridingly plate controlled. The angle dependence of ratios with (Y,Yb) in the denominator has also been reduced to near zero (Figure 4.10, panels (a) and (b)), though many of these ratios still have strong correlations with their ACPs, only now their ACPs are all primarily age controlled. The strength of correlation of Pb/(Nb,Ta) with its ACP has been dramatically reduced

such that now p > 0.05 (Figure 4.10, panel (c)). The strength of correlation of (La,Sr)/(Zr,Hf) has increased significantly upon applying this intra-oceanic filter (Figure 4.10, panel (d)). Its ACP is primarily age and angle determined (but with age in a positive sense and angle in a negative sense).

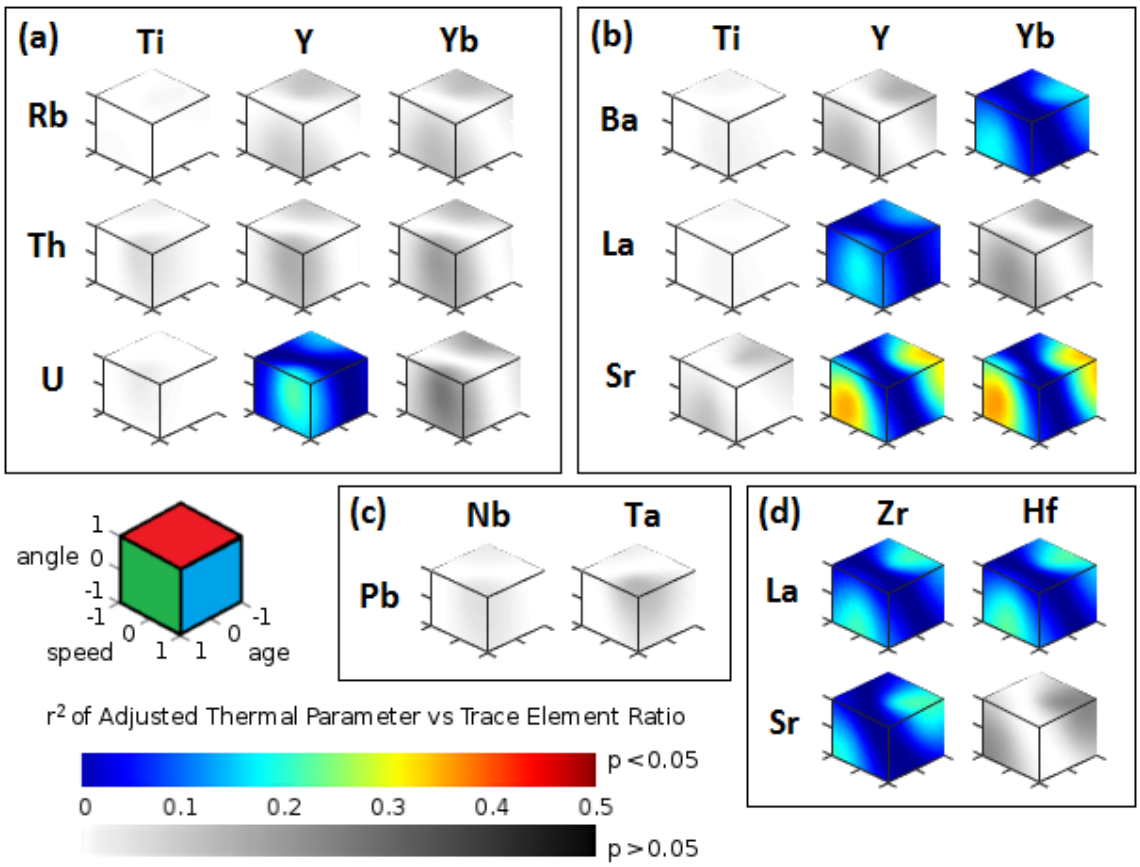

Figure 4.10 Results of the ACP study performed using only subduction segments that are intra-oceanic, presented in the same way as the results in Figure 4.7.

4.3.6 Correlations with Silica Content and Magnesium Number

The silica content and magnesium number, as mentioned previously, are rough proxies for the amount of fractional crystallisation a lava has undergone. Fractionation increases the silica content and decreases the magnesium content such that more highly fractionated lava (more evolved) has high silica and low magnesium. Fractionation is known to alter the trace element characteristics of erupted lavas; for some elements more than others. To gauge how much a trace element is susceptible we look for correlations between each ratio and the average silica content and magnesium number of each subduction segment. The majority of the element ratios we look at correlate positively with silica (Figure 4.11a) and negatively with magnesium number (Figure

4.11b). This could either be because fractionation is leaching denominator elements from the lava or concentrating numerator elements. Of all the denominator elements, this is strongest in ratios involving Ti. Ratios involving Nb show the strongest anti-correlation with Mg# and weak correlation with silica content (along with ratios involving Ta). Ratios involving (Y,Yb) correlate with silica content but have no correlation with Mg# (except for the exceptional Sr/(Y,Yb) which correlate positively and strongly with Mg#, see below). Looking at ratios with a common numerator element: ratios involving Be correlate the strongest with silica and anti-correlate the strongest with Mg#, whereas this trend is notably weaker in Ba and La. However, the most striking behaviour comes from Sr. Ratios involving Sr behave in a completely opposite way: positively correlating very strongly with Mg# and anti-correlating with silica content.

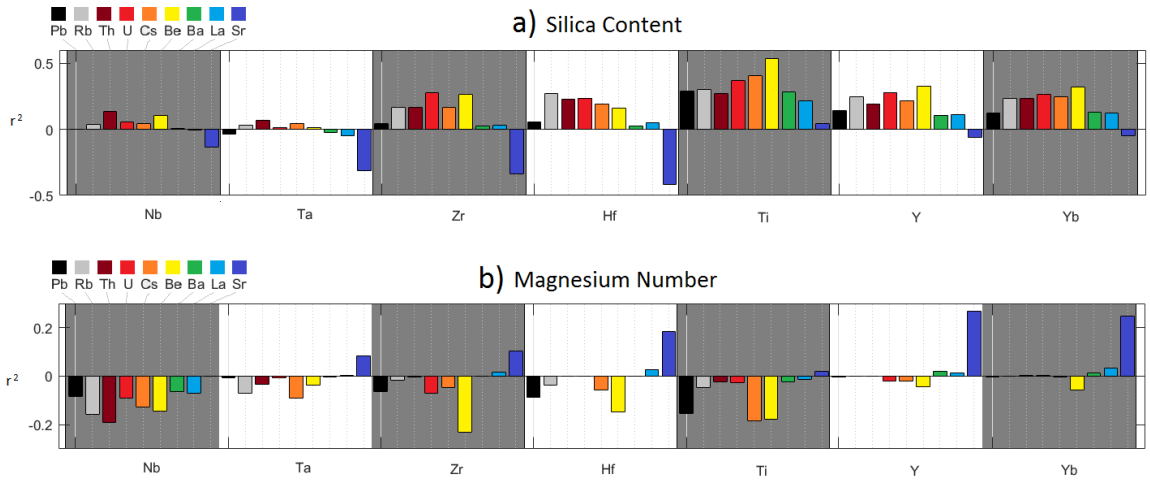

Figure 4.11 The strength of correlation (r^2) of the logarithm of trace element ratios against the average silica content and magnesium number (see Equation 4.1) of lavas in each subduction segment. The sign of the r^2 value reflects the sense of correlation. Element ratios with the same denominator element are grouped together and numerator elements are given in the top left of each plot. All element ratios with the same numerator element have bars that are coloured the same.

4.3.7 Primitive Lavas Only

Given that we observe that many of our element ratios are affected by fractionation processes, we attempt to, at least partially, remove the effect of fractionation by performing the ACP study using data that have first been filtered for low silica, high Mg# and also high Ni content. We ran the analysis for two levels of filter: an intermediate filter with lavas that have Mg# > 0.55, SiO_2 < 0.6 wt % and Ni > 30 ppm and a mafic filter with lavas that have Mg# > 0.6, SiO_2 < 0.55 wt% and Ni > 40 ppm. The results of the run with the intermediate filter are presented in Figure 4.12 and Figure 4.13, in the same way as the unfiltered data (see Section 4.3.4). Unfortunately, when running the mafic filter, not enough segments remained for all but three element ratios to have p

< 0.05. Given we investigate the behaviour of 63 element ratios and given that we set our confidence limit to 95% (p=0.05), we would expect approximately 3 (~0.05 x 63) to yield p > 0.05, if all the data were random. As such, these results were not analysed further.

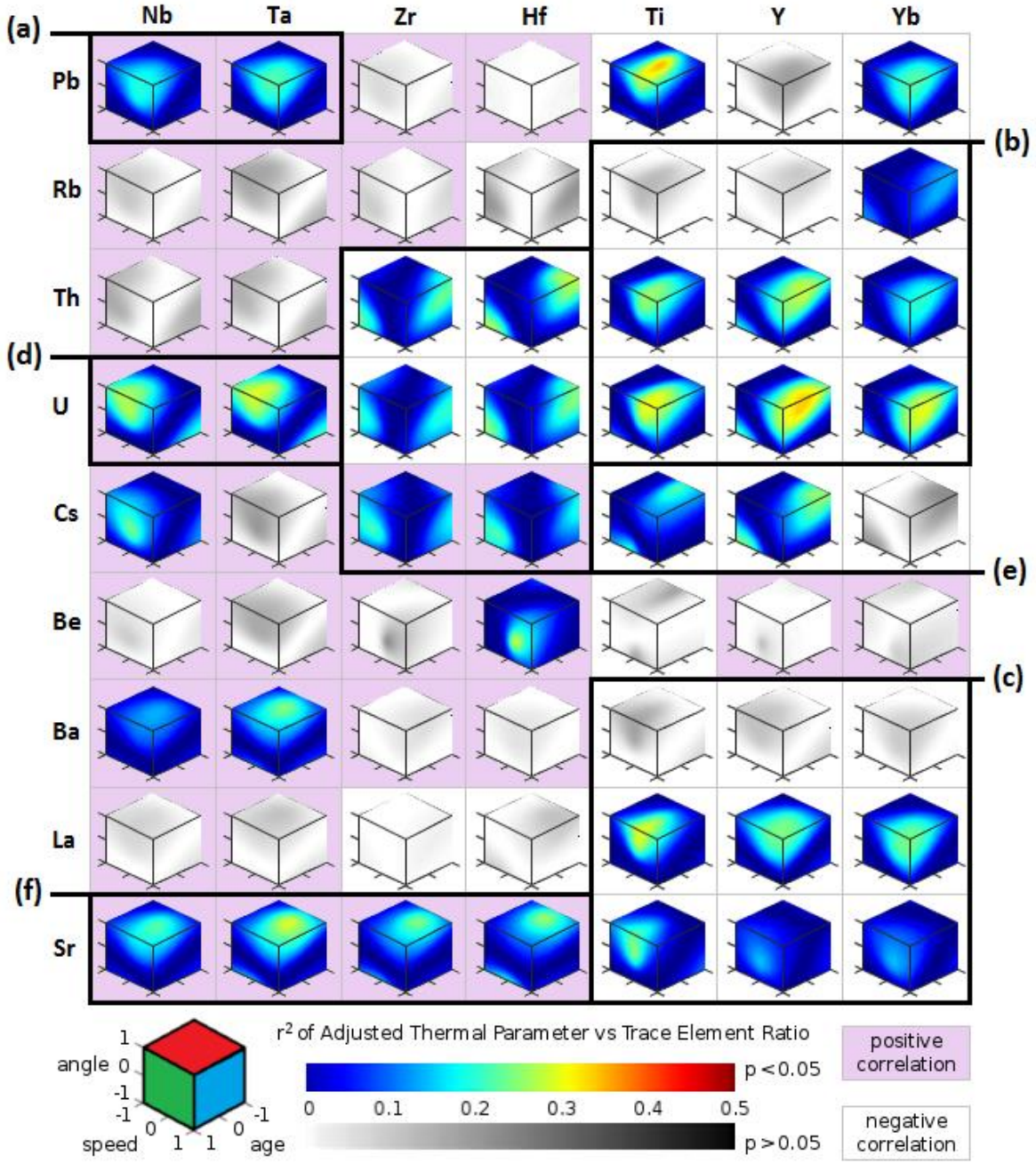

Figure 4.12 Similar plots to those in Figure 4.7 (see figure caption for details) except for the data filtered with the intermediate lava filter (Mg# > 0.6, SiO2 < 0.55 wt% and Ni > 40 ppm).

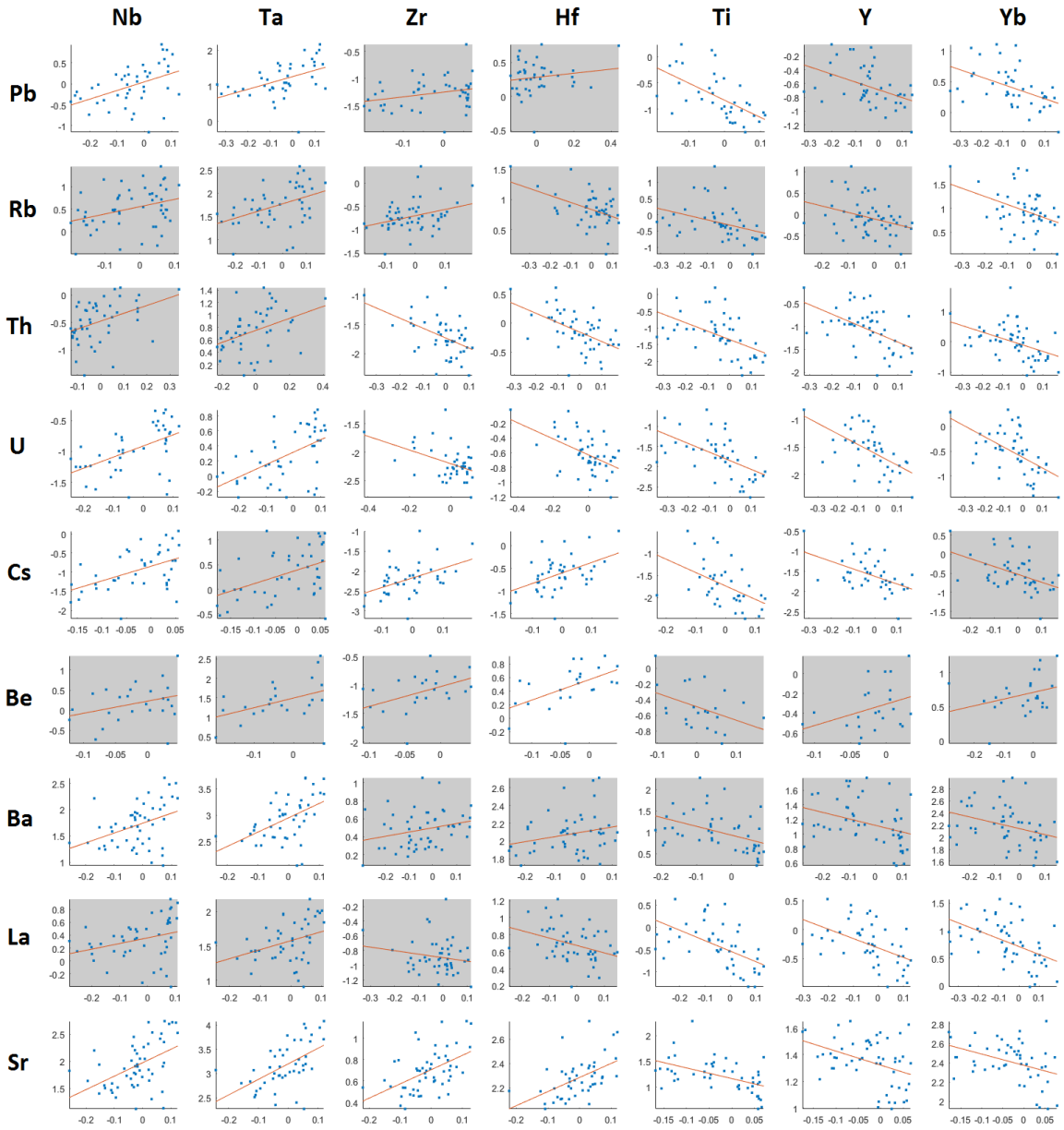

Figure 4.13 Plots of log(ER) (vertical axis) vs log(optimal ATP) (horizontal axis). See the caption of Figure 4.8 for more details.

We analysed the results gained from using the intermediate filter with respect to the results gained using unfiltered data (presented in Section 4.3.4). As with the unfiltered data, ratios with (Nb,Ta) demonstrate positive correlations and the rest negative. This is except for the cases where the determined ACP, i.e. the centre of the bullseye pattern, is close to the edge of the a-b-c (age-speed-angle respectively) search space (meaning the sense of correlation with ACP is ambiguous), and also in the case of Sr, which is discussed in more detail below. Applying the intermediate filter has done little to affect the behaviour of Pb/(Nb,Ta) (Figure 4.12 box (a)), although the strength of correlation of Cs/Nb and its ACP has increased. In the set within Figure 4.12 box (b), the statistical

significance of the correlations between ACP and element ratios with Rb has been reduced to the point of p>0.05 for all but Rb/Yb. The angle dependence of the ACPs for the remaining elements in this group has been reduced: the ACP for (Th,U)/Ti now depends more heavily on age and the ACP for (Th,U)/(Y,Yb) depends more heavily on speed. Looking at the set within Figure 4.12 box (c): while the dependence of the ACPs on age, speed and angle have remained approximately the same, the strength of correlation between ACP and element ratios has been reduced in all cases; to the point of being statistically insignificant in the case of Ba. The most dramatic decrease is seen in Sr/(Y,Yb). The strength of correlation between U/(Nb,Ta) and its ACP, which depends on both age and angle, has increased significantly (Figure 4.12 box (e)). The strength of correlation between (Th,U,Cs)/(Zr/Hf) and their ACPs, which depend on age, speed and angle (but with age in the opposite sense) has also increased. Cs/(Ti,Y,Yb) appears to now behave in a similar way to this set. Sr/(Nb,Ta,Zr,Hf) (as well as Ba/(Nb,Ta)) now appears to correlate positively and strongly with an ACP which is determined solely by angle.

4.4 Discussion

4.4.1 Evidence of the Reliability of the Analysis Tool

The primary goal of this work was to set up a tool to look for correlations between the geochemical characteristics of arc lavas and the physical subduction zone properties: slab age, convergence rate, slab dip and over-riding crustal thickness. A number of aspects of the data we have acquired by running the tool for 63 different trace element ratios indicate that we have achieved our goal in creating a tool that is reliably revealing real trends in the raw data. One key indicator is the similarity in behaviour of elements that one should expect to behave similarly. Y and Yb are both heavy rare earth elements and behave near to identically even after geochemical filtering and even when using intra-oceanic subduction zones only. Nb and Ta also behave identically and Hf and Zr behave very similarly. There are also some correlations we observe that mirror what has previously been suggested by other studies of both global and regional data. For example, we find anti-correlation between heavy rare earth elements and crustal thickness and anti-correlation between Sr/Y and slab age. Both of these are discussed more fully below.

4.4.2 Crustal Thickness and Fractionation

One of the most striking results to come out of this investigation is the strong positive correlations of nearly all element ratios involving (Ti,Y,Yb) with crustal thickness (Figure 4.5). This is then mirrored in the correlations of these ratios with angle, and to lesser extent age, as crustal thickness anti-correlates with both (more strongly with angle). To gauge whether this is a cause or an effect, we calculated an "ACP-Crustal Thickness" value which indicates that this is indeed being driven by a correlation with crustal thickness and not by the slab parameters (Figure 4.9b). As this is a consistency across denominator elements, this indicates that the process responsible for this observation removes Y, Yb and Ti and occurs more readily or to a greater extent where crust is thicker (or in continental arcs more than in intra-oceanic arcs). Further indication that this is the case comes from the fact that the angle dependence (which arises due to cross correlation with crustal thickness, Figure 4.7, box(b)) of the optimal ACPs of (Ba,La,Sr)/(Ti,Y,Yb) disappears when looking at intra-oceanic arcs only (Figure 4.10, box(b), although this could also be due to the fact that angle correlates less with crustal thickness when looking at this dataset). We also observe that, on average, element ratios involving Ti (followed by (Y,Yb)) correlate the strongest with SiO_2, an indicator of how much fractional crystallisation a lava has undergone. As such, it seems likely that this process is fractional crystallisation.

We aren't the first to observe correlations between depletion of HREEs and crustal thickness (Chiaradia, 2015; Mantle and Collins, 2008; Profeta et al., 2015). The fact that we also see correlation between the depletion of Y and Yb and crustal thickness therefore gives us more confidence that this tool is working correctly. It is believed that garnet (and to a lesser extent amphibole) is responsible for depleting Y and Yb as it has the capacity to incorporate heavy rare earth elements into its mineral lattice, leaching them from the lava. However, the exact mechanism responsible is hotly debated. Garnet is a high pressure phase; stable at >40 km depth, and as such, reduced HREE could arise through melting of a basaltic source at depth, either the slab (Defant and Drummond, 1990) or lower arc crust (Atherton and Petford, 1993), or via deep fractionation of a mantle derived lava at depth (Macpherson et al., 2006). Deep fractionation and re-melting of the base of arc crust are both likely to be enhanced if the over-riding crust is thicker. Anti-correlation of Y and Yb with crustal thickness therefore supports either of these hypotheses. However, the strong anti-correlation of Y and Yb with SiO_2 may point more towards the fractionation hypothesis. In addition, it could be argued that slab melting should be more likely if the crust is thinner as this could indicate that the whole over-riding lithosphere is thinner and the decoupling depth possibly shallower. As we demonstrated in the previous chapter, this would increase slab top temperatures at a given depth. As such this correlation is maybe also evidence

against a slab controlled origin for lowered Y and Yb. An important exception to all of this is Sr/(Y,Yb), which may have a slab origin after all, discussed further in Section 4.4.4.

For Ti, the anti-correlation with crustal thickness and the correlation with SiO_2 are even stronger in our data. The reduction of the correlation with angle upon removing the most evolved lavas is also more extreme. This would point to a similar fractionation based mechanism that removes Ti, which is even more prevalent. However, such correlations are far less reported in the literature, if not absent. This is not to say that this behaviour is unexpected. Potential mineral phases which can remove Ti during fractional crystallisation are metal oxides (primarily magnetite) (Verhoogen, 1962). It has been experimentally observed that Ti depletion occurs in the final stages of fractionation (Villiger et al., 2006). Perhaps what we observe in Ti therefore results from these aspects of the fractionation process, although further research into this is needed to further understand these results.

4.4.3 Sediment Melting: Elevated Thorium

It is commonly proposed that the Be and Th found in arc lavas is a result of sediment melting (Johnson and Plank, 2000). This is because the main source for Be and Th into the subduction system are the sediments, rather than the mafic crust or hydrated slab mantle, and because neither Be or Th are fluid mobile. Unfortunately, the level of noise in ratios involving Be means that Be ratios show no significant or consistent correlations with any subduction zone property and p values are consistently low. However, ratios involving Th demonstrate clearer correlations. When the data are unfiltered, Th/(Ti,Y,Yb) correlate strongly with an ACP that is controlled primarily by angle, speed and age (all in a negative sense: i.e. lower angle, speed or age implies higher Th/(Ti,Y,Yb)) (Figure 4.7, box (b)). The strong angle and age dependence is something we see in the optimal ACPs of other ratios involving (Ti,Y,Yb), such as (Ba,La,Sr)/(Ti,Y,Yb) that, as discussed in Section 4.4.1, likely arises (at least in part) due to fractionation processes. However, Th/(Ti,Y,Yb) has an additional dependence on subduction speed. Crucially, the optimal ACP for Th/(Ti,Y,Yb) actually shifts away from angle, and towards a convergence rate dependence, when the most felsic lavas are excluded. This perhaps indicates that, in the more primitive lavas, Th/(Ti,Y,Yb) correlates more strongly with convergence rate and that this isn't a product of fractionation. Another effect of applying this intermediate lava filter is to increase the strength of correlation of Th/(Zr,Hf) with its optimal ACP, which is also dependent strongly on convergence rate, in the same negative sense as the ACP for Th/(Ti,Y,Yb) (though now with an equally strong dependence on slab age in a positive sense, an observation we can't explain here). Unfortunately, not enough data remain to draw conclusions from the data where only intra-oceanic arcs are

used. The final piece of evidence that convergence rate is playing a consistent role across all ratios involving Th is the fact that, when looking at ratios correlating with convergence rate alone (see Section 4.3.3), we find that ratios involving Th have consistently stronger anti-correlations with speed or weaker positive correlations than other ratios.

This correlation with convergence rate is negative: slower slabs have higher Th. In the previous chapter we concluded that slab crust temperatures, at sub-arc depths, were dominated by convergence rate: slower slabs have a hotter slab crust with age playing a secondary role, particularly deeper, and angle virtually none. We would therefore expect sediment melting to be controlled by convergence rate above all else. This is particularly if, as Behn et al. (2011) suggest, the formation of mantle wedge diapirs are necessary, as these are promoted twofold by slower slab speeds: hotter crust is weaker and forms Rayleigh-Taylor instabilities more readily, and slower slabs give the instabilities more time to form (Maunder et al., 2016). As such, the fact that we see a negative correlation between Th concentration and convergence, which strengthens as more evolved lavas are removed from the dataset, is maybe a hint that Th is indeed added by a slab-melt component.

However, another feature of our analysed results is that U behaves nearly identically to Th: all of what we describe above for Th applies equally as well to U. The source of U is thought to be identical to Be and Th, which is the subducted sediments. However, it is believed that U is fluid mobile (Bailey and Ragnarsdottir, 1994). This is perhaps then indicative that fluid release from the sediments is also thermally controlled: slower slabs release more sediment fluids beneath arcs. Another explanation for the similarity between U and Th is that perhaps sediment melting isn't actually required to release Th from the slab at all. It has indeed been suggested that supercritical fluids are able to transport both Th and U from sediments to the mantle wedge together (Kessel et al., 2005). However, this does then leave us with the question: why don't other fluid mobile elements that are carried primarily in the sediments also behave identically to Th and U?

4.4.4 The Adakitic Signature

The most important feature of a so called "adakite" is elevated Sr/Y and La/Yb (Kay, 1978). Early work recognised that this signature tended to arise where the subduction of young slabs is occurring or has occurred (Defant and Drummond, 1990). Our results mirror this finding: the Sr/Y-age anti-correlation is the strongest correlation between any element ratio and slab parameter, and La/Yb also strongly anti-correlates with slab age. However, the cause of this correlation is unclear from our results.

As we discussed in Section 4.4.2, the strong correlation between the concentrations of (Y,Yb) and slab dip likely arises from the fact that (Y,Yb) concentration anti-correlates with crustal thickness and crustal thickness anti-correlates with slab dip. This could also be true for the correlation between (Y,Yb) concentration and slab age as slab age also anti-correlates with crustal thickness. However, this anti-correlation between crustal thickness and slab age is weaker and so the fact that Sr/Y, in particular, correlates with slab age and not with angle at all suggests that this isn't purely crustal thickness controlled.

In addition, we concluded in Section 4.4.2 that the anti-correlation between (Y,Yb) concentration and crustal thickness was likely linked to fractionation as we saw that element ratios with (Y,Yb) in the denominator also generally correlate with silica content. The exception to this is Sr/(Y,Yb) which slightly anti-correlates with SiO_2 (as opposed to positively correlating with SiO_2 like the other ratios involving (Y,Yb)) and also correlates strongly with Mg#, suggesting that it behaves in an opposite way to the other element ratios involving (Y,Yb) upon fractionation. This could potentially indicate that a fractionation process exists which strongly sequesters Sr. Such a process does indeed exist and the mineral phase responsible for Sr fractionation is generally thought to be primarily plagioclase. This might explain the Sr behaviour when looking at correlations with SiO_2 and Mg#. However, this fractionation process is highly pressure dependent: Sr will be incorporated into plagioclase buy only <~30 km (Profeta et al., 2015). As such, one might think that it would serve to enhance the correlation of Sr/(Y,Yb) with crustal thickness, not reduce it in comparison to other element ratios involving (Y,Yb).

So what about a slab control for the adakitic signature, potentially slab melting, which over-prints or even over-writes any crustal effects? Arguments for this, given our results, also seem weak. Firstly, from our results in Chapter 3, we would actually expect slab crust temperatures to be primarily controlled by subduction speed with a secondary control from slab age. This is bolstered by what we observe in the "sediment melt" signature (Section 4.4.3). We don't see any correlation between the adakitic signatures and subduction speed. Secondly, when the intermediate lava filter is applied, the strength of correlation between this La/Yb, and in particular Sr/(Y,Yb), and their ACPs, is reduced (compare Figure 4.7, box (c) and Figure 4.12, box (c)). This would point to fractionation being the driver despite what we discussed in the paragraph above. Taken together, our results appear conflicting with regards to the origin of the adakitic signature. However, the further investigation discussed in the following section may help provide more insight.

4.4.5 Directions for Further Work

In this chapter, we have applied a moderate filter to remove the most evolved lavas from our data set in Section 4.3.7, which has given us a first indication of whether or not trends that we observe are features of the lava source or a result of fractionation processes. But we believe that we can now do better. A filtered version of the GeoRoc database has been released very recently (at the time of writing) by Schmidt and Jagoutz (2017), and could be used as the input into our analysis tool. This filtering is more rigorous than the simple SiO_2, Mg# and Ni content filter we applied in this study and could potentially enable us to better investigate slab processes without the effects of fractionation complicating the results. Performing this investigation may help us to shed light on the unanswered questions that remain from this study.

4.5 Conclusions

We have developed a tool for quantifying the strength of correlation between trace element ratios of arc lavas and physical properties of subduction zones: slab age, convergence rate, slab dip and over-riding crustal thickness. We tested its operation by using it to look at the behaviour of 63 different element ratios. The most striking findings are a strong correlation between slab dip and the concentrations of titanium, yttrium and ytterbium, and a strong anti-correlation between crustal thickness and the same three elements. Looking at cross correlations, it is apparent that these observations are linked, as crustal thickness and slab dip anti-correlate strongly ($r^2 > 0.4$). This result alone suggests that one generally needs to be careful when looking for correlations between slab parameters and the geochemistry and to always check for such cross correlations.

After analysis, we conclude that this correlation is driven by a dependence on crustal thickness that is likely arising from fractionation processes. A crustal thickness dependence of the concentrations of Y and Yb, in particular, has long been suggested and the fact that we arrive at the same conclusion gives us confidence that our technique works. Other indications that our method works come from the similarity in the behaviour of elements that should behave similarly e.g. Niobium and Tantalum.

For evidence of the influence of any slab processes on the arc lava geochemistry, we look at Thorium, which is commonly thought to be an indicator of sediment melting. Of all the elements we investigate, it does appear to (anti-)correlate more strongly with convergence rate than any other element, something that becomes stronger when the more evolved magmas are filtered out. This matches our finding that slab top temperatures are dominantly controlled by

convergence rate. However, uranium, which is fluid mobile, appears to behave near to identically to thorium. We also analyse the behaviour of the "adakitic" signatures Sr/Y and La/Yb. Both signatures have a strong correlation with slab age, which has previously been suggested as evidence that high Sr/Y and La/Yb are the result of slab melting. However, a couple of observations seem contrary to this idea. Firstly, there is no correlation between Sr/Y or La/Yb and convergence rate as there is for Th (and U), which should be the main control on crustal temperatures given our results in Chapter 3. Secondly, the strength of correlation between Sr/Y or La/Yb and slab age decreases when the most evolved magmas are excluded. As such, it is still unclear whether elevated Sr/Y or La/Yb values are slab-derived. However, a proposed further analysis, using a recently released geochemical dataset that is carefully filtered for primitive melts, may yet yield answers.

5 Relamination of Mafic Subducting Crust Throughout Earth's History

This chapter is based on the published manuscript by Maunder et al. (2016). The numerical experiments and production of the manuscript were done by B. L. Maunder who would like to acknowledge the useful discussions, training and support provided by his co-authors.

5.1 Introduction

The mechanisms that have led to the formation of the felsic continental crust (CC) from the mantle throughout Earth's history are still poorly understood, but the presence of subduction systems seems to be an essential component. Indeed, the composition of today's subduction related magmas share many similarities with the CC (Jagoutz and Kelemen, 2015; Rudnick, 1995). This also applies to the most ancient CC (>2.5Ga), however, there are systematic differences (Taylor and McLennan, 1995). In particular, certain geochemical features common of this early crust are widely recognised to be derived from mafic material at high pressure (Alonso-Perez et al., 2009; Defant and Drummond, 1990; Foley et al., 2002), but the particular processes that operated in the early Earth and led to the specificities of the early CC are still speculative.

A commonly accepted mechanism explaining the structure and composition of the CC is a basalt input model, where mantle derived basaltic arc magmas are differentiated into a felsic component, leaving an ultramafic to mafic cumulative counterpart that ultimately delaminates and is recycled back into the mantle (Rudnick, 1995). However, recent studies have argued for a simpler petrological model where buoyant diapirs of crustal material detach from the slab, pond beneath the over-riding plate and melt, feeding the lower crust with evolved magmas from below, a process commonly referred to as "relamination" (Castro et al., 2013; Hacker et al., 2011; Kelemen and Behn, 2016; Marschall and Schumacher, 2012). Based on the pervasiveness of a sedimentary signature in arc magma it is suggested that ~27% of modern granulite terranes and ~43% of ultra-high-pressure terranes have formed via such a crustal underplating mechanism (Behn et al., 2011). However, when looking at Archean granulites this figure falls to 6% (Hacker et al., 2011) in accordance with the fact that the composition of Archean CC is best explained by the involvement of mafic, not just sedimentary, crustal material.

Secular changes in crustal composition suggest that CC formation differed from the modern day mechanism, but exactly how is debated (Condie, 2005; van Hunen and Moyen, 2012). Whether

subduction even played a role in the Earth's earliest history has been thrown into question (Davies, 1992; Sizova et al., 2010), although there is structural evidence for Archean subduction (Calvert et al., 1995; Stevens and Moyen, 2007). If subduction did occur in the early Earth, conditions within the subduction system are expected to have differed systematically from conditions today. In particular, mantle temperatures were probably higher (Herzberg et al., 2010), and oceanic crust was likely thicker as a result (Abbott et al., 1994; Hoffman and Ranalli, 1988). This oceanic crust may have differed compositionally from today's MORB (Herzberg et al., 2010) and, as such, may have had different physical properties. Moreover, it is debated whether subduction in the Archean was slower (Korenaga, 2006), faster (van Hunen and van den Berg, 2008), or comparable to today (Sleep, 1992) and perhaps occurred at a shallower angle (Abbott et al., 1994) although this point is also debated (van Hunen et al., 2004). All these differences may have affected the dynamics of the subduction interface and, in particular, allowed for the relamination of more of the subducting crust.

This leads to the hypothesis: if relamination of subducted felsic materials occurs in modern subduction zones then perhaps, under different, early Earth conditions, such a process may have been viable not only for subducted sediments, but for more of the mafic part of the subducting crust as well, thus producing the characteristics of Archean CC. In this paper, we aim to constrain the conditions required for the relamination of the mafic subducting crust by using a thermo-mechanical numerical model of subduction, varying key parameters across a range of values deemed reasonable for the modern and Archean Earth. We show that under Archean conditions (i.e., with hotter mantle and thicker mafic crust), relamination of the mafic subducting crust is indeed viable under a wider range of subduction conditions. The observed dynamic behaviour can also account for other characteristics of Archean felsic terranes and related rocks, such as their episodic emplacement history (Moyen and Van Hunen, 2012), variable mantle signature (Smithies, 2000), and variable depth of primary melt formation, as well as the secular change of these properties throughout the Archean (Martin and Moyen, 2003).

5.2 Method

Symbol	Description	Units	(Default) value	Lower bound	Upper bound
t	Time	s	–	–	–
u	Velocity	ms^{-1}	–	–	–

P	Pressure	Pa	–	–	–
T	Temperature	K	–	–	–
C	Composition (mantle, basalt or eclogite)		–	–	–
z	Depth	m	–	–	–
$\dot{\varepsilon}$	Strain rate	s^{-1}	–	–	–
$\mathbf{A_{mantle}}$	Pre-factor for mantle dislocation creep	Pa^n s	5.92×10^{15}	3.61×10^{16}	5.92×10^{15}
$\mathbf{A_{crust}}$	Pre-factor for crustal dislocation creep	Pa^n s	3.37×10^{20}	6.04×10^{21}	1.59×10^{19}
$\mathbf{E_{mantle}}$	Activation energy for mantle dislocation creep	J mol^{-1}	5.41×10^5	4.50×10^5	5.41×10^5
$\mathbf{E_{crust}}$	Activation energy for crustal dislocation creep	J mol^{-1}	2.44×10^5	1.70×10^5	3.23×10^5
$\mathbf{n_{mantle}}$	Stress exponent for mantle dislocation creep		3.48	3.47	3.48
$\mathbf{n_{crust}}$	Stress exponent for crustal dislocation creep		3.03	2.95	3.12
R	Gas constant	J K^{-1} mol^{-1}	8.31	–	–
$\mathbf{T_0}$	Surface temperature	°C	0	–	–
ΔT	Temperature of mantle relative to T_0 (modern/Archean)	°C	1350 / 1550	1350 / 1450	1550 / 1650
ρ	Density of the mantle	kg m^{-3}	3300	–	–
$\mathbf{\Delta\rho_{crust}}$	Density of oceanic crust relative to the mantle	kg m^{-3}	−300	−500	−100
$\mathbf{\Delta\rho_{eclogite}}$	Density of eclogite relative to the mantle	kg m^{-3}	+200	–	–
$\mathbf{d_{crust}}$	Incoming crustal thickness	km	7 / 15	7 / 15	22 / 29
$\mathbf{d_{plate}}$	Thickness of the over-riding plate	km	50	20	80
$\mathbf{d_{eclogite}}$	Depth of transition from crust to eclogite	km	140	80	140
$\mathbf{d_{weak\ zone}}$	Depth the weak zone extends to	km	d_{plate} + 10	–	–
r	Initial radius of curvature of slab	km	180	–	–

x_0	Distance from left boundary to trench	km	18	–	–
θ	Subduction angle	°	45	30	60
v_{plate}	Velocity of the subducting plate	cm yr^{-1}	5 OR 4.5	2	10
Slab age	Age of the subducting plate	Myrs	40	20	60
η_0	Reference viscosity	Pa s	10^{19}	–	–
$\eta_{weak\ zone}$	Viscosity of weak zone	Pa s	10^{20}	10^{19}	10^{21}
η_{max}	Maximum viscosity	Pa s	10^{24}	–	–
h	Model depth	km	150	–	–
κ	Thermal diffusivity	$m^2\ s^{-1}$	8×10^{-7}	–	–
g	Acceleration due to gravity	ms^{-2}	9.8	–	–
α	Thermal expansivity	K^{-1}	3.5×10^{-5}	–	–

Table 5.1 A list of the parameters that define the model. The default values of all the parameters are given as well as the upper and lower bounds for the parameters varied in the parametric study.

5.2.1 Model Physics

A 2-D Cartesian version of the finite element code Citcom is used (Moresi and Gurnis, 1996; Zhong et al., 2000) to numerically solve the governing equations that ensure the conservation of mass, momentum, thermal energy, and composition:

$$\nabla \cdot \mathrm{u}' = 0$$

Equation 5.1

$$-\nabla P' + \nabla \cdot \left(\eta'(\nabla \mathbf{u}' + (\nabla \mathbf{u}')^T)\right) + (Ra_T T' + Ra_C C)\hat{\boldsymbol{e}}_{\boldsymbol{Z}} = 0$$

Equation 5.2

$$\frac{\partial T'}{\partial t} + \mathbf{u}' \cdot \nabla T' = \nabla^2 T'$$

Equation 5.3

$$\frac{\partial C}{\partial t} + \mathbf{u}' \cdot \nabla C = 0$$

Equation 5.4

where the primed variables represent dimensionless variables, non-dimensionalised as follows:

$$T' = \frac{T}{\Delta T} \qquad t' = \frac{\kappa}{h^2}t \qquad \mathbf{u}' = \frac{h}{\kappa}\mathbf{u} \qquad P' = \frac{h^2}{\eta_0 \kappa}\left(P - \rho_0 g(h - z)\right) \qquad \eta' = \frac{\eta}{\eta_0}$$

and the thermal and compositional Rayleigh numbers, Ra_T and Ra_C, are defined as follows:

$$Ra_T = \frac{\rho_0 g \alpha \Delta T h^3}{\kappa \eta_0} \qquad\qquad Ra_C = \frac{\Delta \rho g h^3}{\kappa \eta_0}$$

All variables used in the above equations are defined in Table 5.1. We use the Boussinesq approximation and assume incompressibility, with no shear, adiabatic or radiogenic heating, which reduces the complexity of the system in order to allow for the clearer investigation of its primary features.

We use a purely viscous, non-Newtonian, rheology for all materials. Brittle behaviour is not included as it is deemed not to play a significant role in our region of interest: namely subducting crust and mantle wedge, below the over-riding plate. Instead, we impose a maximum viscosity of 10^{24} Pas, which limits the maximum stresses achievable within the rheologically stronger regions of the model. During preliminary work, it was apparent that dislocation creep dominates throughout the model region. This is in line with the findings of Karato and Wu (1993), who put the dislocation-diffusion creep transition between 200km and 300km depth, and with the fact that dislocation creep is more likely to dominate in high-stress regimes such as around subduction zones. As such, the viscosity (η) is calculated as follows:

$$\eta = A^{\frac{1}{n}} \dot{\varepsilon}^{\frac{1-n}{n}} \exp\left(\frac{E}{nRT}\right)$$

Equation 5.5

All variables in the above equation are defined in Table 5.1. The effect of pressure on viscosity is assumed to be negligible as the model domain is shallow, and is partly offset by the omission of adiabatic heating, which has an opposite effect on the rheology. It is expected that the inclusion of pressure effects and adiabatic heating would increase the viscosity at the bottom of the model area by no more than a factor of 3.2 (based on an activation volume of 14 $x10^{-6}$ m^3mol^{-1} for dislocation creep (Karato and Jung, 2003) and an adiabatic gradient of 7.8 $^oC/GPa$). This is small compared to the viscosity uncertainties due to variations in flow law parameters arising from uncertainty in the subducting crustal composition, as well as discrepancies between different rheological studies (Figure 5.2).

Material is defined to be either mantle or crust, both with different flow laws (A, E and n) and densities. The density of crust relative to mantle material (Δρ) is assigned a fixed negative value

above a certain "eclogitisation depth" and a fixed positive value below (see Table 5.1). This is included as a first order effort to simulate the effect of densifying phase changes (eclogitisation) expected to take place in the subducting crust (see Section 5.2.5 for details).

5.2.2 Model Setup

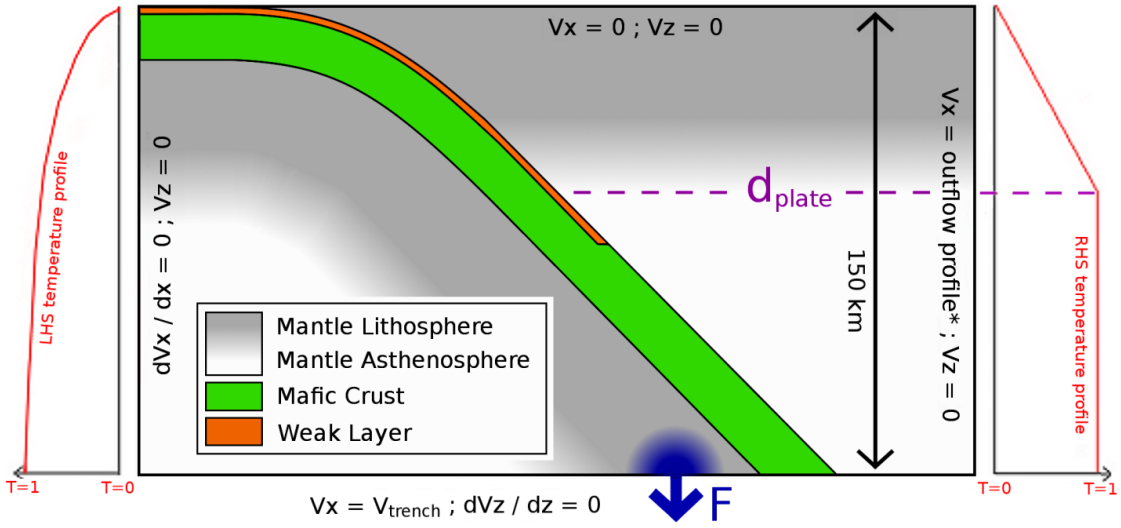

Figure 5.1 Schematic representation of the model setup with thermal and mechanical boundary conditions. Green area marks the position of crustal material and is given a thickness $\mathbf{d_{crust}}$ *, the location of the weak zone (see main text for further details) is depicted in orange, and the overriding plate is defined to extend down to* $\mathbf{d_{plate}}$*. The artificial slab pull force* **F** *is applied over an area within the slab mantle which is free to move laterally (indicated in blue).* $\mathbf{V_{trench}}$ *is applied to the bottom boundary to mimic the effect trench migration has on the subduction geometry*
**The outflow flow profile is Vz= 0 above* $\mathbf{d_{plate}}$ *and Vx =* $\mathbf{V_{trench}}$ *at the bottom boundary with Vx linearly interpolated in between*

The model domain is 450 x 150 km divided up into 512 x 256 finite elements. These elements are 600 x 600 m in a region of interest around the subducting slab and mantle wedge and 1200 x 600 m outside. The thermal and mechanical boundary conditions are illustrated in Figure 5.1. The mechanical boundary conditions are as follows: Vx = Vz = 0 (no slip) on the surface boundary; Vx = V_{trench} (see below) and dVz/dz = 0 (stress free) on the bottom boundary at 150 km; dVx/dx = 0 (stress free) and Vz = 0 (no slip) on the left hand side; and Vx is linearly interpolated between Vx = 0 at z = d_{plate} and Vx = V_{trench} at z = h with Vz = 0 (no slip) on the right hand side. The thermal boundary conditions are: T=0 (0°C) at the surface; T=1 (ΔT or mantle temperature, see Table 5.1) at 150km; the left hand side boundary is given the thermal profile of a half-space which has been conductively cooled from above for a certain period of time: the "slab age" (see Table 5.1); and the right hand side boundary is given the linear thermal profile of an older plate where we

assume that the base of the plate has been kept at a constant temperature by convective processes and the heat-flow through the plate is purely conductive and in steady-state.

In order to avoid modelling the full slab extending throughout the upper mantle, we approximate its presence by applying a slab pull force, *F*, achieved by applying a body force within the slab mantle at the bottom boundary. The bottom Vx boundary condition, V_{trench} , approximately mimics the effect of slab roll-back in the reference frame of the overriding plate, and allows for the subduction angle to be a controllable variable. Throughout the runtime of the model, the magnitudes of *F* and V_{trench} are automatically adjusted such that a fixed, controllable, incoming plate velocity and subduction dip angle are achieved (see Table 5.1). By using this technique we neglect the effects of feedbacks between behaviour in our model and larger scale slab dynamics.

Randomly distributed tracers at an average density of ~60 per element are advected with the flow to carry compositional information. Tracer velocities are conservatively interpolated between nodes to prevent gaps in tracer density forming in areas of high shear (Wang et al., 2015). A weak zone, 1.2 km wide, is imposed to decouple the two plates. Its position is defined using these tracers and it has a fixed low viscosity (see Table 5.1), which is logarithmically interpolated to the background viscosity over 10 finite elements (6 km).

During the model run time, the subducting crust is initially subjected to artificial stresses, resulting from the system finding its steady state geometry. We first run each model calculation with a uniformly strong (10^{23} Pas) crust, during an “initialisation stage” until it reaches a quasi-steady state temperature profile in order to prevent these stresses from deforming the crust. After this initialisation stage, all parts of the model are given their proper rheological properties, as described above.

5.2.3 Parametric Study

Four default models are constructed for our parametric study. The first two "modern-day defaults" have reasonable values for a typical modern day subduction zone with convergence rates of 4.5 and 5 cm/yr, respectively. The other two "Archean defaults" are identical, but with an increased mantle temperature (+200ºC) and thicker subducting crust (15 km rather than 7 km). A parameter sensitivity study of these four default model setups is then undertaken by systematically isolating and varying key parameters about the default model but within the parameter’s bounds (see Table 5.1 for the values of these bounds). The varied parameters are incoming slab age, subduction convergence rate, subduction angle, mantle temperature, over-riding lithosphere thickness, crustal thickness, crustal buoyancy, “eclogitisation” depth (see Section 5.2.5), plate coupling (via viscosity of the imposed weak zone, see Section 5.2.2), mantle

rheology, and crustal rheology. The default and bounds for each parameter are chosen to be representative for realistic subduction zones (and assuming that Archean crustal composition is similar to today's (see Section 5.4.4)) as well as to capture the full range of behaviours.

5.2.4 Rheological Parameter Values

It is recognised that the behaviour of the system is particularly sensitive to the choice of flow laws and as such the default and bounds for the mantle and crustal rheologies are informed by a thorough literature study. See Section 2.3.2 for details of this study. Values for the viscosity were calculated for a range of temperatures (300 – 1700 K) and strain rates (10^{-18} - 10^{-10} s^{-1}) for each flow law, and the logarithmic mean viscosity and standard deviation (SD) found. Flow laws were then fit to the mean and its ±1 SD using least squares regression.

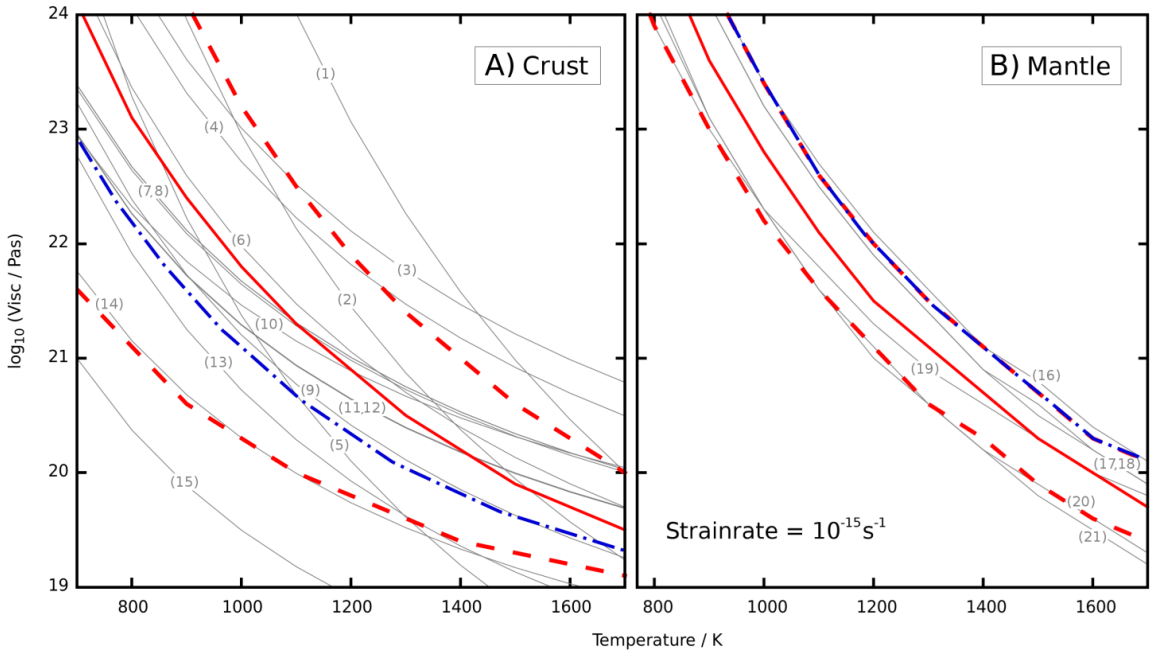

Figure 5.2 The viscosity-temperature relationships at a constant strain rate of 10^{-15} s^{-1} according to: the flow laws listed in Table 2.2 (in grey); the logarithmic mean viscosity flow law (solid red line); and the +/- 1 standard deviation (of the logarithm of the viscosity) flow laws (dotted red line) for the mantle (A) and the crust (B). The default flow laws used in both parametric studies is highlighted by the dashed blue lines.

The ±1 SD flow laws for mantle material are used as the bounds in this parametric study and the +1 SD as the default as this best represents dry peridotite. All mantle flow laws give modern-day upper mantle viscosities of order 10^{20} Pa s (Figure 5.2), in line with the conclusion of Hirth and Kohlstedt (2003) and estimates from isostatic rebound observations (Walcott, 1973). The experimentally derived crustal flow laws show a large variability with the collection of 15 studies

showing a spread of viscosities over 4 orders of magnitude at temperature conditions of 800K (Figure 5.2). This is in part due to the inclusion of a variety of crustal materials, an approach deemed appropriate as the uppermost subducting crust is likely to consist of a mixture or "melange" of mafic crust and subducted sediments (Marschall and Schumacher, 2012) with the extent of mixing and the hydration state of these materials uncertain. All hydrated mafic flow laws lie near to or below the mean, with dehydrated mafic crust lying above and felsic material around the -1 SD flow law. As such, the -1 SD and mean crustal flow laws are used as upper and lower bounds for crustal material, respectively, and a flow law exactly halfway between used as the default. The default model therefore has a rheology that well represents the behaviour of hydrated mafic crust). The upper bound of the crustal rheology is a realistic upper bound for hydrated mafic crust while the lower bound is realistic for a more felsic crust.

The effects of both dehydration (Hirth and Kohlstedt, 2003; Karato and Jung, 2003) (which can occur at highly variable depths (Bouilhol et al., 2015; Magni et al., 2014)) and partial melting (Hirth and Kohlstedt, 2003) on the rheology are uncertain. In addition to this, inclusion of dehydration involves modelling processes beyond the scope of this study. For these reasons, the effect of dehydration is not considered.

5.2.5 Crustal Density and Eclogitisation Depth

Subducting mid-ocean ridge basalts densify via metamorphism, a process that we refer to here as "eclogitisation". The thermokinematic models of Duesterhoeft et al. (2014) demonstrate that this eclogitisation leads to gradual densification of the subducting mafic crust, which becomes negatively buoyant in the mantle below 100 km. However, there is seismic (Garth and Rietbrock, 2014), geodynamic (Gutscher et al., 1999; van Hunen et al., 2004) and field evidence (Austrheim, 1987; Hacker, 1996) showing that the mafic crust may remain metastable and therefore buoyant at greater depths, particularly if the crust is dry (Hacker, 1996). In addition, the effects of partial melts (not considered in this study) can reduce crustal densities considerably. See Section 5.4.4 for a more thorough discussion on the eclogitisation depth. As such, $\Delta\rho_{crust}$ = -300 kg/m^3 is used above an eclogitisation depth of 140 km (as default) and $\Delta\rho_{crust}$ = +200 kg/m^3 below. This eclogitisation depth and the crustal density above this depth are both varied as part of the parametric study. The effect of eclogitisation depth is investigated separately in more detail by running a further set of models that systematically explore the convergence rate – eclogitisation depth parameter space, the results of which are presented in Section 5.3.4.

5.3 Results

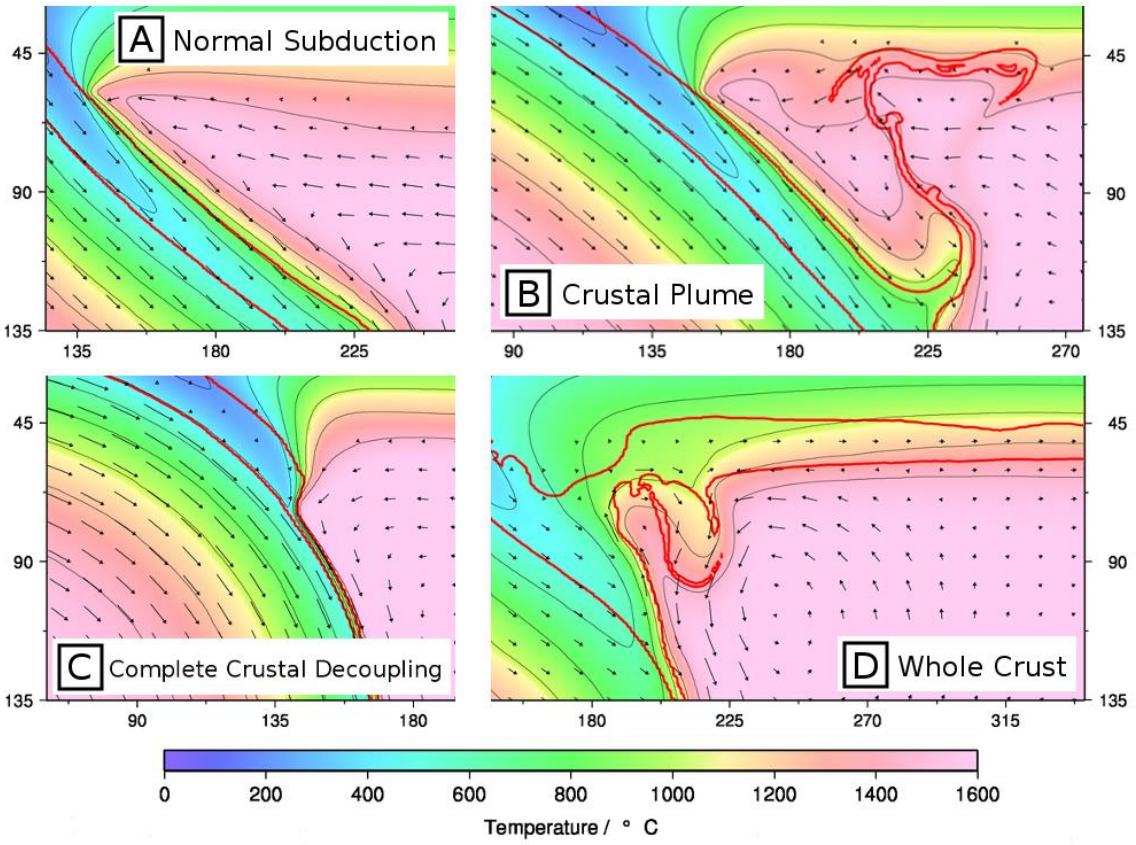

Figure 5.3 Snapshots of the Archean default model with convergence rate 5 cm/yr (panel A), which exhibits normal subduction and the Archean default model with convergence rate 4.5 cm/yr (panel B), in which a small, deep crustal plume forms, model A5_CR_LB (panel C), which displays complete crustal decoupling (Section 5.3.3) and model A5_V_2 (panel D) which displays whole crust delamination (Section 5.3.2). Crustal material is outlined in red.

We performed four sets of parametric studies, in each of which physical parameters were varied about a specific default model. Two default models apply to a modern day subduction system and the other two apply to an Archean setting, in which the mantle is made 200 K hotter and the crust is 15 km thick (Abbott et al., 1994) rather than 7 km thick. In the modern day default models, "normal" steady state subduction (i.e. no break-off or relamination) is observed. Normal subduction is also observed in the Archean default model with convergence of 5 cm/yr. However, upward removal of a portion of the mafic slab crust and subsequent underplating, henceforth referred to as relamination, occurs in the Archean default model with convergence of 4.5 cm/yr. These particular default models, with convergence rates of 4.5 cm/yr and 5 cm/yr, were chosen such that one Archean default model exhibits plume behaviour while the other does not, in order to allow for the investigation of the switching on/off behaviour of all parameters. Models that exhibit relamination appear to lie on a spectrum between a smaller scale, episodic behaviour that

we refer to as “crustal plume” behaviour (Figure 5.3B, described in section 5.3.1) and larger scale, continuous behaviour that we term “whole crust” behaviour (Figure 5.3D, described in Section 5.3.2). Table 5.2 and Figure 5.4 summarise the results of the two parametric studies, listing the conditions required to achieve crustal relamination. A key result to be noted from these results is that relamination does occur under a wider range of conditions in Archean models in comparison to modern day models.

Default	**Model**	**Condition**	**Depth of detachment (km)**	**Degree of relamination (km^2)**	**Velocity of plume (cm/yr)**
Modern 5 cm/yr	M5_CR_LB	LB crustal rheology	73	260	20
	M5_V_2	v_{plate} = 2 cm yr^{-1}	72	395	20
Modern 4.5 cm/yr	M4.5_CR_LB	LB crustal rheology	60	340	30
	M4.5_V_LB	v_{plate} = 2.5 cm yr^{-1}	106	227	10
	M4.5_MT_UB	ΔT = 1550 °C	129	120	40
	M4.5_CD_UB	$\Delta\rho_{crust}$ = −500 kg m^{-3}	96	260	20
Archean 5 cm/yr	A5_An_UB	Θ = 60°	120	106	30
	A5_CD_UB	$\Delta\rho_{crust}$ = −500 kg m^{-3}	106	866	70
	A5_MT_UB	ΔT = 1650 °C	114	190	60
	A5_V_2	v_{plate} = 2 cm yr^{-1}	75	1217	10
	A5_CR_LB	LB crustal rheology	Complete crustal decoupling		
	A5_CT_22	d_{crust} = 22 km	Complete crustal decoupling		
Archean 4.5 cm/yr	A4.5_default	Default	120	183	40
	A4.5_An_UB	Θ = 60°	96	169	30
	A4.5_An_LB	Θ = 30°	119	343	60
	A4.5_CD_UB	$\Delta\rho_{crust}$ = −500 kg m^{-3}	100	680	40
	A4.5_OPT_LB	d_{plate} = 20 km	111	254	60

	A4.5_MT_UB	ΔT = 1650 °C	96	289	50
	A4.5_PC_LB	LB plate coupling	115	131	40
	A4.5_V_2.5	v_{plate} = 2.5 cm yr^{-1}	93	461	30
	A4.5_V_3.5	v_{plate} = 3.5 cm yr^{-1}	90	525	40
	A4.5_CR_LB	LB crustal rheology	Complete crustal decoupling		
	A4.5_CT_22	d_{crust} = 22 km	Complete crustal decoupling		

Table 5.2 Summary of cases where relamination behaviour is observed, with the depth of detachment of material from the slab and the degree of relamination (a quantitative indication of the volume of crustal material expected to be removed from the slab: the method used to calculate the degree of relamination is described fully in the main text), and the peak vertical velocity of the crustal plume for each case. The depth of detachment is calculated as the shallowest depth of crustal material moving net upwards at the point of the formation of the first instability (or point "A" in Figure 5.5). LB stands for "lower bound". Some models don't show relamination as they exhibit complete crustal decoupling instead (see Section 5.3.3 and Figure 5.3C).

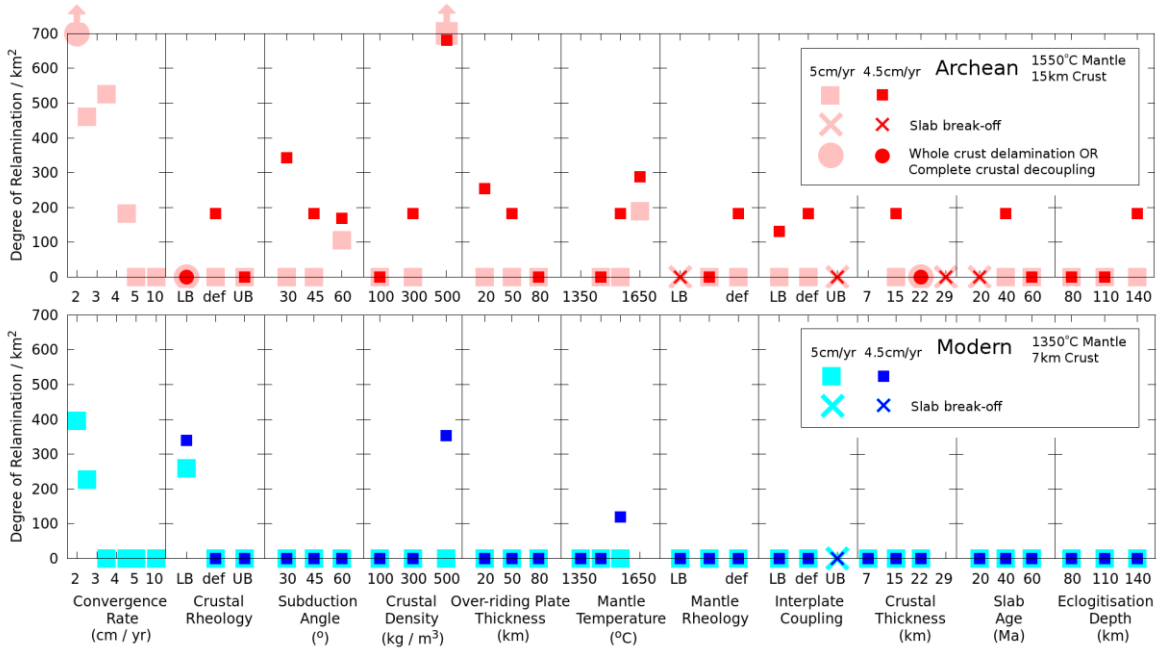

Figure 5.4 A graphical summary of the degree of relamination (see text for definition). Red symbols represent the Archean model runs and blue the modern day model runs. Darker, smaller symbols represent models where the default has a convergence rate of 4.5 cm/yr and lighter, larger symbols, 5 cm/yr. The circles represent Archean models that display relamination behaviour that is morphologically distinct from the normal "crustal plume" mode of relamination (see Section 5.3.2 and 5.3.3). Crosses represent model runs that displayed slab break off instead of subduction (see Section 5.4.3). "LB" stands for lower bound , "def" for default and "UB" for upper bound.

5.3.1 Crustal Plume Behaviour

In models that display crustal plume behaviour, the top-most 2-3 km of crust becomes weak enough to form a Rayleigh-Taylor instability that subsequently feeds a plume consisting of crustal material that rises through the mantle wedge, driven by its compositional buoyancy (Figure 5.5). Please follow this link for an animation of such a crustal plume: https://drive.google.com/open?id=0ByxwST3vd-ttQ0N1WHNYeVlRcGM .

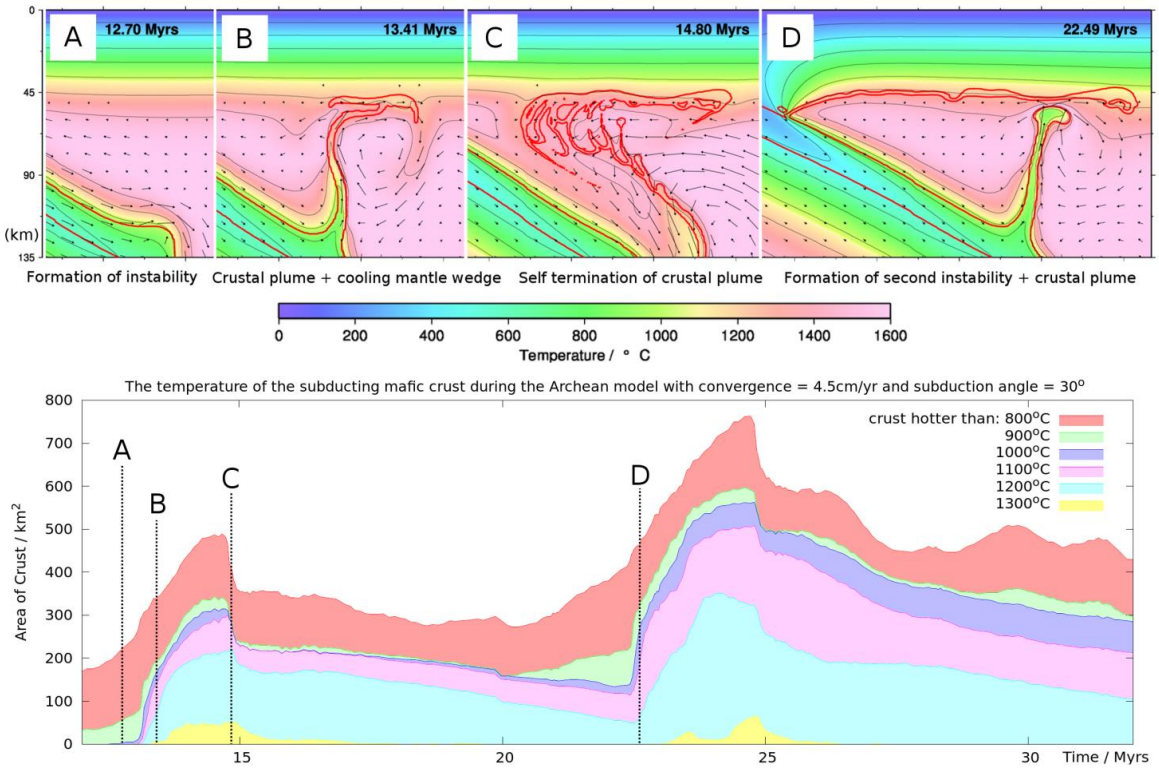

Figure 5.5 The progression of a crustal plume in model A4.5_An_LB (Archaean model with convergence 4.5 cm/yr and a subduction angle of 30°). The coloured curves give the area of crust, which is hotter than the indicated isotherm, through time in the 2D model. This is used as a proxy for the amount of relaminating material present. Four key stages in the crustal plume cycle are identified: A) the formation of the initial instability; B) the development of the crustal plume and cooling of the mantle wedge; C) the self-termination of the crustal plume; D) the formation of a second instability. The upper panels are model snapshots at points A, B, C, and D in which crustal material is outlined in red.

Convergence velocity strongly influences the development of these instabilities, with lower values promoting crustal plume development. When using the modern-day default with convergence 5 cm/yr, crustal plumes can be switched on by using the lower-bound crustal (i.e. felsic) rheology or decreasing the subduction convergence rate to ~2 cm/yr. For the modern-day default with convergence 4.5 cm/yr, raising the mantle temperature or decreasing the crustal density also produces crustal plumes. In the Archean default with convergence 5 cm/yr, crustal plumes form

under all the above conditions and also when the angle of subduction is significantly steeper than 45^{o}. The default Archean model with convergence 4.5 cm/yr is just slow enough to form crustal plumes without adjustment. But decreasing the eclogitisation depth to shallower than 140 km, increasing the slab age, decreasing mantle viscosity, decreasing the mantle temperature, increasing the over-riding plate thickness, decreasing the crustal density, or increasing the crustal strength all have the effect of switching off the crustal plumes.

Figure 5.5 summarises the evolution of a model which shows typical crustal plume type behaviour. Relamination starts with the formation of an instability on the subduction interface (stage A), which corresponds to the start of an increase in the area of hot crustal material within the model, as this material is separated from the slab and heated in the mantle wedge. As the plume develops (stage B), crustal material is fluxed into the mantle wedge, which causes the mantle wedge to cool. At stage C, the mantle wedge has cooled by typically 100-300^{o}C and along with it, the surface of the newly incoming slab. At this point, the surface of incoming crust is too cold and strong to relaminate, the source of the crustal plume is shut off and the crustal plume self-terminates. This is accompanied by a rapid removal of some of the colder relaminating material and surrounding cooled mantle. There is then a period where the ponded crustal material is gradually heated from below by the mantle wedge flow, with some of this material being caught in this flow and cycled around the mantle wedge. This causes some undulations in the thermal evolution of the crust (see curves between points C and D in Figure 5.5). Eventually, the subduction interface becomes hot enough for another instability to form, which feeds a new crustal plume (stage D). The period of the episodicity of this behaviour is defined as the time between the formation of the two crustal plumes (points A and D) and is typically ~10 Myrs although it ranges from 3 Myrs to 16 Myrs. In Archean conditions, crustal plumes rise fast through the mantle wedge, with velocity peaks of tens of cm/yr (40-80 cm/yr), typically taking only 100-200 kyrs to reach the base of the overriding plate. Usually the second plume forms deeper in the model than the first as the mantle wedge is cooler overall, which is particularly apparent in the modern day models. A cooler mantle wedge means a cooler slab top so plumes take longer to form but also means, in certain cases, that the mantle wedge becomes too strong to flow above the original plume. This second reason is more apparent in the modern day models which display relamination. However, in reality this may not happen as it is believed that the mantle wedge is weakened, possibly by a few orders of magnitude (Billen and Gurnis, 2001), by hydration/serpentinisation (Gerya et al., 2002; Hilairet et al., 2007), something not explored in this study but that we argue might be crucial for subduction to be robust against sudden dynamic temporal changes in Chapter 6.

All models that show crustal plume type behaviour have a similar evolution with points A, B, C and D easily identifiable. However, there is great variability in the depth at which these instabilities form and the amount of crustal material that is removed from the slab and eventually ponds below the over-riding plate. We define the depth of detachment as the shallowest depth of crustal material moving upwards at the point in time of the formation of the first instability (stage "A" in Figure 5.5), and the amount of relamination as the area of crust that has passed the 900^{o}C isotherm, at the peak of the first crustal plume event. We use this measure as it offers a proxy for the amount of crust removed from the slab: the more crust that is removed, the more crust heats up to these high temperatures in the mantle wedge. In addition, it gives us a first order handle on the relative amounts of melt one could expect. These values are listed in Table 5.2, for all models that show relamination. Archean models lie on a spectrum between normal subduction with no relamination (Figure 5.3A), through models which display smaller, more short-lived crustal plumes that form deeper in the model (up to 120 km, Figure 5.3B), to the "whole crust" end member, described below, for which the instability forms shallower, ~10-40 km below the over-riding plate, and crustal input into the mantle wedge is continuous (Figure 5.3D). We observe a negative correlation between the depth of detachment and the amount of relamination in both the Archean and modern-day models, implying that crustal plumes that detach from the slab shallower are usually larger.

5.3.2 Whole Crust Relamination

It is possible for almost the entire crust to detach from the slab upon entering the mantle with only a small portion of material leaving through the bottom of the box (see Figure 5.3D). This only occurs under Archean conditions and if the convergence is slow (~2 cm/yr). In this model, the initial Rayleigh-Taylor instability forms at a depth between 75 and 90 km, or ~10-40 km below the overriding lithosphere. Unlike the crustal plume behaviour, this behaviour is not transient, with continued input of crustal material into the mantle wedge upon continued subduction and a new mantle wedge flow developing below the relaminating crust. As such, the definition of the "amount of relamination" (see Section 5.3.1) has to be altered for this model as there is no peak associated with a plume event. Instead, the amount of crustal material that has crossed the 900^{o}C isotherm after 10 Myrs from point A is used. All mantle material above the relaminating crust is cooled to < 900^{o}C and therefore has lithospheric strength. The new mantle wedge below the crust behaves as it does under normal steady state subduction only with most crust flowing laterally above it, with only a small amount of crust, subducted with the slab, underlaying it.

5.3.3 Complete Crustal Decoupling

In Archean models where the lower crust is comparable in strength to the imposed inter-plate weak-zone prior to subduction, either because the crust is thick (>22 km) or rheologically weak, the lower crust assumes the role of the decoupling interface. The result of this is that the crust no longer subducts (Figure 5.3C).

5.3.4 The Effect of Eclogitisation

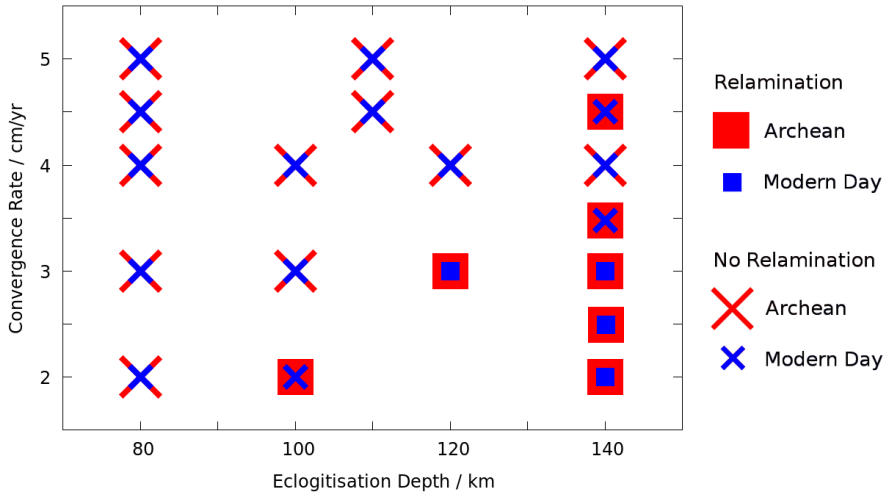

Figure 5.6 Graphical summary of the results of the parametric study of the effects of convergence rate and eclogitisation depth on relamination (see Section 5.3.4).

A further set of model calculations was performed to determine the required eclogitisation depth for a given convergence rate (Figure 5.6). It was found that the formation of the smaller, deeper plumes at moderate convergence rates (4 cm/yr), requires an eclogitisation depth of 140 km. However, for the larger, shallower relamination events which occur at slower convergence rates (2 cm/yr) an eclogitisation depth of 100 km is sufficient. The plumes that form at the faster convergence rates are smaller and form deeper in comparison to the crustal plumes that form at slower convergence rates. The result that relamination occurs at 4.5 cm/yr but not at 4 or 5 cm/yr when the eclogitisation depth is 140 km in Archean models, is due to the fact that this region is at the boundary between behavioural regimes. Any small changes under these conditions can result in markedly differing behaviours due to the fact that this system is very non-linear. This chaotic behaviour is also demonstrated in Figure 5.4, panel 1.

5.4 Discussion

5.4.1 Conditions for Crustal Relamination in Modern Subduction Zones

Crustal plume behaviour can occur, under modern-day subduction zone conditions, when a weak rheology (e.g. for sediments or felsic crust; see Section 5.2.4) is used. Indeed, modern-day felsic and sedimentary material can relaminate from the subducting slab in the form of mantle wedge plumes (Behn et al., 2011; Castro et al., 2013; Gerya and Yuen, 2003b; Marschall and Schumacher, 2012; Vogt et al., 2013), also known as "cold plumes" (Gerya and Yuen, 2003b). The only condition under which material, which is as strong as hydrated mafic crust, can relaminate, is when the plate convergence rate is slow enough (<5 cm/yr or as low as ~2 cm/yr in a mantle at modern day temperatures with crust of relative density <+500 kg/m^3). This is primarily because, in slower subduction systems, the crust has more time to form Rayleigh-Taylor instabilities above the eclogitisation depth. In addition, as we demonstrated in Chapter 3, the temperature of the subducting crust is primarily speed controlled: slower slabs are hotter. This means that slower slabs must also have weaker crusts helping instabilities to form. This is particularly important for whole-crust relamination in Archean models (see Section 5.3.2).

5.4.2 Crustal Relamination in the Archean

As in the modern-day cases, the parameter with the strongest control on relamination behaviour appears to be the subduction convergence rate. However, when subduction is slow (2 cm/yr) under Archean conditions, "whole-crust" relamination is observed (see Section 5.3.2). A much larger amount of crust is involved in the relamination process when compared directly to the modern-day equivalent (amount of relamination ~4 times higher). In addition to this, crustal plume relamination now occurs under a far wider range of conditions. These results give strength to our original hypothesis that the relamination of the subducting crust was more viable in the early Earth.

The fact that one Archean default model displays relamination and the other does not allows the effects of all parameters to be gauged. The result that increased crustal buoyancy promotes relamination is perhaps unsurprising as with higher buoyancy forces, instabilities form more readily. Subduction with a hotter mantle means the crust heats faster, which leads to faster weakening and promotes the formation of instabilities. Steepening subduction means that slabs are more aligned with the direction of gravity, which leads to increased stress weakening.

Whether subduction operated more slowly in the Archean is unclear. More dehydration stiffening near Archaean MORs may have led to consistently slower plate tectonics in the early Earth

(Korenaga, 2006) (though this has been argued against (Davies, 2009)) or perhaps episodic subduction, interrupted by intermittent slab break-off events (Moyen and Van Hunen, 2012; van Hunen and van den Berg, 2008). Episodic subduction may have had a particularly dramatic effect on relamination as during periods of slab stagnation the convergence rate is effectively zero. Stagnating mafic slab crust would heat up in such a situation, ideal conditions for the formation of crustal plumes. We explore what happens to the temperature of the subducting crust upon episodically driven subduction in Chapter 6 and find that, during a slow-down period, the crust can heat up significantly, particularly the lower crust, which would promote the formation of crustal plumes.

The complete crustal decoupling observed when the crust is made weak (felsic-like in strength) or thick (22 km) (see Section 5.3.3 and Figure 5.3C) has previously been suggested as a possible mode of plate tectonics in the Archean ("flake tectonics") (Hoffman and Ranalli, 1988). Based on proposed Archean conditions, it was argued that the thicker crust, which is hot and weak at its base, may have been more decoupled from the underlying mantle lithosphere, allowing it to fully separate from the subducting slab upon subduction leaving only the mantle lithosphere to sink deeper into the mantle. This mechanism has been shown to be dynamically viable in other modelling studies, provided that a weak enough layer underlays the crust (Davies, 1992; Vogt and Gerya, 2014).

5.4.3 Slab Break-off

Previous studies have suggested that, with a thicker crust, subduction may not have been viable in the early Earth (Davies, 1992; Sizova et al., 2010). This is because, with a thicker crust, buoyancy forces resisting subduction are higher and the overall lithospheric strength weaker. Indeed, in Archean models we find that slab break-off is more likely to occur when the crust is thickened (to ~29 km in our models) or the slab made too young (~20 Myrs), shutting down subduction. However, subduction with episodic, spontaneous break-off has been shown to be a viable mode of subduction in the Archean and may also explain the absence of ultra-high-pressure metamorphic rock from this time (Sizova et al., 2014; van Hunen and van den Berg, 2008).

5.4.4 The Composition and Density of the Subducting Crust

We have undertaken an extensive parametric study to constrain the conditions required for crustal relamination and investigate the effect of various subduction parameters on this

behaviour. In our default models, the depth to which the crust remains buoyant (i.e. the eclogitisation depth) is 140km. Additional simulations demonstrated that for larger crustal plumes to develop at slower velocities, an ecologitisation depth of 100 km is sufficient. However, an ecologitisation depth of 140 km is required for the development of smaller, deeper crustal plumes (see Section 5.3.4). The reason for choosing 140 km as a default eclogitisation depth is motivated by the evidence that the subducting crust remains metastable during its prograde path. Indeed, the geological record of exhumed ultra-high-pressure terranes (e.g. Western Norwegian Caledonides, Sulu belt, Eastern China) show that mafic material has resisted the transformation to eclogite well within the eclogite-facies conditions (some as deep as >90 km), save for along hydrated veins (Austrheim, 1987; Zhang and Liou, 1997). This petrological evidence for a delayed eclogitisation, has been confirmed by the geophysical observation that slab crust remains seismically slow compared to mantle to great depths (>150 km) (Abers, 2000; Garth and Rietbrock, 2014). Such significant delays in eclogitisation have also been invoked to explain flat slab subduction of oceanic buoyant plateaus, arguing that the bulk of this plateau crust must remain buoyant at the depth at which the slab flattens (typically ~150 km) for timescales of several Myrs (Gutscher et al., 1999; van Hunen et al., 2004). We have therefore used these observations to postulate that if the subducting crust is subject to eclogitisation delays, then the bulk crust may remain metastably buoyant.

As highlighted by the results in Section 5.3.4, the deepest, smallest scale crustal plumes require a deep eclogitisation depth and are therefore most likely to be prevented by densification reactions. However, these small plumes only form from the topmost 1-2 km of subducting crust, which is likely to consist of a melange of mafic subducting crust and sediments (Gerya and Yuen, 2003b; Marschall and Schumacher, 2012). In this case, the physical addition of sediments to the oceanic crust would significantly affect the bulk density of this heterogeneous layer, leading to an even more buoyant slab top. In addition, along the warm subduction gradients of an “Archean subduction zone” the oceanic slab crust may undergo partial melting (Bouilhol et al., 2015) leading to significantly lower density (Gerya and Yuen, 2003b).

In this study, our modelled Archean crust is assumed to be thicker than its modern equivalent but similar in composition. The nature of the Archean oceanic lithosphere is much debated. At higher mantle potential temperatures, more mantle material is processed at the ridge, leading to a thicker, MgO-rich oceanic crust. This thicker crust might have been stratified, in a similar way to modern oceanic plateaus, being more basaltic (MORB-like) at the top and more ultramafic / komatiitic at depth (Kerr et al., 1997). As such, MORB properties might be appropriate for the top-most Archean crust but the lower crust may have been denser and stronger. This would affect

neither the eclogitisation depth nor the crustal plume behaviour, but could hinder the removal of the deeper parts of the crust from the slab during whole-crust relamination.

5.4.5 Magmatic Output and Archean Continental Crust Formation

Although studying the magmatic output of this process is beyond the scope of this work and we do not compute it in our models, it is worth noting that during normal subduction, under Archean conditions, very little crust heats up to above 800^{o}C and no crustal material heats up to above 900^{o}C within our model region. However, as Figure 5.4 illustrates, the area of mafic crustal material that heats up to above 900^{o}C when relamination occurs (the "amount of relamination") can be substantial (typically a few 100 km^2, but ~1000 km^2 after 10Myrs in the whole-crust relamination case). At this temperature, partial melting of mafic material is likely to occur, particularly if the system is being percolated by metamorphic fluids (Magni et al. 2014, Bouilhol et al. 2015). In all cases crustal plume material reaches these melting temperatures within the mantle wedge (at >50km depth in our models) and, as such, has the potential to explain the high pressure mafic signature, pervasive in Archean terranes (Foley et al., 2002; Martin, 1999).

Episodic crustal plumes may result in episodic magmatism (Marschall and Schumacher, 2012) and previous studies on Archean terranes have suggested episodicity in their formation with a typical timescale of a few Myrs (Moyen and Van Hunen, 2012), the same timescale under which crustal plumes operate in our models. The variability of the depth of formation of the crustal instability, the variability in the size of the subsequent relamination event, and the fact that shallow instability formation correlates with more extensive relamination imply that the degree of crust-mantle interaction may also vary significantly. When crustal plumes form deep and are small, the degree of mantle interaction is likely to be high whereas in the whole-crust relamination case, the crustal relaminant does not have to pass through the hot mantle wedge at all and potential melts from the ponded crustal material will only pass through mantle lithosphere, which is <900^{o}C.

Our results demonstrate that more extensive and shallow relamination is more likely under the hotter mantle conditions of the early Earth. As the mantle probably cooled through the Archean (Herzberg et al., 2010), crustal relamination may have gradually transitioned from shallow and extensive to small-scale and deep. The result of this may have been a gradual transition from crust derived melting at relatively shallow depths with minimal mantle interaction, to crust derived melting at greater depths with greater mantle interaction. Interestingly, this trend in depth and degree of mantle interaction is observed in the composition of Archean felsic terranes of different ages (Martin and Moyen, 2003). This has previously been cited as evidence for, on average, shallower subduction in the Archean, which gradually steepens through Earth's history

(Abbott et al., 1994), or a secular change in the depth of slab melting through time (Martin and Moyen, 2003). Here we offer secular changes in subducting crust dynamics as an alternative explanation.

5.5 Conclusions

We performed two sets of parametric studies to investigate how different key parameters can affect subduction dynamics and, in particular, the possibility for the detachment of the subducting mafic crust from the slab and subsequent upwelling and underplating (or "relamination"), in a modern day setting and early Earth setting (with a 200 K hotter mantle and 15 km oceanic crust). Under modern day conditions, crustal relamination is only observed when the crust has a "felsic" flow law (thus confirming previous studies) or when subduction is slow (<5 cm/yr or ~2 cm/yr for modern mantle temperatures and a realistic crustal density). Slowing down subduction, raising mantle temperature and decreasing crustal density or strength also enhances relamination in the early Earth models. However, in these Archean models, so does making the overriding plate thinner, making the subduction angle significantly steeper or shallower than 45^{o}, making the slab younger, or making the mantle stronger. Relamination of the mafic crust requires that the crust remains buoyant in the mantle to depths greater than the equilibrium eclogitisation depth in all but the most extreme (slow convergence) cases. This may be achieved by mixing with more buoyant sediment, partial melting or the slow kinetics of eclogitisation in the absence of water.

Crustal strength and subduction convergence rate have the strongest control and, when the crust is made weak enough or subduction is slow enough (~2 cm/yr), the entire mafic crust is able to detach from the slab and relaminate. We demonstrate that crustal relamination behaviour exhibits a spectrum between this whole-crust end member (which occurs at relatively shallow depths) through an episodic "crustal plume" mode (which occurs deeper and is typically episodic on a ~10 Myr timescale), to no relamination. We suggest that this trend may explain secular changes in the degree of mantle interaction and depth of primary magma production of Archean felsic terranes over time. It is also observed that, under early Earth conditions, continuous subduction is less viable if the oceanic crust is too thick (>~20 km), the slab is too young (~20 Myrs), or the inter-plate coupling high, due to spontaneous slab-breakoff. Finally, when drawing a direct comparison between the modern day and early Earth parameter studies, we find that relamination of subducting mafic crust is a viable mechanism under a wider range of subduction conditions in an early Earth subduction zone and has the potential to be more substantial. This has implications for the generation of magmatism in Archean subduction zones, Archean subduction dynamics, and the long term recycling of mafic crust.

6 On the Feasibility and Potential Consequences of Episodic Subduction

6.1 Introduction

It has been suggested that, due to raised mantle temperatures in the Archean, subducting slabs should be hotter. We also observe this in the model calculations of Chapter 3: increasing mantle temperatures by 200^{o}C increases slab temperatures by ~100^{o}C on average. Higher temperatures lead to increased rates of solid state creep and also may result in the lithosphere being percolated by asthenospheric melts (Sizova et al., 2010). As a result, it is likely that tectonic plates were weaker in the early Earth. It has also been proposed that the mafic oceanic crust was thicker due to increased amounts of decompression melting at mid-oceanic ridges (van Thienen et al., 2004b). This thicker crust would further weaken the slab as crustal material is weaker than the mantle. Another effect of a thicker crust would be to potentially increase tensile stresses in the slab as it undergoes eclogitisation: going from less dense to more dense than the surrounding mantle (gabbro being buoyant in the mantle and eclogite being denser than the mantle) (van Thienen et al., 2004a). Due to all these reasons, it has been suggested that sustained subduction was rare in the early Earth and instead, may have been intermittent with frequent and spontaneous slab break-off (Rey et al., 2014; Sizova et al., 2015; van Hunen and van den Berg, 2008) (Figure 6.1) if it occurred at all. Episodicity in arc magmatism is perhaps observable in some Archean terranes as geological evidence for this behaviour (Moyen and Van Hunen, 2012). The readiness of slabs to break off in Earth's past has been offered as an explanation for the lack of (undisputed) ultra-high-pressure metamorphism prior to the Phanerozoic (Sizova et al., 2014). It would also be a solution to the "thermal catastrophe" problem, explaining why the rate of heat loss from the Earth appears to be, counterintuitively, lower in the past compared to today (Silver and Behn, 2008). In addition, it could explain why mantle mixing rates appear to have been slower in the early Earth (O'Neill et al., 2013), since subduction is responsible for recycling material back to the deep mantle. However, these final two points may also be explained by invoking a type of longer term episodicity where long periods of stagnation (on the order of 100s Myrs) are punctuated by large over-turn events which gradually evolves into modern day continuous plate tectonics (Lourenço et al., 2016; O'Neill et al., 2007). Another explanation might be that subduction was continuous but slower as perhaps plates were stronger or more buoyant due to the higher levels of melting related depletion dehydration at mid-oceanic ridges (Korenaga, 2006). However, this is obviously in opposition to the arguments presented above.

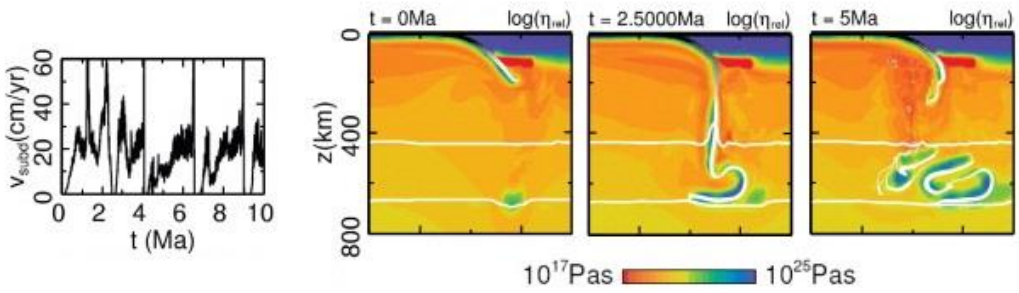

Figure 6.1 A plot of subduction velocity through time as well as snapshots of a model produced by van Hunen and van den Berg (2008) which illustrates episodic subduction (figure adapted from (van Hunen and van den Berg, 2008))

In the models of van Hunen and van den Berg (2008), when slab breakoff occurs, subduction velocities drop to zero before gradually returning to their original velocity at which point the process repeats (Figure 6.1). In the models of Sizova et al. (2015) and Rey et al. (2014) a period of subduction appears to occur once, lasting 3 Myrs and 10 Myrs respectively. As demonstrated in Chapter 3, the temperature of the subducting crust should be highly speed dependent. As such, we might expect the temperature of the crust to increase during the slow parts of this episodic subduction cycle, or at the beginning of one subduction event, perhaps to the point of crossing its solidus (~800^{o}C for hydrated mafic crust). In Chapter 5 we also demonstrate that slow subduction significantly increased the likelihood of relamination and, as such, we might also expect episodic subduction to be accompanied by increased occurrence of relamination. Here we undertake a preliminary study of the effects of episodic subduction with the aim of getting a first estimate on the effect it might have on the thermal state of the subducting plate.

6.2 Method

We set up a model, which is nearly identical to the models used in Chapter 3. Therefore the reader is referred to Table 3.1 for values of all unstated input parameters used in this model. This is a 2D numerical model of subduction, extending down to 200 km and driven from below by an adjustable, artificial slab pull force. This allows for the slab velocity to be controlled during the run time of the model. The mantle and crust are given rheologies informed by a literature study (Section 2.3.2), the two plates decoupled by a weak zone (Section 2.2.4) and all boundary conditions are the same as for the models used in the other modelling chapters in this thesis. The model is also initialised in the same way as the models used in the previous chapters (Section 2.2.2). The slab dip and age are set to intermediate values according to the study of slab

parameter in subduction systems on Earth today (Section 3.2.3) at 45^{o} and 40 Myrs respectively. The decoupling depth is set at 50 km, which is on the shallow end of the range explored in Chapter 3. The mantle temperature is set to 1550^{o}C to better reflect Archean conditions but the thickness of the crust is set to 7 km just like in the Archean models of Chapter 3. To study the effect of episodic subduction, the slab speed is made time dependent. The model initialises with the slab subducting at 8 cm/yr. Then, starting at 12 Myrs after the beginning of the model run (several Myrs after the initialisation period), this is reduced to 1 cm/y over a period of 1 Myrs. This mimics the consequence of an event of deep slab break-off, which would remove most of the slab pull that drives subduction. The slab velocity is subsequently linearly increased back up to 8cm/yr over a period of 7 Myrs (Figure 6.2a). This saw-tooth signal in the slab velocity is observed in the models of van Hunen and van den Berg (2008) (Figure 6.1). This timescale is representative of what was found in the previously mentioned modelling work: longer than the 2-3 Myrs of Sizova et al. (2015) and van Hunen and van den Berg (2008) but shorter than the 10 Myrs of Rey et al. (2014). It also matches the timescales of the proposed geological evidence (5-10 Myrs) (Moyen and Van Hunen, 2012).

In reality, the mantle wedge is likely weaker than ambient asthenosphere due to a number of reasons. In particular, the mantle wedge is likely hydrated (and therefore rheologically weaker), particularly in the coldest parts, directly above the slab, which are potentially cold enough and hydrated enough to be serpentinised (Hacker et al., 2003). Some estimates of serpentinite strength lie between 10^{19}-10^{20} Pas (Gerya et al., 2002; Hilairet et al., 2007) and it is believed that only ~20% serpentinisation is needed to significantly reduce the overall bulk strength of the rock (Escartin et al., 2001). In addition, the presence of melt within the mantle wedge can act to weaken it. It has previously been suggested that the mantle wedge does indeed need to have a reduced viscosity to match observation (Billen and Gurnis, 2001). We observed in Chapter 5 that mantle wedge weakening is perhaps even required for subduction to be robust to sudden temporal changes. As such, the model is run twice, once with all materials given the same maximum viscosity as used in the previous models (10^{24} Pas, see Section 2.3 for details) and one run where the mantle wedge has a viscosity which is capped at 10^{22} Pas. Such a cap means the coldest parts of the wedge, which are the most likely to be serpentinised, have a viscosity of 10^{22} Pas, at the strongest: a conservative amount of weakening.

6.3 Results and Discussion

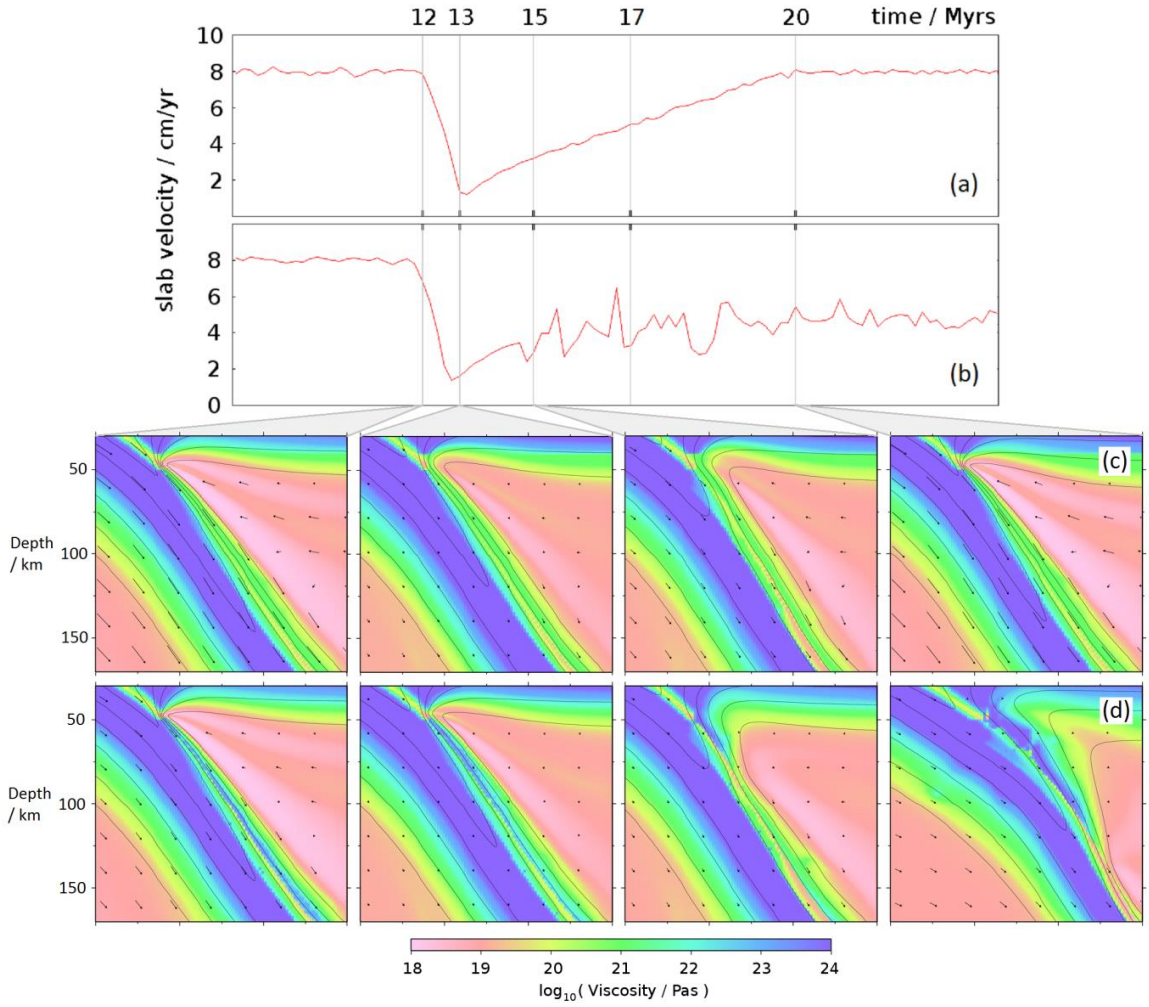

Figure 6.2 a) Plots of subduction velocity through time for the model with a lowered mantle wedge viscosity maximum and b) the model without such a lowered maximum. The marked times correspond to the snapshots in the panels below and also the panels in Figure 6.3. c) Viscosity profiles of the model with a lowered mantle wedge viscosity maximum. d) Viscosity profiles of the model without such a lowered maximum. The black lines in the viscosity plot are 200°C isotherms.

Model snapshots are presented in Figure 6.2(c and d) at the onset of "slab-breakoff" (12 Myrs), completion of slab-breakoff (13 Myrs), during the period of the slab speeding up (15 Mrys) and the end of the reduced velocity period (20 Myrs). Figure 6.2(a and b) are plots of the actual slab velocity (as opposed to the velocity aimed for) with time. Panel (a) is the model run with a weaker mantle wedge and, as can be seen, the desired velocity envelope is achieved. Panel (b) is the model run without a weakened mantle wedge. After the sharp reduction in velocity, the slab speed never fully recovers. This is despite the slab pull force being increased at a fixed rate to attempt to reach the target velocity. This indicates that, in reality, where slab pull is only a limited force, subduction would simply cease.

Looking at the model snapshots below, the reason why becomes apparent. After the reduction in velocity, the mantle wedge flow is shut off. It is this flow of hot asthenosphere into the nose of the mantle wedge that keeps this region hot and therefore rheologically weak. Without it, conductive cooling from the slab and the overriding plate reduces the temperature of the corner of the mantle wedge and increases its viscosity. This couples the two plates below the depth of the imposed weak zone which stops at 50 km. When the slab pull force is increased, cold and strong material from the overriding plate is dragged down with the subducting plate, and subduction becomes almost two-sided. This doesn't happen when the viscosity of the mantle wedge is capped to 10^{22} Pas, as this prevents the material in the nose from becoming strong enough to couple the plates. In that case, subduction completely recovers by the time the slab velocity is back to its original velocity. This perhaps indicates that, for subduction to be resilient to such sudden reductions in convergence rate, a mechanism is indeed required that weakens the mantle wedge, in particular the coldest parts: potentially serpentinisation. It could also indicate that the assumption of the decoupling weak zone abruptly stopping at a fixed depth, independent of subduction conditions, is invalid when looking at subduction systems that have properties, e.g. convergence rate, which change significantly in time.

Next, we focus on the model with the capped mantle wedge viscosity, in which subduction dynamics returned to normal after the "break-off" event, as observed in the models of van Hunen and van den Berg (2008). We are interested to see what effect this stalling has on slab temperature and whether or not this process could potentially catalyse slab melting. In Figure 6.3, temperature profiles of this model are presented with the slab crust outlined in red. The slowing of subduction means the slab crust heats up (mirroring results in Chapter 3). As the slab speeds up again, colder slab from above follows this heated section on its way down, resulting in a cold front that advances down the slab preceded by the hottest crust. This is most easily seen between 15 Myrs and 17 Myrs. When it reaches ~150 km (in the 17 Myr panel) this hottest part of the crust has a Moho temperature which is almost 200^{o}C hotter than the Moho during the steady state subduction that precedes the simulated "slab break-off" event (in the 12 Myr panel), and a slab top which is ~150^{o}C hotter. A substantial amount of crust in this hot section is at temperatures >800^{o}C, hot enough to melt under hydrous conditions (Poli and Schmidt, 2002). Another effect this increase in temperature may have is to promote the formation of crustal plumes, as hypothesised in the discussion of Chapter 5. With a full parametric study, where crustal and mantle density and rheology would be varied along with the slab parameters: age, speed and angle, we may observe this happening under certain conditions and be able to quantify the amount by which slow-down events of different lengths promote relamination. Such a study

would also help us to quantify the amount by which the temperature of the heated section of crust is raised, under different conditions.

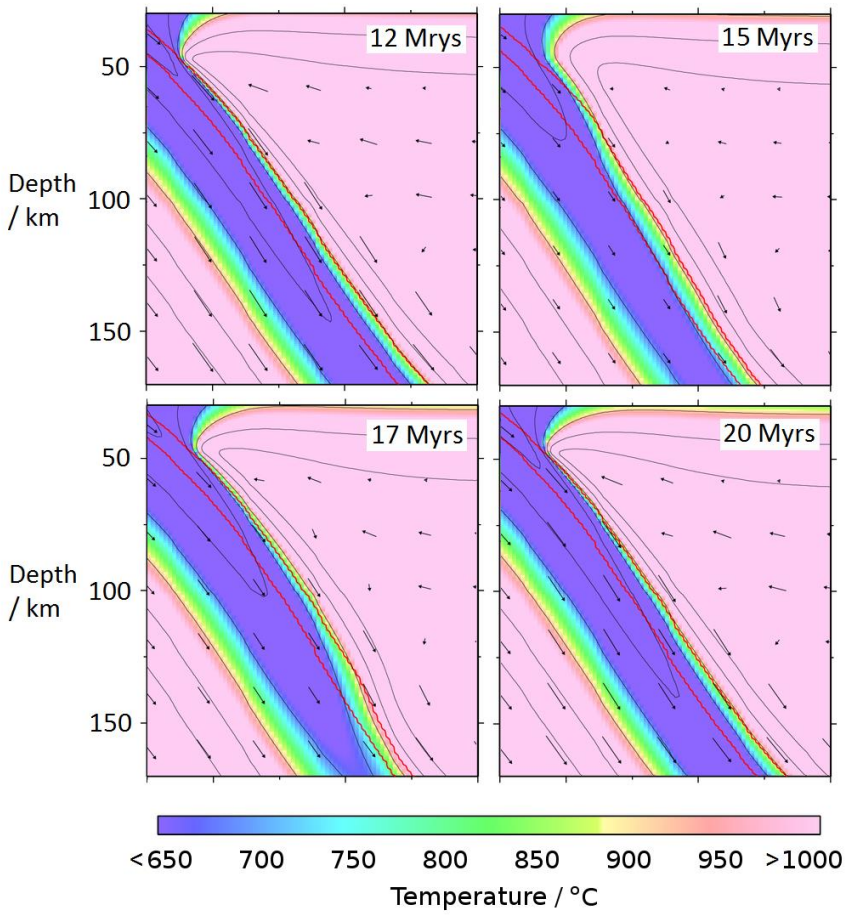

Figure 6.3 Temperature plots for the model with a lowered mantle wedge viscosity cap. Black contours are 200°C isotherms. The temperature scale is saturated above 1000°C and below 650°C so temperature changes within the crust are easier to see. The crust is outlined with a red line.

Linking of the numerical models to a thermodynamic database would help us to understand more precisely how the increased crustal temperature and changes in the mantle flow during such a slow-down event might affect subduction related melting processes and, in particular, whether one might expect the subducting crust to melt at all. Such extension may also allow us to link this parametric study to observables. Modern analogues of this process occurring today might be areas where it is believed that subduction is initiating or has just initiated, such as the Philippines or where subduction is simply very slow, such as the Lesser Antilles (slow with an old slab) or Cascadia (slow with a young slab). We could look at the geochemical data from modern day volcanic arcs, in a similar way to the work undertaken for Chapter 4 and look for systematic

differences between these regions and the global average subduction system to see whether they can be explained by our predicted dynamics.

6.4 Conclusions

The results of this preliminary study hint at two things. Firstly, in order for subduction to be robust against sudden reductions in convergence rate, either an additional weakening mechanism is required in the coldest parts of the mantle wedge or the decoupling weak zone operates in a more complicated way than having a terminus at a fixed depth. Secondly, if subduction is allowed to recover, a section of crust can heat up to ~150^{o}C hotter than under steady state conditions which may lead to crustal melting although we would like to conduct a more rigorous study before we reach this conclusion.

7 Conclusions and Suggestions for Further Work

7.1 Thesis Summary

Subduction and the associated arc magmatism are of key importance in the study of many Earth systems as they control the cycling of surface materials, water in particular, back into the mantle. It is believed that volcanic arcs are the sites of continental crust formation today (Davidson and Arculus, 2006) and that this may even extend back to the Archean (van Hunen and Moyen, 2012). The thermal state of slabs is thought to be of great importance in the generation of arc magmatism. The temperature of slabs affects dehydration, the primary driver of arc magmatism, but may also determine whether the slab itself undergoes partial melting. The main aims of this thesis have therefore been to gain insight into what determines slab temperatures and exactly what effect this has on arc magmatism today and back in Earth's early history. This is reflected in the following individual studies.

7.1.1 Improving on the Thermal Parameter

In Chapter 3 we started by first investigating how slab dynamics affect slab temperature, coming to the conclusion that, above the base of the over-riding plate or the "decoupling depth" (the point at which mantle wedge flow becomes coupled to the sinking plate), the temperature of the whole plate is dominantly controlled by the slab's age. Below the decoupling depth, the subducting mantle is still dominantly age controlled but the temperature of the crust is primarily controlled by the convergence rate. However, if the decoupling depth itself is allowed to vary, we find that this actually dominates over the three slab parameters in determining the temperature of the subducting crust, down to 40 km below the range within which the decoupling depth is varied. One goal was to improve on a proxy for slab temperature known as the slab "thermal parameter" (Kirby et al., 1996), defined as its age multiplied by its subducting velocity and the sine of its dip angle. The reason for this motivation is that it has been shown that the thermal parameter doesn't perform well as a proxy for slab temperatures at the depths which are important for the generation of arc magmatism (Syracuse et al., 2010). With regards to this, we found that, firstly, angle plays very little role in determining slab temperatures and, if anything, has the *opposite* effect on slab top temperatures around the decoupling point. Secondly, we observed that this thermal parameter becomes a better slab temperature proxy with depth. We

weren't able to significantly improve on this thermal parameter for slab mantle temperatures below ~50 km below the decoupling depth. From this work, we suggest that any temperature dependent process within the slab should depend on slab age, convergence rate and (to a lesser extent) angle, differently depending on where in the slab the process is thought to take place. Such processes include the various metamorphic, and potentially fluid releasing, reactions that occur in the subducting slab as well as slab seismicity and the propensity of subducting plates to form crustal or cold plumes (the focus of Chapter 5). We also investigated the effect of raising mantle temperatures and observed that, even with a mantle which is 200^{o}C hotter, the results of this study do not change significantly. The primary difference is an increase in slab top temperatures by ~100^{o}C in all models within the parametric study.

7.1.2 Can We See the Same Dependences in the Trace Element Characteristics of Arc Lavas?

Chapter 4 aimed to build on the results of Chapter 3 by attempting to link them to real world observables: the trace element geochemistry of subduction related arc magmatism. We started with the hypothesis that slab temperatures may influence the concentrations of different trace elements in the lavas that erupt at the surface above. To this end, we developed a tool to look for correlations between the global geochemical database GeoRoc and the global geophysical databases SubMap (Heuret and Lallemand, 2005), a global database of subduction zone physical parameters, and Crust1.0 (Laske et al., 2013), a global database of crustal thickness. We performed tests of correlation between 63 element ratios and slab age, convergence rate, slab dip and overriding crustal thickness. We aimed to make these tests statistically rigorous, removing outliers and calculating a statistical significance, so we can be sure that what we observe are genuine trends in the data.

Before even involving the geochemical data, one of our most striking findings is the strong anti-correlation between slab dip and overriding crustal thickness. This finding alone immediately suggests that one needs to be careful in interpreting correlations between slab parameters and geochemical data as these cross correlations can exist. We observe that certain elements correlate strongly with crustal thickness and as a result, correlate with slab dip as well. The clearest example of this is the correlation between the concentrations of titanium, yttrium and ytterbium and crustal thickness, which results in these elements apparently positively correlating with slab dip. An anti-correlation between heavy rare earth elements, such as Y and Yb, and the crustal thickness beneath volcanic arcs, has indeed previously been proposed (Chiaradia, 2015; Mantle and Collins, 2008; Profeta et al., 2015) and as such, this finding confirms this previous work and gives us confidence in our method. The currently accepted mechanism for this trend is

based in fractionation processes and we also find that correlation is reduced when the most evolved magmas are filtered out lending further support to this hypothesis.

We also observe similarity in the way chemically similar elements behave, such as Y and Yb (both heavy rare earth) but also Nb and Ta, as well as Hf and Zr, as to be expected. When using our tool to achieve the original goal of looking for trends in the geochemistry which might be slab derived, we first look at the behaviour of thorium, commonly thought to be an indicator of sediment melting (Johnson and Plank, 2000). Of all the elements we investigate it does appear to (anti-)correlate more strongly with convergence rate than any other element, something which becomes stronger when the more evolved magmas are filtered out. This agrees with our previous finding that slab top temperatures are dominantly controlled by convergence rate. However Uranium, which is fluid mobile, appears to behave nearly identically to Thorium. Uranium is carried into subduction zones in the sediments like thorium but is fluid mobile. This may either indicate that sediment fluid release is controlled by convergence rate in a similar way to sediment melting or that both U and Th are actually released from sediments in the same way, perhaps supercritical fluids as suggested by Kessel et al. (2005).

We also analyse the behaviour of the "adakitic" signatures Sr/Y and La/Yb. Both signatures have a strong correlation with slab age, as has previously been suggested and offered as evidence that high Sr/Y and La/Yb are results of slab melting. However, a couple of observations seem contrary to this idea. Firstly, there is no correlation between Sr/Y or La/Yb and convergence rate like there is for Th (and U), which should be the main control on crustal temperatures. Secondly, the strength of correlation between Sr/Y or La/Yb and slab age decreases when the most evolved magmas are excluded. As such, the results with regards to the adakitic signature are by no means conclusive. However, we do believe this tool enables for a statistically robust way of analysing geochemical and geophysical data and could potentially be used for further investigation. In particular, a recently released compilation of the most primitive lavas (Schmidt and Jagoutz, 2017) (believed to best represent the source prior to fractionation) could be used as an input and then compared to our current results to potentially further understand the role of the slab.

7.1.3 Relamination Involving the Mafic Subducting Crust

A well-documented feature of the rock record is that Archean rock differs systematically from more modern continental crust and modern arc rock in its geochemistry. In particular, Archean rock is more "adakitic", high Sr/Y and La/Yb as discussed above (Martin, 1999). This adakitic signature can potentially be produced by the melting of mafic material at mantle wedge depths (Defant and Drummond, 1990). Motivated by looking for a possible dynamic explanation for this

trend, in Chapter 5 we investigated the possibility of mafic crust relamination which would likely result in extensive melting of mafic material. We conducted two sets of parametric studies in which a number of subduction parameters were varied: one with a "modern-day" range for the parameters and another with a raised mantle temperature and thicker subducting crust, thought to be applicable to any subduction in the Archean. We find that mafic crust relamination is indeed more likely to occur under Archean conditions. In addition to this key result, we find that the spectrum of behaviours that we observe ranges from deeper, smaller, and intermittent "crustal plumes", which reoccur on a ~10 Myr timescale, similar to the crustal or "cold" plume behaviour suggested by previous studies (Gerya and Yuen, 2003b; Marschall and Schumacher, 2012), to a more extreme, shallower and continuous relamination behaviour which we term "whole crust" relamination. We suggest that a gradual transition from "whole crust" relamination to "crustal plume" relamination explains why Archean TTGs apparently evolved through time: from those with an apparently shallower source and less mantle interaction to those with a apparently deeper source and more mantle contamination (Martin and Moyen, 2003). We also observe that relamination of mafic material may be possible in the modern Earth but only if subduction is slow (<2 cm/yr, velocities which subducting plates do reach during episodic subduction) or if the crust is as weak as felsic material (mirroring what has previously been suggested (Behn et al., 2011)).

7.1.4 The Effects of Episodic Subduction on the Slab

Finally, in Chapter 6 we undertook a preliminary study on the feasibility and consequences of another potential dynamic feature of the early Earth: episodic subduction. Previous numerical modelling (Sizova et al., 2015; van Hunen and van den Berg, 2008) and evidence in the rock record (Moyen and Van Hunen, 2012) suggest that when subduction started in the Earth, it was intermittent. We aimed here to investigate the effect this might have on slab temperatures. Firstly, our models suggest that in order for subduction to be robust against such sudden reductions in convergence rate, either an additional weakening mechanism is required in the coldest parts of the mantle wedge or the decoupling weak zone operates in a more complicated way than having a terminus at a fixed depth. As for a first order indication on the effect on slab temperature, we find that, during a successful stop and restart cycle of ~8 Myrs, a section of crust can heat up to ~150^{o}C hotter than under steady state conditions. As such, this behaviour should have an effect on slab dehydration and possibly induce slab melting or even crustal relamination.

7.1.5 Overall Thoughts

Plank et al. (2009) suggest there are two main ways that we can learn more about the role of the subducting plate in the generation of arc volcanism: 1) forward modelling through the use of numerical simulations of subduction systems and 2) working back from observation, primarily the geochemistry of the lavas themselves. In this thesis, we have aimed to use both to advance our knowledge about the behaviour and role of subducting plates in the generation of arc magmatism. The end products are the results and conclusions we have summarised in this final chapter and also a set of tools which we hope to use to continue both the forward and backward lines of investigation with potential directions discussed in the next section.

Taken together, our results demonstrate that the role of the slab (and its thermal state) in the generation of arc magmatism, is certainly complex. The thermal state itself is a function of a number of slab parameters and we show that a single simple proxy, such as the thermal parameter, is not sufficient to describe it. However, we have shown that numerical modelling work can be used to go beyond and improve upon this thermal parameter. We have also developed a working tool to analyse global chemical and physical data related to subduction systems in a statistically rigorous way. Using this tool we have gleaned some suggestions that the thermal state of the slab does indeed play a role in the generation of arc magmatism. However, the classic “slab melt” signature, or “adakitic” signature, appears to be a far more complex one, with conflicting indications that either the slab might play a role, or that it arises due to processes within the overriding plate. In the future we aim to shed more light on this topic through further use of this tool. We also demonstrated that relamination may have an important role in the generation of the adakitic signature; perhaps not necessarily on Earth today but, because relamination of mafic material is more likely in a hotter mantle, it could explain the observation that the majority of Archean rock is more “adakitic” than modern continental crust.

7.2 Suggestions for Further Work

7.2.1 Linking the Numerical Models to a Thermodynamic Database

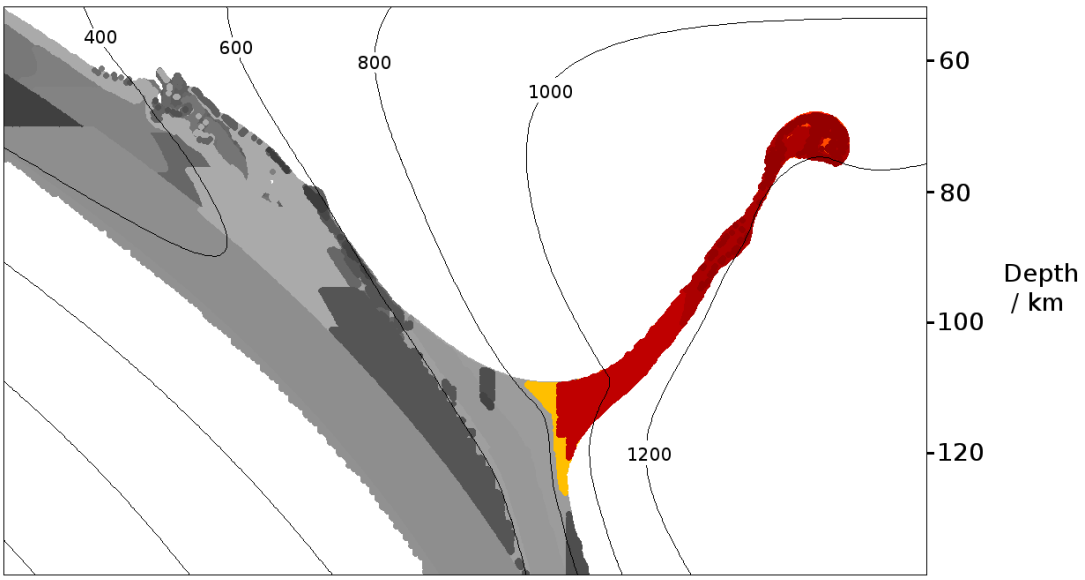

Figure 7.1 A map of equilibrium phases generated by linking a numerical model from Chapter 5 to a thermodynamic database. The subducting plate plunges from the top left and a crustal plume is ascending through the mantle wedge. Calculations are only performed for the hydrated slab mantle and the crust (including the plume). Each region with a different mineral assemblage is coloured a different colour. Assemblages without melt present are coloured in greyscale and areas where melt is present are coloured in yellow-red. The "step-like" nature of the contacts between areas with different mineral assemblages is due to the resolution (in pressure and temperature) of the method used to perform this analysis. If we were to use this tool in the future we would need to increase the resolution.

One very important aspect of numerical modelling is comparing the results to real world observables. The results of the modelling work undertaken for this thesis are mainly dynamical whereas the data we analyse are primarily geochemical. This is true for a lot of geodynamic modelling work. Bridging the gap between these two research aspects has proved to be a powerful way to yield valuable new insight: data can be used to further inform the models, and models can be used to further understand the data. However, direct and quantitative comparison is complex; meaning linking data to the models is often done in a qualitative and speculative way. Much linking between modelling results and actual data is done in this way in this thesis. A first step towards a more quantitative approach would be to extract the pressure, temperature and compositional fields from the numerical model and use a thermodynamic database to calculate the equilibrium mineral assemblages at all points. This would enable us to predict petrological observables from the models. We performed such a linking to get a first order view of how much crustal melting one might expect upon the formation of a crustal plume in Chapter 5. For this we

used the database PerpleX (Connolly, 2005) using a method outlined by Bouilhol et al. (2015). This method crucially takes into account the movement of water, propagating it instantaneously upwards after release via dehydration reactions. An example of this being applied is given in Figure 7.1. Melting begins right at the inception of the formation of the crustal plume, enhanced by the influx of water from the hydrated slab mantle below and, in the hottest parts of the plume, can reach melt fractions in excess of 30%. From this, we can be more confident that one consequence of mafic crust relamination would indeed be extensive melting of mafic material. A link to a clip of a test model, ran with melt tracked (plotted as a white over-lay on a viscosity plot), as well as an additional feature: a third rheological layer to represent subducted sediment (outlined in blue, whilst the mafic crust is outlined in red) can be found here: https://drive.google.com/open?id=0ByxwST3vd-ttZE5CTGxNZndDV2c . Materials in this test model are given very weak rheologies (non-hydrated mafic crust is given the weakest or "more felsic" flow law of Chapter 5) but demonstrate the capabilities of this method, particularly the ability to track melting as the model progresses.

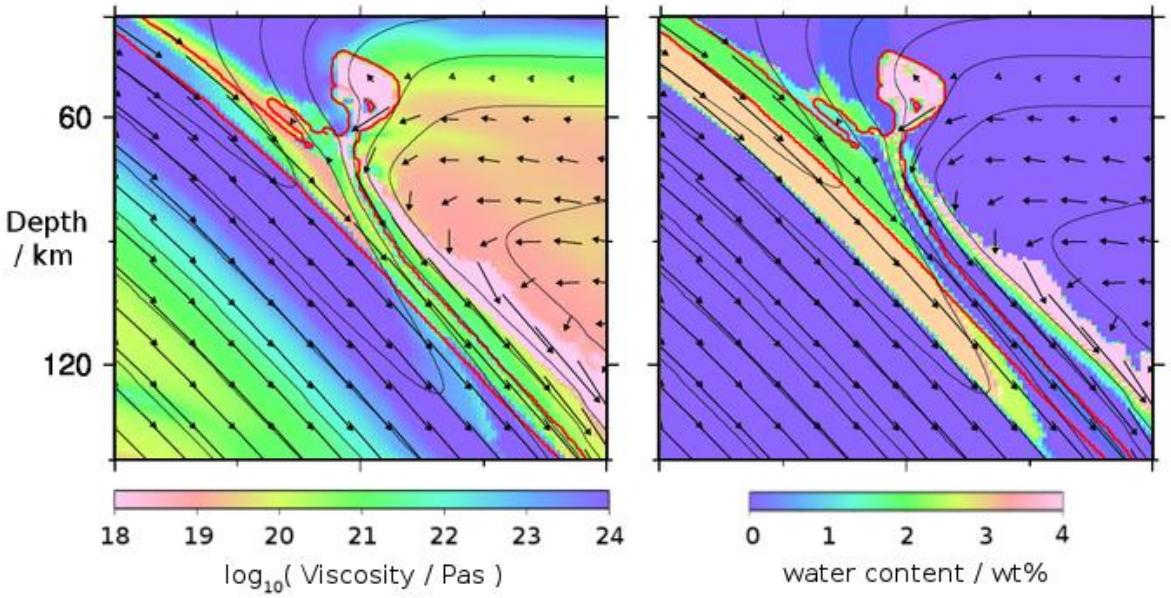

Figure 7.2 A test model with a hydration state dependent rheology. The left panel is a viscosity plot and the right panel the water content. The strength of materials is decreased by a factor of 100 if there is water present. Melting is allowed to occur but isn't extracted from the models, which is what is giving rise to the high water contents within the crustal plume and in a band in the mantle wedge above the slab. The crust is outlined in red and 200°C isotherms in black.

Another possible prediction that could be made by linking the models to a thermodynamic database is the major element composition of any resulting melt and of the residue. However, doing this requires the major element composition of material within the model to be dynamic

and doing this at a high enough resolution becomes very computationally expensive. Advances in computing technology may allow for this to be a more commonplace technique in the near future. In addition to major element composition, knowing the equilibrium mineral assemblages throughout the model domain may also allow for predictions of trace element concentrations in the fluids and melts generated within the subduction system. This would provide a direct link to the geochemical database analysis work we undertook in Chapter 4 (which, as we mentioned previously, we aim to update by using recently refined geochemical data) as well as with similar work.

It would also be possible to map observables such as seismic velocity by using the predicted mineral assemblages, in a similar way to Gerya et al. (2006), as well as to use this information to feedback into the model in the form of a density map or even used to include a more advanced compositionally dependent rheology. We have already tested a simple rheology dependent on the hydration state of materials: in this model, subduction is modelled in a very similar way to the models in Chapter 5, but hydrated material is made 100 times weaker than dehydrated material as a very rough approximation. This could be made more realistic by including a hydrated crust flow law and a dehydrated crust flow law, which could be determined by literature study in a similar way as outlined in Section 2.3.2. This test model is presented in Figure 7.2. Such weakening promotes relamination of crustal material as soon as it enters the mantle. Whilst the strength of materials in this test case are likely to be relatively weak, it is likely that the hydration state of materials does play a key role in this and other dynamic subduction related processes, and such a tool would enable us to investigate its effect more fully.

7.2.2 Further Investigations of the Dynamics of Subduction Systems

Other dynamic behaviours that we observed in the models of Chapter 5 include the “complete crustal decoupling” (Section 5.3.3) mode of subduction, which has previously been suggested as a tectonic mode in the Archean, occasionally termed “flake tectonics” (Hoffman and Ranalli, 1988). A more in-depth study of this mechanism could help shed further light on the potential tectonic mechanisms that operated in the Archean. A similar type of behaviour has also been suggested to occur in the modern Earth upon continental collision (lithospheric delamination (Magni et al., 2013)), so this work may also have applicability to the study of collisional settings.

Another type of behaviour that we have only started to investigate here is episodic subduction (Chapter 6). By conducting a full parametric study, in a similar way to Chapter 5, we could begin to constrain aspects of this behaviour. We would aim to answer questions such as: by how much does the crust heat up under different subduction conditions? By performing the link to PerpleX

we could also start to quantify melt volumes and perhaps even compositions. A fuller study would also allow us to assess whether episodic subduction promotes relamination as well as investigate the effects of slowing down subduction for different lengths of time.

Other direct extensions to this work could include extension of the models into 3 dimensions. This is likely to have an impact on relamination behaviour in particular as crustal plumes and diapirs are intrinsically 3D phenomena (Marschall and Schumacher, 2012). The current 2D investigation likely under-estimates how likely they are to form as more energy is required to form a 2D plume (effectively an infinite sheet of material) than a 3D plume. 3D modelling would also allow for the investigation of other subduction parameters on slab temperature such as trench parallel movement of slabs (Yogodzinski et al., 1995).

Throughout this study it became clear that the nature of the decoupling weak zone between the two plates is of great importance and especially where and how it terminates (a result found in other modelling studies also (Syracuse et al., 2010)). To further the investigation of the thermal state of subducting plates and the effect this might have on arc magmatism, we believe that focusing on this decoupling is essential (Arcay, 2012; Wada and Wang, 2009). Investigation into this decoupling would be aided by the use of a numerical code that allows for more local and dynamic mesh refinement. Mesh refinement may also do away with the need for producing a model of just the shallow upper mantle with subduction being artificially driven as in the studies presented in this thesis. It would, instead, be possible, for not much more computational effort, to model the whole upper mantle or even the whole mantle and have subduction occur completely self consistently, while retaining high resolution in the regions of interest such as the mantle wedge and the subducting crust.

Bibliography

Abbott, D., Drury, R., Smith, W.H., 1994. Flat to steep transition in subduction style. Geology 22, 937-940.

Abers, G., van Keken, P., Hacker, B., 2017. The cold and relatively dry nature of mantle forearcs in subduction zones. Nature Geoscience.

Abers, G.A., 2000. Hydrated subducted crust at 100–250 km depth. Earth and Planetary Science Letters 176, 323-330.

Agrusta, R., Goes, S., van Hunen, J., 2017. Subducting-slab transition-zone interaction: Stagnation, penetration and mode switches. Earth and Planetary Science Letters 464, 10-23.

Alonso-Perez, R., Müntener, O., Ulmer, P., 2009. Igneous garnet and amphibole fractionation in the roots of island arcs: experimental constraints on andesitic liquids. Contributions to Mineralogy and Petrology 157, 541-558.

Arcay, D., 2012. Dynamics of interplate domain in subduction zones: influence of rheological parameters and subducting plate age. Solid Earth 3, 467.

Arcay, D., Tric, E., Doin, M.-P., 2007. Slab surface temperature in subduction zones: Influence of the interplate decoupling depth and upper plate thinning processes. Earth and Planetary Science Letters 255, 324-338.

Arculus, R.J., Powell, R., 1986. Source component mixing in the regions of arc magma generation. Journal of Geophysical Research: Solid Earth 91, 5913-5926.

Armstrong, R., Harmon, R., 1981. Radiogenic isotopes: the case for crustal recycling on a near-steady-state no-continental-growth Earth. Philosophical Transactions of the Royal Society of London A: Mathematical, Physical and Engineering Sciences 301, 443-472.

Atherton, M.P., Petford, N., 1993. Generation of sodium-rich magmas from newly underplated basaltic crust. Nature 362, 144-146.

Austrheim, H., 1987. Eclogitization of lower crustal granulites by fluid migration through shear zones. Earth and Planetary Science Letters 81, 221-232.

Bailey, E.H., Ragnarsdottir, K.V., 1994. Uranium and thorium solubilities in subduction zone fluids. Earth and Planetary Science Letters 124, 119-129.

Bebout, G.E., 1996. Volatile Transfer and Recycling at Convergent Margins: Mass-Balance and Insights from High-P/T Metamorphic Rocks. Subduction top to bottom, 179-193.

Becker, T.W., Conrad, C.P., Buffett, B., Müller, R.D., 2009. Past and present seafloor age distributions and the temporal evolution of plate tectonic heat transport. Earth and Planetary Science Letters 278, 233-242.

Behn, M.D., Kelemen, P.B., Hirth, G., Hacker, B.R., Massonne, H.-J., 2011. Diapirs as the source of the sediment signature in arc lavas. Nature Geoscience 4, 641-646.

Billen, M.I., Gurnis, M., 2001. A low viscosity wedge in subduction zones. Earth and Planetary Science Letters 193, 227-236.

Bouilhol, P., Magni, V., van Hunen, J., Kaislaniemi, L., 2015. A numerical approach to melting in warm subduction zones. Earth and Planetary Science Letters 411, 37-44.

Brooks, A.N., 1981. A Petrov-Galerkin finite element formulation for convection dominated flows. California Institute of Technology.

Byerlee, J., 1978. Friction of rocks. Pure and applied Geophysics 116, 615-626.

Calvert, A., Sawyer, E., Davis, W., Ludden, J., 1995. Archaean subduction inferred from seismic images of a mantle suture in the Superior Province.

Caristan, Y., 1982. The transition from high temperature creep to fracture in Maryland diabase. Journal of Geophysical Research: Solid Earth (1978–2012) 87, 6781-6790.

Castro, A., 2014. The off-crust origin of granite batholiths. Geoscience Frontiers 5, 63-75.

Castro, A., Vogt, K., Gerya, T., 2013. Generation of new continental crust by sublithospheric silicic-magma relamination in arcs: a test of Taylor's andesite model. Gondwana Research 23, 1554-1566.

Chertova, M., Geenen, T., van den Berg, A., Spakman, W., 2012. Using open sidewalls for modelling self-consistent lithosphere subduction dynamics. Solid Earth 3, 313.

Chiaradia, M., 2015. Crustal thickness control on Sr/Y signatures of recent arc magmas: an Earth scale perspective. Scientific reports 5.

Chorowicz, J., 2005. The east African rift system. Journal of African Earth Sciences 43, 379-410.

Christensen, U., 1984. Convection with pressure-and temperature-dependent non-Newtonian rheology. Geophysical Journal International 77, 343-384.

Clift, P., Vannucchi, P., 2004. Controls on tectonic accretion versus erosion in subduction zones: Implications for the origin and recycling of the continental crust. Reviews of Geophysics 42.

Condie, K.C., 2005. TTGs and adakites: are they both slab melts? Lithos 80, 33-44.

Condie, K.C., 2015. Earth as an evolving planetary system. Academic Press.

Condie, K.C., Bickford, M., Aster, R.C., Belousova, E., Scholl, D.W., 2011. Episodic zircon ages, Hf isotopic composition, and the preservation rate of continental crust. Geological Society of America Bulletin 123, 951-957.

Condie, K.C., Pease, V., 2008. When did plate tectonics begin on planet Earth? Geological Society of America.

Connolly, J., 2005. Computation of phase equilibria by linear programming: a tool for geodynamic modeling and its application to subduction zone decarbonation. Earth and Planetary Science Letters 236, 524-541.

Cooper, L.B., Ruscitto, D.M., Plank, T., Wallace, P.J., Syracuse, E.M., Manning, C.E., 2012. Global variations in H2O/Ce: 1. Slab surface temperatures beneath volcanic arcs. Geochemistry, Geophysics, Geosystems 13.

Crisp, J.A., 1984. Rates of magma emplacement and volcanic output. Journal of Volcanology and Geothermal Research 20, 177-211.

Currie, C., Wang, K., Hyndman, R.D., He, J., 2004. The thermal effects of steady-state slab-driven mantle flow above a subducting plate: the Cascadia subduction zone and backarc. Earth and Planetary Science Letters 223, 35-48.

Davidson, J.P., Arculus, R., 2006. The significance of Phanerozoic arc magmatism in generating continental crust. Cambridge University Press.

Davies, G.F., 1992. On the emergence of plate tectonics. Geology 20, 963-966.

Davies, G.F., 2009. Effect of plate bending on the Urey ratio and the thermal evolution of the mantle. Earth and Planetary Science Letters 287, 513-518.

Defant, M.J., Drummond, M.S., 1990. Derivation of some modern arc magmas by melting of young subducted lithosphere. Nature 347, 662-665.

Dhuime, B., Hawkesworth, C.J., Cawood, P.A., Storey, C.D., 2012. A change in the geodynamics of continental growth 3 billion years ago. Science 335, 1334-1336.

Duesterhoeft, E., Quinteros, J., Oberhänsli, R., Bousquet, R., de Capitani, C., 2014. Relative impact of mantle densification and eclogitization of slabs on subduction dynamics: A numerical thermodynamic/thermokinematic investigation of metamorphic density evolution. Tectonophysics 637, 20-29.

Eiler, J.M., Carr, M.J., Reagan, M., Stolper, E., 2005. Oxygen isotope constraints on the sources of Central American arc lavas. Geochemistry, Geophysics, Geosystems 6, n/a-n/a.

Elliott, T., Plank, T., Zindler, A., White, W., Bourdon, B., 1997. Element transport from slab to volcanic front at the Mariana arc. Journal of Geophysical Research: Solid Earth 102, 14991-15019.

England, P., Wortel, R., 1980. Some consequences of the subduction of young slabs. Earth and Planetary Science Letters 47, 403-415.

Escartin, J., Hirth, G., Evans, B., 2001. Strength of slightly serpentinized peridotites: Implications for the tectonics of oceanic lithosphere. Geology 29, 1023-1026.

Faccenda, M., Gerya, T.V., Burlini, L., 2009. Deep slab hydration induced by bending-related variations in tectonic pressure. Nature Geoscience 2, 790-793.

Fischer, R., Gerya, T., 2016. Early Earth plume-lid tectonics: A high-resolution 3D numerical modelling approach. Journal of Geodynamics 100, 198-214.

Fisher, R.A., 1949. The design of experiments. The design of experiments.

Foley, S., Tiepolo, M., Vannucci, R., 2002. Growth of early continental crust controlled by melting of amphibolite in subduction zones. Nature 417, 837-840.

Forsyth, D., Uyeda, S., 1975. On the relative importance of the driving forces of plate motion. Geophysical Journal International 43, 163-200.

Furukawa, Y., 1993. Depth of the decoupling plate interface and thermal structure under arcs. Journal of Geophysical Research: Solid Earth 98, 20005-20013.

Fyfe, W., 1978. The evolution of the Earth's crust: modern plate tectonics to ancient hot spot tectonics? Chemical Geology 23, 89-114.

Gaetani, G.A., Grove, T.L., 1998. The influence of water on melting of mantle peridotite. Contributions to Mineralogy and Petrology 131, 323-346.

Garth, T., Rietbrock, A., 2014. Downdip velocity changes in subducted oceanic crust beneath Northern Japan—insights from guided waves. Geophysical Journal International 198, 1342-1358.

Gazel, E., Hayes, J.L., Hoernle, K., Kelemen, P., Everson, E., Holbrook, W.S., Hauff, F., van den Bogaard, P., Vance, E.A., Chu, S., 2015. Continental crust generated in oceanic arcs. Nature Geoscience 8, 321-327.

Gerya, T.V., Connolly, J.A., Yuen, D.A., 2008. Why is terrestrial subduction one-sided? Geology 36, 43-46.

Gerya, T.V., Connolly, J.A., Yuen, D.A., Gorczyk, W., Capel, A.M., 2006. Seismic implications of mantle wedge plumes. Physics of the Earth and Planetary Interiors 156, 59-74.

Gerya, T.V., Stöckhert, B., Perchuk, A.L., 2002. Exhumation of high-pressure metamorphic rocks in a subduction channel: A numerical simulation. Tectonics 21.

Gerya, T.V., Yuen, D.A., 2003a. Characteristics-based marker-in-cell method with conservative finite-differences schemes for modeling geological flows with strongly variable transport properties. Physics of the Earth and Planetary Interiors 140, 293-318.

Gerya, T.V., Yuen, D.A., 2003b. Rayleigh–Taylor instabilities from hydration and melting propel 'cold plumes' at subduction zones. Earth and Planetary Science Letters 212, 47-62.

Gorbatov, A., Kostoglodov, V., 1997. Maximum depth of seismicity and thermal parameter of the subducting slab: general empirical relation and its application. Tectonophysics 277, 165-187.

Gutscher, M.-A., Olivet, J.-L., Aslanian, D., Eissen, J.-P., Maury, R., 1999. The "lost Inca Plateau": cause of flat subduction beneath Peru? Earth and Planetary Science Letters 171, 335-341.

Hacker, B.R., 1996. Eclogite formation and the rheology, buoyancy, seismicity, and H2O content of oceanic crust. Subduction top to bottom, 337-346.

Hacker, B.R., Abers, G.A., Peacock, S.M., 2003. Subduction factory 1. Theoretical mineralogy, densities, seismic wave speeds, and H2O contents. Journal of Geophysical Research: Solid Earth (1978–2012) 108.

Hacker, B.R., Christie, J.M., 1990. Brittle/ductile and plastic/cataclastic transitions in experimentally deformed and metamorphosed amphibolite. Geophys. Monogr., Am. Geophys. Union 56.

Hacker, B.R., Kelemen, P.B., Behn, M.D., 2011. Differentiation of the continental crust by relamination. Earth and Planetary Science Letters 307, 501-516.

Hager, B.H., O'Connell, R.J., 1981. A simple global model of plate dynamics and mantle convection. Journal of Geophysical Research: Solid Earth 86, 4843-4867.

Hawkesworth, C., Dhuime, B., Pietranik, A., Cawood, P., Kemp, A., Storey, C., 2010. The generation and evolution of the continental crust. Journal of the Geological Society 167, 229-248.

Hawkesworth, C., Gallagher, K., Hergt, J., McDermott, F., 1994. Destructive plate margin magmatism: geochemistry and melt generation. Lithos 33, 169-188.

Hawkesworth, C., Turner, S., McDermott, F., Peate, D., Van Calsteren, P., 1997. U-Th isotopes in arc magmas: Implications for element transfer from the subducted crust. Science 276, 551-555.

Helffrich, G., Brodholt, J., 1991. Relationship of deep seismicity to the thermal structure of subducted lithosphere.

Hermann, J., Spandler, C., Hack, A., Korsakov, A.V., 2006. Aqueous fluids and hydrous melts in high-pressure and ultra-high pressure rocks: Implications for element transfer in subduction zones. Lithos 92, 399-417.

Herzberg, C., Condie, K., Korenaga, J., 2010. Thermal history of the Earth and its petrological expression. Earth and Planetary Science Letters 292, 79-88.

Heuret, A., Lallemand, S., 2005. Plate motions, slab dynamics and back-arc deformation. Physics of the Earth and Planetary Interiors 149, 31-51.

Hilairet, N., Reynard, B., Wang, Y., Daniel, I., Merkel, S., Nishiyama, N., Petitgirard, S., 2007. High-pressure creep of serpentine, interseismic deformation, and initiation of subduction. Science 318, 1910-1913.

Hildreth, W., Moorbath, S., 1988. Crustal contributions to arc magmatism in the Andes of central Chile. Contributions to mineralogy and petrology 98, 455-489.

Hirschmann, M.M., 2000. Mantle solidus: Experimental constraints and the effects of peridotite composition. Geochemistry, Geophysics, Geosystems 1.

Hirschmann, M.M., Tenner, T., Aubaud, C., Withers, A., 2009. Dehydration melting of nominally anhydrous mantle: The primacy of partitioning. Physics of the Earth and Planetary Interiors 176, 54-68.

Hirth, G., Kohlstedt, D., 2003. Rheology of the upper mantle and the mantle wedge: A view from the experimentalists. Inside the subduction Factory, 83-105.

Hoffman, P.F., Ranalli, G., 1988. Archean oceanic flake tectonics. Geophysical Research Letters 15, 1077-1080.

Holmes, A., 1931. XVIII. Radioactivity and Earth Movements. Transactions of the Geological Society of Glasgow 18, 559-606.

Houlier, B., Cheraghmakani, M., Jaoul, O., 1990. Silicon diffusion in San Carlos olivine. Physics of the Earth and Planetary Interiors 62, 329-340.

Hughes, T.J., 2012. The finite element method: linear static and dynamic finite element analysis. Courier Corporation.

Hurley, P.M., Rand, J.R., 1969. Pre-drift continental nuclei. Science 164, 1229-1242.

Hyndman, R.D., Peacock, S.M., 2003. Serpentinization of the forearc mantle. Earth and Planetary Science Letters 212, 417-432.

Jagoutz, O., Kelemen, P.B., 2015. Role of arc processes in the formation of continental crust. Annual Review of Earth and Planetary Sciences.

Jaoul, O., Froidevaux, C., Durham, W., Michaut, M., 1980. Oxygen self-diffusion in forsterite: implications for the high-temperature creep mechanism. Earth and Planetary Science Letters 47, 391-397.

Ji, S., Zhao, P., 1994. Layered rheological structure of subducting oceanic lithosphere. Earth and planetary science letters 124, 75-94.

Johnson, M.C., Plank, T., 2000. Dehydration and melting experiments constrain the fate of subducted sediments. Geochemistry, Geophysics, Geosystems 1.

Karato, S.-i., 2010. Rheology of the deep upper mantle and its implications for the preservation of the continental roots: A review. Tectonophysics 481, 82-98.

Karato, S.-i., 2012. On the origin of the asthenosphere. Earth and Planetary Science Letters 321, 95-103.

Karato, S.-I., Jung, H., 2003. Effects of pressure on high-temperature dislocation creep in olivine. Philosophical Magazine 83, 401-414.

Karato, S.-i., Wu, P., 1993. Rheology of the upper mantle: A synthesis. Science 260, 771-778.

Kay, R., 1978. Aleutian magnesian andesites: melts from subducted Pacific Ocean crust. Journal of Volcanology and Geothermal Research 4, 117-132.

Kay, R., Mahlburg-Kay, S., 1991. Creation and destruction of lower continental crust. Geologische Rundschau 80, 259-278.

Kelemen, P.B., Behn, M.D., 2016. Formation of lower continental crust by relamination of buoyant arc lavas and plutons. Nature Geoscience.

Kerr, A.C., Tarney, J., Marriner, G.F., Nivia, A., Saunders, A.D., 1997. The Caribbean-Colombian Cretaceous igneous province: The internal anatomy of an oceanic plateau. Geophysical monograph - American Geophysical Union 100, 123-144.

Kessel, R., Schmidt, M.W., Ulmer, P., Pettke, T., 2005. Trace element signature of subduction-zone fluids, melts and supercritical liquids at 120-180 km depth. Nature 437, 724.

Kirby, S., Kronenberg, A., 1987. Rheology of the lithosphere: Selected topics. Reviews of Geophysics 25, 1219-1244.

Kirby, S.H., Stein, S., Okal, E.A., Rubie, D.C., 1996. Metastable mantle phase transformations and deep earthquakes in subducting oceanic lithosphere. Reviews of Geophysics 34, 261-306.

Kohlstedt, D., Evans, B., Mackwell, S., 1995. Strength of the lithosphere: Constraints imposed by laboratory experiments. Journal of Geophysical Research: Solid Earth 100, 17587-17602.

Korenaga, J., 2006. Archean geodynamics and the thermal evolution of Earth. Archean Geodynamics and Environments, 7-32.

Lallemand, S., Heuret, A., Faccenna, C., Funiciello, F., 2008. Subduction dynamics as revealed by trench migration. Tectonics 27.

Laske, G., Masters, G., Ma, Z., Pasyanos, M., 2013. Update on CRUST1. 0—A 1-degree global model of Earth's crust, Geophys. Res. Abstracts, p. 20132658abstrEGU.

Lourenço, D.L., Rozel, A., Tackley, P.J., 2016. Melting-induced crustal production helps plate tectonics on Earth-like planets. Earth and Planetary Science Letters 439, 18-28.

Mackwell, S., Zimmerman, M., Kohlstedt, D., 1998. High-temperature deformation of dry diabase with application to tectonics on Venus. Journal of Geophysical Research: Solid Earth (1978–2012) 103, 975-984.

Macpherson, C.G., Dreher, S.T., Thirlwall, M.F., 2006. Adakites without slab melting: high pressure differentiation of island arc magma, Mindanao, the Philippines. Earth and Planetary Science Letters 243, 581-593.

Magni, V., Bouilhol, P., van Hunen, J., 2014. Deep water recycling through time. Geochemistry, Geophysics, Geosystems 15, 4203-4216.

Magni, V., Faccenna, C., Hunen, J., Funiciello, F., 2013. Delamination vs. break-off: the fate of continental collision. Geophysical Research Letters 40, 285-289.

Makkonen, L., 2006. Plotting positions in extreme value analysis. Journal of Applied Meteorology and Climatology 45, 334-340.

Mantle, G., Collins, W., 2008. Quantifying crustal thickness variations in evolving orogens: Correlation between arc basalt composition and Moho depth. Geology 36, 87-90.

Marschall, H.R., 2005. Lithium, beryllium and boron in high-pressure metamorphic rocks from Syros (Greece).

Marschall, H.R., Schumacher, J.C., 2012. Arc magmas sourced from mélange diapirs in subduction zones. Nature Geoscience 5, 862-867.

Martin, H., 1999. Adakitic magmas: modern analogues of Archaean granitoids. Lithos 46, 411-429.

Martin, H., Moyen, J., 2003. Secular changes in TTG composition: comparison with modern adakites, EGS-AGU-EUG Joint Assembly, p. 2673.

Maunder, B., van Hunen, J., Magni, V., Bouilhol, P., 2016. Relamination of mafic subducting crust throughout Earth's history. Earth and Planetary Science Letters 449, 206-216.

McDonough, W., 1991. Partial melting of subducted oceanic crust and isolation of its residual eclogitic lithology. Philosophical Transactions of the Royal Society of London A: Mathematical, Physical and Engineering Sciences 335, 407-418.

McKenzie, D., Bickle, M., 1988. The volume and composition of melt generated by extension of the lithosphere. Journal of petrology 29, 625-679.

McKenzie, D.P., 1966. The viscosity of the lower mantle. Journal of Geophysical Research 71, 3995-4010.

McKenzie, D.P., 1969. Speculations on the consequences and causes of plate motions. Geophysical Journal International 18, 1-32.

McKenzie, D.P., Parker, R.L., 1967. The North Pacific: an example of tectonics on a sphere. Nature 216, 1276-1280.

Mei, S., Kohlstedt, D., 2000. Influence of water on plastic deformation of olivine aggregates: 1. Diffusion creep regime. Journal of Geophysical Research: Solid Earth 105, 21457-21469.

Mitrovica, J., Forte, A., 2004. A new inference of mantle viscosity based upon joint inversion of convection and glacial isostatic adjustment data. Earth and Planetary Science Letters 225, 177-189.

Molnar, P., England, P., 1995. Temperatures in zones of steady-state underthrusting of young oceanic lithosphere. Earth and Planetary Science Letters 131, 57-70.

Molnar, P., Tapponnier, P., 1975. Cenozoic tectonics of Asia: effects of a continental collision. Science 189, 419-426.

Moore, W.B., Webb, A.A.G., 2013. Heat-pipe earth. Nature 501, 501-505.

Moresi, L., Gurnis, M., 1996. Constraints on the lateral strength of slabs from three-dimensional dynamic flow models. Earth and Planetary Science Letters 138, 15-28.

Moresi, L.N., Solomatov, V., 1995. Numerical investigation of 2D convection with extremely large viscosity variations. Physics of Fluids 7, 2154-2162.

Moyen, J.-F., 2009. High Sr/Y and La/Yb ratios: the meaning of the "adakitic signature". Lithos 112, 556-574.

Moyen, J.-F., 2011. The composite Archaean grey gneisses: petrological significance, and evidence for a non-unique tectonic setting for Archaean crustal growth. Lithos 123, 21-36.

Moyen, J.-F., Van Hunen, J., 2012. Short-term episodicity of Archaean plate tectonics. Geology 40, 451-454.

Nichols, G.T., Wyllle, P.J., 1994. Subduction zone melting of pelagic sediments constrained. Nature 371, 27.

O'Neill, C., Debaille, V., Griffin, W., 2013. Deep earth recycling in the Hadean and constraints on surface tectonics. American Journal of Science 313, 912-932.

O'Neill, C., Lenardic, A., Moresi, L., Torsvik, T., Lee, C.-T., 2007. Episodic precambrian subduction. Earth and Planetary Science Letters 262, 552-562.

Peacock, S.M., 1990. Numerical simulation of metamorphic pressure-temperature-time paths and fluid production in subducting slabs. Tectonics 9, 1197-1211.

Peacock, S.M., 1996. Thermal and petrologic structure of subduction zones. Subduction top to bottom, 119-133.

Peacock, S.M., 2003. Thermal structure and metamorphic evolution of subducting slabs. Inside the subduction factory, 7-22.

Pearce, J.A., 1982. Trace element characteristics of lavas from destructive plate boundaries. Andesites 8, 525-548.

Pearce, J.A., Peate, D.W., 1995. Tectonic implications of the composition of volcanic arc magmas. Annual Review of Earth and Planetary Sciences 23, 251-285.

Penniston-Dorland, S.C., Kohn, M.J., Manning, C.E., 2015. The global range of subduction zone thermal structures from exhumed blueschists and eclogites: rocks are hotter than models. Earth and Planetary Science Letters 428, 243-254.

Peterson, E.T., Seno, T., 1984. Factors affecting seismic moment release rates in subduction zones. Journal of Geophysical Research: Solid Earth 89, 10233-10248.

Plank, T., Cooper, L.B., Manning, C.E., 2009. Emerging geothermometers for estimating slab surface temperatures. Nature Geoscience 2, 611-615.

Plank, T., Langmuir, C.H., 1988. An evaluation of the global variations in the major element chemistry of arc basalts. Earth and Planetary Science Letters 90, 349-370.

Plank, T., Langmuir, C.H., 1993. Tracing trace elements from sediment input to volcanic output at subduction zones. Nature 362, 739-743.

Polat, A., 2012. Growth of Archean continental crust in oceanic island arcs. Geology 40, 383-384.

Poli, S., Schmidt, M.W., 1995. H2O transport and release in subduction zones: experimental constraints on basaltic and andesitic systems. Journal of Geophysical Research: Solid Earth (1978–2012) 100, 22299-22314.

Poli, S., Schmidt, M.W., 2002. Petrology of subducted slabs. Annual Review of Earth and Planetary Sciences 30, 207-235.

Profeta, L., Ducea, M.N., Chapman, J.B., Paterson, S.R., Gonzales, S.M.H., Kirsch, M., Petrescu, L., DeCelles, P.G., 2015. Quantifying crustal thickness over time in magmatic arcs. Scientific Reports 5.

Ranalli, G., 1995. Rheology of the Earth. Springer.

Ranero, C., Sallares, V., 2004. Geophysical evidence for hydration of the crust and mantle of the Nazca plate during bending at the north Chile trench. Geology 32, 549-552.

Rey, P.F., Coltice, N., Flament, N., 2014. Spreading continents kick-started plate tectonics. Nature 513, 405-408.

Reymer, A., Schubert, G., 1984. Phanerozoic addition rates to the continental crust and crustal growth. Tectonics 3, 63-77.

Ricard, Y., Wuming, B., 1991. Inferring the viscosity and the 3-D density structure of the mantle from geoid, topography and plate velocities. Geophysical Journal International 105, 561-571.

Rozel, A., Golabek, G., Jain, C., Tackley, P., Gerya, T., 2017. Continental crust formation on early Earth controlled by intrusive magmatism. Nature 545, 332-335.

Rudnick, R., Gao, S., 2003. Composition of the continental crust. Treatise on geochemistry 3, 659.

Rudnick, R.L., 1995. Making continental crust. Nature 378, 571-577.

Ruff, L., Kanamori, H., 1980. Seismicity and the subduction process. Physics of the Earth and Planetary interiors 23, 240-252.

Rüpke, L.H., Morgan, J.P., Hort, M., Connolly, J.A., 2004. Serpentine and the subduction zone water cycle. Earth and Planetary Science Letters 223, 17-34.

Ruscitto, D.M., Wallace, P.J., Cooper, L.B., Plank, T., 2012. Global variations in H2O/Ce: 2. Relationships to arc magma geochemistry and volatile fluxes. Geochemistry, Geophysics, Geosystems 13.

Sajona, F.G., Maury, R.C., Bellon, H., Cotten, J., Defant, M.J., Pubellier, M., 1993. Initiation of subduction and the generation of slab melts in western and eastern Mindanao, Philippines. Geology 21, 1007-1010.

Savov, I.P., Ryan, J.G., D'Antonio, M., Fryer, P., 2007. Shallow slab fluid release across and along the Mariana arc-basin system: Insights from geochemistry of serpentinized peridotites from the Mariana fore arc. Journal of Geophysical Research: Solid Earth 112.

Schmidt, M., Jagoutz, O., 2017. The global systematics of primitive arc melts. Geochemistry, Geophysics, Geosystems.

Schmidt, M., Poli, S., 2014. 4.19. Devolatilization during subduction. The Crust, Treatise on Geochemistry (eds. HD Holland and KK Turekian, Second Edition), Elsevier-Pergamon, Oxford, 669-701.

Shelton, G., Tullis, J., 1981. Experimental flow laws for crustal rocks. Eos Trans. AGU 62, 396.

Shirey, S.B., Richardson, S.H., 2011. Start of the Wilson cycle at 3 Ga shown by diamonds from subcontinental mantle. Science 333, 434-436.

Shreve, R.L., Cloos, M., 1986. Dynamics of sediment subduction, melange formation, and prism accretion. Journal of Geophysical Research: Solid Earth 91, 10229-10245.

Silver, P.G., Behn, M.D., 2008. Intermittent plate tectonics? science 319, 85-88.

Sizova, E., Gerya, T., Brown, M., 2014. Contrasting styles of Phanerozoic and Precambrian continental collision. Gondwana Research 25, 522-545.

Sizova, E., Gerya, T., Brown, M., Perchuk, L., 2010. Subduction styles in the Precambrian: insight from numerical experiments. Lithos 116, 209-229.

Sizova, E., Gerya, T., Stüwe, K., Brown, M., 2015. Generation of felsic crust in the Archean: A geodynamic modeling perspective. Precambrian Research 271, 198-224.

Skjerlie, K.P., Douce, A.E.P., 2002. The fluid-absent partial melting of a zoisite-bearing quartz eclogite from 1· 0 to 3· 2 GPa; Implications for melting in thickened continental crust and for subduction-zone processes. Journal of Petrology 43, 291-314.

Sleep, N.H., 1992. Archean plate tectonics: what can be learned from continental geology? Canadian Journal of Earth Sciences 29, 2066-2071.

Smithies, R., 2000. The Archaean tonalite–trondhjemite–granodiorite (TTG) series is not an analogue of Cenozoic adakite. Earth and Planetary Science Letters 182, 115-125.

Stern, R.A., Bleeker, W., 1998. Age of the world's oldest rocks refined using Canada's SHRIMP: The Acasta Gneiss Complex, Northwest Territories, Canada. Geoscience Canada 25.

Stern, R.J., Gerya, T., Tackley, P.J., 2017. Stagnant lid tectonics: Perspectives from silicate planets, dwarf planets, large moons, and large asteroids. Geoscience Frontiers.

Stevens, G., Moyen, J.-F., 2007. Metamorphism in the Barberton Granite Greenstone Terrain: a record of Paleoarchean accretion. Earth's Oldest Rocks. Developments in Precambrian Geology 15, 669-698.

Syracuse, E.M., van Keken, P.E., Abers, G.A., 2010. The global range of subduction zone thermal models. Physics of the Earth and Planetary Interiors 183, 73-90.

Tatsumi, Y., 2005. The subduction factory: how it operates in the evolving Earth. GSA today 15, 4.

Taylor, S.R., McLennan, S.M., 1985. The continental crust: its composition and evolution.

Taylor, S.R., McLennan, S.M., 1995. The geochemical evolution of the continental crust. Reviews of Geophysics 33, 241-265.

Thorkelson, D.J., Breitsprecher, K., 2005. Partial melting of slab window margins: genesis of adakitic and non-adakitic magmas. Lithos 79, 25-41.

Turcotte, D.L., Schubert, G., 2014. Geodynamics. Cambridge University Press.

Turner, S.J., Langmuir, C.H., 2015a. The global chemical systematics of arc front stratovolcanoes: Evaluating the role of crustal processes. Earth and Planetary Science Letters 422, 182-193.

Turner, S.J., Langmuir, C.H., 2015b. What processes control the chemical compositions of arc front stratovolcanoes? Geochemistry, Geophysics, Geosystems 16, 1865-1893.

Turner, S.J., Langmuir, C.H., Katz, R.F., Dungan, M.A., Escrig, S., 2016. Parental arc magma compositions dominantly controlled by mantle-wedge thermal structure. Nature Geoscience 9, 772-776.

Ulmer, P., Trommsdorff, V., 1995. Serpentine stability to mantle depths and subduction-related magmatism. Science 268, 858.

van Hunen, J., Moyen, J.-F., 2012. Archean subduction: fact or fiction? Annual Review of Earth and Planetary Sciences 40, 195-219.

van Hunen, J., van den Berg, A.P., 2008. Plate tectonics on the early Earth: limitations imposed by strength and buoyancy of subducted lithosphere. Lithos 103, 217-235.

van Hunen, J., van Den Berg, A.P., Vlaar, N.J., 2002. On the role of subducting oceanic plateaus in the development of shallow flat subduction. Tectonophysics 352, 317-333.

van Hunen, J., van den Berg, A.P., Vlaar, N.J., 2004. Various mechanisms to induce present-day shallow flat subduction and implications for the younger Earth: a numerical parameter study. Physics of the Earth and Planetary Interiors 146, 179-194.

van Keken, P.E., Currie, C., King, S.D., Behn, M.D., Cagnioncle, A., He, J., Katz, R.F., Lin, S.-C., Parmentier, E.M., Spiegelman, M., 2008. A community benchmark for subduction zone modeling. Physics of the Earth and Planetary Interiors 171, 187-197.

van Keken, P.E., Hacker, B.R., Syracuse, E.M., Abers, G.A., 2011. Subduction factory: 4. Depth-dependent flux of H2O from subducting slabs worldwide. Journal of Geophysical Research: Solid Earth 116.

van Keken, P.E., Kiefer, B., Peacock, S.M., 2002. High-resolution models of subduction zones: Implications for mineral dehydration reactions and the transport of water into the deep mantle. Geochemistry, Geophysics, Geosystems 3.

van Thienen, P., van den Berg, A., Vlaar, N., 2004a. Production and recycling of oceanic crust in the early Earth. Tectonophysics 386, 41-65.

van Thienen, P., Vlaar, N., Van den Berg, A., 2004b. Plate tectonics on the terrestrial planets. Physics of the Earth and Planetary Interiors 142, 61-74.

Verhoogen, J., 1962. Distribution of titanium between silicates and oxides in igneous rocks. American Journal of Science 260, 211-220.

Villiger, S., Ulmer, P., Müntener, O., 2006. Equilibrium and fractional crystallization experiments at 0· 7 GPa; the effect of pressure on phase relations and liquid compositions of tholeiitic magmas. Journal of Petrology 48, 159-184.

Vogt, K., Castro, A., Gerya, T., 2013. Numerical modeling of geochemical variations caused by crustal relamination. Geochemistry, Geophysics, Geosystems 14, 470-487.

Vogt, K., Gerya, T., 2014. Deep plate serpentinization triggers skinning of subducting slabs. Geology 42, 723-726.

Wada, I., Wang, K., 2009. Common depth of slab-mantle decoupling: Reconciling diversity and uniformity of subduction zones. Geochemistry, Geophysics, Geosystems 10.

Walcott, R.I., 1973. Structure of the earth from glacio-isostatic rebound. Annual Review of Earth and Planetary Sciences 1, 15.

Wang, H., Agrusta, R., van Hunen, J., 2015. Advantages of a conservative velocity interpolation (CVI) scheme for particle-in-cell methods with application in geodynamic modelling. Geochemistry, Geophysics, Geosystems.

Wegener, A., 1912. Die entstehung der kontinente. Geologische Rundschau 3, 276-292.

Wiens, D.A., Gilbert, H.J., 1996. Effect of slab temperature on deep-earthquake aftershock productivity and magnitude-frequency relations. Nature 384, 153.

Wilde, S.A., Valley, J.W., Peck, W.H., Graham, C.M., 2001. Evidence from detrital zircons for the existence of continental crust and oceans on the Earth 4.4 Gyr ago. Nature 409, 175-178.

Wilks, K.R., Carter, N.L., 1990. Rheology of some continental lower crustal rocks. Tectonophysics 182, 57-77.

Wilson, J.T., 1966. Did the Atlantic close and then re-open? Nature.

Wolery, T.J., Sleep, N.H., 1976. Hydrothermal circulation and geochemical flux at mid-ocean ridges. The Journal of Geology 84, 249-275.

Yogodzinski, G., Kay, R., Volynets, O., Koloskov, A., Kay, S., 1995. Magnesian andesite in the western Aleutian Komandorsky region: implications for slab melting and processes in the mantle wedge. Geological Society of America Bulletin 107, 505-519.

Zegers, T.E., van Keken, P.E., 2001. Middle Archean continent formation by crustal delamination. Geology 29, 1083-1086.

Zhang, R., Liou, J., 1997. Partial transformation of gabbro to coesite-bearing eclogite from Yangkou, the Sulu terrane, eastern China. Journal of Metamorphic Geology 15, 183-202.

Zhong, S., Yuen, D.A., Moresi, L.N., 2007. Numerical methods for mantle convection. Treatise on Geophysics 7, 227-252.

Zhong, S., Zuber, M.T., Moresi, L., Gurnis, M., 2000. Role of temperature-dependent viscosity and surface plates in spherical shell models of mantle convection. Journal of Geophysical Research: Solid Earth (1978–2012) 105, 11063-11082.

Appendix (Data Table for Chapter 4)

		Adjusted Thermal Parameter Analysis						Crustal Thickness				Original Correlations				
		a	b	c	p	max r^2	+/-	vs ER	+/-	vs ACP	ACP-CT	age	spd	ang	TP	segs
B	Hf	1.0	0.8	-0.2	0.04	0.33	-	0.07	+	0.03	0.66	0.07	0.23	0.02	0.26	54
Ba	Hf	1.0	-0.3	0.1	0.04	0.08	-	0.08	-	0.19	0.01	0.08	0.01	0.02	0.02	98
Be	Hf	1.0	0.0	-0.6	0.36	0.12	+	0.00	+	0.01	0.95	0.08	0.00	0.00	0.02	54
Cs	Hf	1.0	-0.3	-1.0	0.04	0.10	+	0.05	+	0.02	0.37	0.04	0.01	0.02	0.00	91
La	Hf	1.0	0.5	0.4	0.04	0.16	-	0.18	+	0.24	-0.07	0.12	0.02	0.06	0.15	98
Pb	Hf	1.0	0.6	-0.6	0.55	0.03	+	0.02	+	0.00	0.32	0.01	0.01	0.00	0.02	89
Rb	Hf	-0.4	0.8	1.0	0.27	0.06	-	0.11	-	0.11	-0.27	0.00	0.04	0.02	0.02	98
Sr	Hf	1.0	-0.4	-0.9	0.13	0.16	-	0.05	+	0.01	0.53	0.06	0.04	0.02	0.00	94
Th	Hf	0.3	0.9	1.0	0.04	0.13	-	0.24	+	0.22	-0.29	0.02	0.06	0.06	0.11	97
U	Hf	0.5	0.9	1.0	0.18	0.10	-	0.20	-	0.22	-0.35	0.03	0.04	0.04	0.09	95
B	Nb	1.0	0.2	1.0	0.10	0.17	+	0.07	-	0.44	0.43	0.12	0.00	0.13	0.12	55
Ba	Nb	0.3	0.9	1.0	0.04	0.12	+	0.06	-	0.22	0.34	0.02	0.06	0.05	0.09	101
Be	Nb	1.0	-0.1	-0.2	0.27	0.09	+	0.04	-	0.06	0.41	0.09	0.00	0.01	0.03	59
Cs	Nb	1.0	0.2	0.1	0.04	0.18	+	0.03	-	0.22	0.68	0.16	0.01	0.04	0.14	89
La	Nb	0.5	0.4	1.0	0.18	0.09	+	0.08	-	0.38	0.05	0.04	0.01	0.07	0.07	97
Pb	Nb	1.0	0.6	0.6	0.04	0.27	+	0.15	-	0.27	0.29	0.16	0.06	0.13	0.27	93
Rb	Nb	1.0	0.2	0.5	0.11	0.13	+	0.02	-	0.33	0.70	0.11	0.00	0.07	0.10	99
Sr	Nb	-0.2	0.5	1.0	0.04	0.18	+	0.21	-	0.22	-0.09	0.01	0.05	0.12	0.08	95
Th	Nb	1.0	-0.4	0.2	0.09	0.08	+	0.00	-	0.20	0.99	0.07	0.02	0.03	0.02	98
U	Nb	1.0	0.2	0.8	0.18	0.10	+	0.03	+	0.35	0.59	0.07	0.00	0.06	0.07	92
B	Ta	0.4	0.1	1.0	0.18	0.18	+	0.09	-	0.53	0.34	0.09	0.00	0.17	0.11	53
Ba	Ta	-0.1	0.6	1.0	0.04	0.14	+	0.10	-	0.23	0.16	0.01	0.06	0.08	0.08	94
Be	Ta	1.0	-0.2	0.4	0.64	0.05	+	0.04	-	0.23	0.14	0.04	0.01	0.02	0.02	53
Cs	Ta	1.0	0.2	0.1	0.04	0.17	+	0.04	-	0.22	0.62	0.16	0.01	0.04	0.14	88
La	Ta	-0.1	0.3	1.0	0.04	0.10	+	0.10	-	0.31	0.01	0.01	0.02	0.08	0.05	94
Pb	Ta	0.6	0.7	1.0	0.04	0.26	+	0.19	-	0.30	0.17	0.10	0.08	0.16	0.24	87
Rb	Ta	1.0	0.1	0.9	0.27	0.08	+	0.04	-	0.37	0.33	0.06	0.00	0.06	0.05	93
Sr	Ta	-0.3	0.4	1.0	0.04	0.17	+	0.20	-	0.23	-0.06	0.00	0.05	0.11	0.06	89
Th	Ta	0.4	-0.6	1.0	0.82	0.03	+	0.00	-	0.29	1.00	0.01	0.01	0.02	0.00	94
U	Ta	0.2	0.2	1.0	0.18	0.10	+	0.05	+	0.39	0.34	0.03	0.01	0.09	0.06	92
B	Ti	1.0	0.6	0.3	0.04	0.29	-	0.28	+	0.18	0.02	0.09	0.12	0.09	0.28	47
Ba	Ti	0.4	0.0	1.0	0.04	0.22	-	0.44	+	0.43	-0.33	0.11	0.00	0.20	0.10	83
Be	Ti	-0.8	0.0	1.0	0.04	0.27	-	0.23	+	0.18	0.09	0.03	0.00	0.13	0.00	54
Cs	Ti	-0.4	0.1	1.0	0.04	0.16	-	0.25	+	0.25	-0.24	0.00	0.00	0.12	0.02	79
La	Ti	0.4	0.2	1.0	0.04	0.31	-	0.40	+	0.38	-0.13	0.13	0.01	0.26	0.22	82
Pb	Ti	-0.3	0.0	1.0	0.04	0.16	-	0.38	+	0.36	-0.41	0.01	0.00	0.15	0.03	78
Rb	Ti	0.0	0.2	1.0	0.04	0.18	-	0.37	+	0.34	-0.36	0.03	0.01	0.15	0.09	83
Sr	Ti	1.0	0.1	0.9	0.04	0.34	-	0.37	+	0.38	-0.05	0.25	0.00	0.24	0.23	83
Th	Ti	0.1	0.3	1.0	0.04	0.24	-	0.40	+	0.31	-0.24	0.05	0.02	0.20	0.15	82
U	Ti	0.2	0.2	1.0	0.04	0.22	-	0.40	-	0.39	-0.30	0.06	0.01	0.18	0.14	81

B	Y	1.0	0.5	0.3	0.04	0.20	-	0.16	+	0.23	0.12	0.12	0.07	0.06	0.20	56
Ba	Y	1.0	0.0	0.5	0.04	0.28	-	0.40	+	0.33	-0.17	0.25	0.00	0.15	0.18	98
Be	Y	-0.4	0.1	1.0	0.12	0.14	-	0.25	+	0.23	-0.28	0.00	0.00	0.12	0.01	56
Cs	Y	-0.1	0.4	1.0	0.18	0.11	-	0.25	+	0.31	-0.37	0.01	0.03	0.08	0.06	87
La	Y	1.0	0.4	0.7	0.04	0.32	-	0.38	+	0.33	-0.09	0.23	0.03	0.18	0.28	95
Pb	Y	0.5	0.2	1.0	0.07	0.11	-	0.30	+	0.42	-0.48	0.06	0.00	0.09	0.08	90
Rb	Y	0.6	0.5	1.0	0.04	0.18	-	0.44	+	0.34	-0.41	0.09	0.03	0.13	0.16	97
Sr	Y	1.0	0.0	-0.1	0.04	0.33	-	0.10	+	0.16	0.53	0.33	0.00	0.06	0.16	93
Th	Y	0.5	0.6	1.0	0.04	0.23	-	0.38	+	0.34	-0.24	0.09	0.06	0.16	0.20	95
U	Y	0.4	0.5	1.0	0.04	0.21	-	0.33	-	0.33	-0.22	0.08	0.05	0.15	0.18	91
B	Yb	1.0	0.5	0.3	0.17	0.17	-	0.14	+	0.24	0.11	0.11	0.05	0.05	0.17	56
Ba	Yb	1.0	0.1	0.8	0.04	0.33	-	0.39	+	0.38	-0.09	0.26	0.00	0.21	0.21	101
Be	Yb	-0.2	-0.1	1.0	0.17	0.13	-	0.24	+	0.36	-0.31	0.01	0.01	0.12	0.01	56
Cs	Yb	0.0	0.4	1.0	0.04	0.14	-	0.29	+	0.32	-0.35	0.02	0.03	0.10	0.08	91
La	Yb	1.0	0.5	1.0	0.04	0.34	-	0.41	+	0.36	-0.09	0.23	0.03	0.22	0.29	101
Pb	Yb	0.6	0.2	1.0	0.04	0.14	-	0.33	+	0.41	-0.39	0.08	0.00	0.12	0.09	91
Rb	Yb	0.5	0.5	1.0	0.04	0.24	-	0.42	+	0.36	-0.28	0.10	0.04	0.17	0.19	101
Sr	Yb	1.0	0.0	0.1	0.04	0.36	-	0.14	+	0.23	0.45	0.36	0.00	0.10	0.19	99
Th	Yb	0.6	0.6	1.0	0.04	0.24	-	0.39	+	0.33	-0.24	0.10	0.05	0.15	0.21	100
U	Yb	0.8	0.6	1.0	0.04	0.25	-	0.40	-	0.31	-0.22	0.13	0.04	0.15	0.23	96
B	Zr	0.0	1.0	-0.8	0.45	0.10	-	0.00	+	0.10	0.93	0.01	0.08	0.02	0.01	55
Ba	Zr	1.0	-0.5	-0.2	0.27	0.05	-	0.03	-	0.07	0.21	0.04	0.02	0.00	0.00	106
Be	Zr	1.0	0.0	-0.7	0.18	0.16	+	0.00	+	0.02	0.99	0.10	0.00	0.01	0.04	55
Cs	Zr	1.0	-0.2	-0.6	0.04	0.10	+	0.02	+	0.01	0.65	0.07	0.01	0.00	0.01	89
La	Zr	1.0	0.7	0.5	0.13	0.08	-	0.09	-	0.24	-0.05	0.05	0.02	0.03	0.08	102
Pb	Zr	1.0	0.4	0.1	0.27	0.07	+	0.00	+	0.18	0.99	0.05	0.01	0.02	0.06	93
Rb	Zr	-0.7	0.9	1.0	0.36	0.04	-	0.12	-	0.04	-0.52	0.00	0.02	0.01	0.01	104
Sr	Zr	-0.9	0.4	1.0	0.04	0.16	+	0.09	+	0.04	0.29	0.03	0.04	0.04	0.00	100
Th	Zr	0.1	1.0	0.9	0.04	0.10	-	0.18	+	0.16	-0.27	0.01	0.07	0.04	0.07	102
U	Zr	-0.1	0.9	1.0	0.45	0.05	-	0.10	-	0.13	-0.33	0.00	0.03	0.02	0.03	96

Supplementary Table Combined analysis results extracted from the unfiltered dataset. The section headed "Adjusted Chemical Parameter Analysis" contains results relevant to the ACP study (see Section 4.3.4). "a", "b" and "c" contain the optimal values of a (the age exponent), b (the speed exponent) and c (the angle exponent), in the definition of the ACP (see Equation 4.2) for each element ratio (ER) (element in first column over element in second column). The column labelled "max r^2" is the r^2 of a log-log plot of the ER and the optimal ACP. The sense of correlation of this plot is given in the next column, headed "+/-". The column "p" contains the p-value; effectively the probability that we are able to achieve as high a maximum r^2 value if the data were random. This is calculated by monte-carlo permutation test (see Section 4.2.3).The section headed "Crustal Thickness" contains results relating to the overriding crustal thickness (CT). The r^2 values of plots of log(ER) vs CT and log(ACP) vs CT are given in the columns "vs ER" (with the sense of correlation next to it) and "vs ACP". The column headed "ACP-CT" contains the difference between the r^2 of ER vs ACP and the r^2 of ER vs CT, divided by their sum. This is used as an indicator of which type of process is driving the observed correlation: whether it is CT and the state of the overriding plate that seems to drive it, or the ACP and the state of the slab. The section headed "Original Correlations" gives the r^2 values of log log plots of ER and age, speed, angle and the original definition of the thermal parameter in the columns "age", "spd", "ang" and "TP" respectively. The final column "segs" is the number of segments used in the analysis of each particular ER.